SANDIA REPORT

SAND99–8225
Unlimited Release
Printed February 1999

A Fully Coupled Computational Model of the Silylation Process

W. S. Winters, G. H. Evans, R. S. Larson, V. C. Prantil

Prepared by
Sandia National Laboratories
Albuquerque, New Mexico 87185 and Livermore, California 94550

Sandia is a multiprogram laboratory operated by Sandia Corporation,
a Lockheed Martin Company, for the United States Department of
Energy under Contract DE-AC04-94AL85000.

Sandia National Laboratories

Issued by Sandia National Laboratories, operated for the United States Department of Energy by Sandia Corporation.

Available to DOE and DOE contractors from
Office of Scientific and Technical Information
P.O. Box 62
Oak Ridge, TN 37831

Prices available from (615) 576-8401, FTS 626-8401

Available to the public from
National Technical Information Service
U.S. Department of Commerce
5285 Port Royal Rd
Springfield, VA 22161

NTIS price codes
Printed copy: A06
Microfiche copy: A01

SAND99-8225
Unlimited Release
Printed February 1999

A Fully Coupled Computational Model of the Silylation Process

W. S. Winters, G. H. Evans and R. S. Larson
Computational Reactive Processes Department
Sandia National Laboratories / California

V. C. Prantil
Solid and Material Mechanics Department
Sandia National Laboratories / California

This report documents the development of a new finite element model of the positive tone silylation process. Model development makes use of pre-existing Sandia technology used to describe coupled thermal-mechanical behavior in deforming metals. Material properties and constitutive models were obtained from the literature. The model is two-dimensional and transient and focuses on the part of the lithography process in which crosslinked and uncrosslinked resist is exposed to a gaseous silylation agent. The model accounts for the combined effects of mass transport (diffusion of silylation agent and reaction product), chemical reaction resulting in the uptake of silicon and material swelling, the generation of stresses, and the resulting material motion. The influence of stress on diffusion and reaction rates is also included. Both Fickian and case II diffusion models have been incorporated. The model provides for the appropriate mass transport and momentum boundary conditions and couples the behavior (stress/strain) of uncrosslinked and crosslinked materials as well including the underlying device topology. Finite element mesh generation, problem setup, and post processing of computed results is sufficiently mature to permit investigation of a broad parameter space which includes material properties and geometry issues (*e.g.*, alternate crosslinking distributions, resist thickness, etc.). The 2D transient model has been validated for simple geometries using independent material point simulations and one-dimensional transient simulations. A complete 2D transient simulation of the silylation process is presented and discussed. Recommendations for future work are presented.

Contents

List of Figures

1 Nomenclature

a	mean molecular radius
A	area,proportionality constant
A	silylating reagent
$A_a(t)$	surface area of arbitrary control volume (function of time)
B	element geometry parameter defined by Equation (115);
B	amine product of silylating reaction given by Equation (1)
C	unexposed, unsilylated polymer resist material
C_r	rubbery modulus
$\mathcal{C}$	elastic modulus tensor
c_i	molar concentration of species i (moles i / volume)
D	unexpanded, silylated resist material
$\mathbf{D}$	deformation rate tensor
$\mathcal{D}$	diffusion coefficient (*cf. Equations (21) and (22)*)
$\mathcal{D}_o$	constant part of diffusion coefficient (*cf. Equations (21) and (22)*)
E	expanded, silylated resist material
$\mathbf{F}$	body force vector, deformation gradient tensor
$F_{i,j}$	nodal body force components where $i = x, y$ and $j = 1, 2, 3, 4$
$\{F\}$	column vector of body force components defined by Equation (86)
f	density scaling factor
h	hardening modulus
H	Henry's constant
$\lvert J \rvert$	element Jacobian defined by Equation (77)
j_i	mass diffusion flux of species i
K_g	mass transfer coefficient
k	Boltman's constant
k_e	rate constant for polymer relaxation reaction (Equation (2))
k_s	silylation rate constant for silylation reaction (Equation (1))
$[M]$	mass matrix
M_i	molecular weight of species i
m	mass
m_{i_p}	mass of species i in control volume centered about point p
$\mathbf{n}$	unit normal vector
$\mathbf{N}$	stress direction
N_I	element bilinear shape function defined by Equation (57) where I=1,2,3,4
p	scalar material constitutive parameter
$\mathbf{Q}$	rotation tensor
q	scalar material constitutive parameter
R	yield limit
RHS	right hand side
$\mathbf{R}$	rotation tensor
s	flow resistance
S	path along a surface
t	time
Δt	time step
$\mathbf{U}$	right stretch tensor
u_I	x component of displacement at node $I, I = 1, 2, 3, 4$
$\dot{u}_I$	x component of velocity at node $I, I = 1, 2, 3, 4$
$\ddot{u}_I$	x component of acceleration at node $I, I = 1, 2, 3, 4$
v_I	y component of displacement at node I, I=1,2,3,4
$\mathbf{v}_i$	velocity of species i
$\mathbf{V}$	left stretch tensor
$\mathbf{V}_i$	diffusion velocity of species i
$\dot{v}_I$	y component of velocity at node $I, I = 1, 2, 3, 4$

$\ddot{v}_I$	y component of acceleration at node $I, I = 1, 2, 3, 4$
$\mathbf{v}$	velocity vector (mass average)
$\dot{\mathbf{v}}$	acceleration vector
$\{\ddot{v}\}$	column vector of acceleration components defined by Equation (85)
V	volume
$V_a(t)$	volume of arbitrary control volume (function of time)
$V_p(t)$	volume of control volume centered about point P (function of time)
$\mathbf{W}$	spin tensor
W	finite element weighting function
$\mathbf{w}_{\mathrm{arb}}$	arbitrary velocity of control volume
w	coefficient in exponential diffusion expressions (*cf. Equations (21) and (22)*)
x	cartesian coordinate x
$\mathbf{x}$	position vector
x_I	x coordinate of node $I, I = 1, 2, 3, 4$
y	cartesian coordinate y
Y_i	mass fraction of species i
y_I	y coordinate of node $I, I = 1, 2, 3, 4$
$\mathcal{Y}$	yield function

1.1 Greek symbols

α	coefficient of thermal expansion
ϵ_i	volume fraction of species i
$[\Lambda]$	coefficient matrix defined by Equation (88)
Φ	nodal dependent variable defined by Equation (54), silylation swelling
ρ	density
$\tilde{\rho}_i$	intrinsic density of species i (mass i / volume i),
σ	stress tensor
$\{\sigma\}$	column vector of stress components defined by Equation (87)
σ_{xx}	x component of the traction vector on a plane whose normal points in the x direction
σ_{yy}	y component of the traction vector on a plane whose normal points in the y direction
σ_{zz}	z component of the traction vector on a plane whose normal points in the z direction
σ_{xy}	x component of the traction vector on a plane whose normal points in the y direction ($\sigma_{xy} = \sigma_{yx}$)
η	local isoparametric coordinate
ξ	local isoparametric coordinate, angle of molecular chain rotation
$\dot{\omega}_i$	mass production rate of species i
$\dot{\gamma}$	plastic strain rate
τ	deviatoric stress tensor magnitude
Θ	absolute temperature
μ, λ	Lamé elastic constants
ν	Poisson's ratio
β	Langevin back stress tensor, rate dependent yield stress

1.2 Subscripts and superscripts

m	momentum quantity
d	diffusion quantity
P	point P at the control volume center
g,s	evaluated in the gas at the surface
g,∞	evaluated in the gas far from the interface
i	species index
P	point P at the control volume center
r,s	evaluated in the polymer resist at the surface
e	elastic
p	plastic

2 Introduction

This report describes a new two-dimensional transient computational model of a positive tone silylation process. The model accounts for multispecies diffusion of the silylation and product gases, the silylation chemical reaction, the subsequent swelling and movement of the resist and adjacent materials, and the evolution of the stress state including the kinematics for finite deformations. Although the model is two-dimensional, its extension to three dimensions is straightforward. Material properties and constants were estimated from the literature. The ability of the model to predict accurate quantitative behavior will depend on the collection of more precise material property data.

2.1 Background

Photolithography and its related chemical processing steps are expected to have an essential role in the development of next-generation semiconductor devices. Extreme Ultraviolet Lithography (EUVL) has been demonstrated as a viable candidate for fabrication of integrated circuits having feature sizes of 130nm or less. Due to the strongly absorbing nature of 13.4nm radiation, thin layer imaging (TLI) resist technology is utilized by EUVL. In TLI, an imaging mask layer is placed over a bottom layer photoresist. The top layer is then irradiated causing the photochemical transfer of the mask image to the top surface of the photoresist. Henderson *et al.* [1] discuss several TLI processes. The imaged pattern in the top thin layer of resist is then pattern transfered into the remaining resist thickness using an anisotropic plasma etch step.

The post-exposure silylation process, also referred to as top surface imaging (TSI), is one of several viable processes being proposed for TLI (see *e.g.* reference [1]). Like other TLI methods, TSI is an excellent match to EUVL because it allows thick resist layers to be patterned despite the limited penetration depth of the incident radiation (see *e.g.* reference[1]).

The critical steps of TSI include exposure, post-exposure bake, silylation, and etch development. These steps have an influence on process sensitivity, contrast, and resolution. Depending on the chemistry of the photoresist, either the exposed (negative tone) or unexposed (positive tone) regions can be selectively silylated. During the silylation step, gaseous aminosilanes are absorbed at the resist surface and diffuse into the imaging layer. A reaction takes place in the layer that results in an uptake of silicon, localized increases in volume, and the evolution of a product gas. Volume increases on the order of one hundred percent are typical which results in the development of complex stress states in the resist material. These volume increases can influence the effectiveness of subsequent processing steps (*e.g.* etch development). Attempts to control swelling of the resist during silylation are discussed by Han *et al.* [2]. Researchers who have examined the behavior of materials undergoing TSI include La Tulipe *et al.* [3], Horn, *et al.* [4], Itani, *et al.* [5], Glezos *et al.* [6], Whelan, *et al.* [7], Zuniga and Neureuther [8], Ocola and Cerrina [9], and Henderson *et al.* [1].

2.2 Earlier Work

Early silylation modeling efforts represented silylation solely as a diffusion/reaction process. Weiss and Goethals [10] utilized a modified version of the Deal-Grove oxidation model [11] to simulate the one-dimensional propagation of a silylation front as a function of time for negative tone resists. Bauch *et al.* [12] studied the silylation process experimentally and numerically using a two-dimensional diffusion model. They used an equilibrium balance between sorption, desorption and diffusion as a boundary condition at the gas/resist boundary. The influence of resist glass transition temperature on the diffusion mechanism was examined by Hartney *et al.* [13] and Paniez *et al.* [14]. They observed that, while Fickian diffusion may be appropriate below the glass transition temperature, Case II diffusion is more likely above it. This point is discussed in more detail in Section 4. A comprehensive diffusion-based silylation model was proposed by Pierrat [15]. His model accounted for the reaction of the silylating agent with the resist polymer and the relaxation rate of the polymer after reaction. The diffusion coefficient of the silylating agent was calculated as a function of the relaxed polymer chain concentration.

The models described above do not account for swelling of the resist during silylation. Such swelling can increase diffusion path lengths, induce stresses which affect the mode of diffusion (Fickian versus Case II), and result in shape changes which can influence subsequent processing steps. A more comprehensive model of the silylation process must couple the effects of diffusion and large deformations in the material. Winters and Mason [16, 17] proposed a computational model for heat conduction (diffusion of heat) and material motion for the purpose of modeling coupled thermal-mechanical phenomena. The silylation model proposed here is an extension of their technique. Dimitrienko [18] developed a fully coupled model to determine the effect of finite deformations on internal heat and mass transfer in elastomer ablating materials.

To the authors' knowledge, the only silylation model to date which couples diffusion of the silylation agent to the subsequent growth of the silylated medium was proposed by Zuniga and Neureuther [19]. Their model accounted for the relaxation of the polymer during silylation, the increase in diffusion rate after silylation and a slowing of the local silylation reaction due to the stress induced by swelling. They chose a variable diffusion coefficient similar to Pierrat's [15] to account for an increase of diffusion through the silylated medium. A silylation reaction rate was proposed that depended on the change of state achieved in the resist upon exposure and was proportional to the number of bonding sites available for the silylating agent. The reaction rate was also influenced by the stress generated during silylation. A detailed description of the constitutive equations and kinematics of the model was not given.

2.3 Report Overview

In the sections which follow, the details of a new two-dimensional transient silylation model will be presented. Model formulation, numerical implementation issues, results, and recommendations for future work are discussed.

Section 3 describes the silylation process and its relationship to other TSI processing steps. Formulation of the silylation model is presented in Section 4 including all appropriate equations and boundary conditions. Solution of the coupled set of governing equations is discussed in Section 5. Section 6 presents several model verification studies and results from a 2D silylation analysis. Concluding remarks and recommendations for future work are presented in Section 7. A one-dimensional transient silylation model based on the model of Zuniga and Neureuther [19] is documented in Appendix A.

3 Problem Description

This section will describe the TSI process with an emphasis on the silylation step. The nomenclature and terminology introduced here will be used in the discussion presented in later sections. Much of what follows is a summary of information presented by Wheeler, *et.al.* [20].

3.1 TSI Processing Steps

A schematic showing the TSI processing steps and structure cross-sections are shown in Figure 1. Figure 1 (a) shows the cross-section prior to the first processing step. The cross-section consists of three layers, the substrate (black), an intermediate processing layer (grey) and the top surface imaging layer (white). The processing layer, a hard baked resist typically 400-500 nm thick, functions as a planarizing layer and antireflective coating for the device substrate. The imaging layer, a photoactive resist, is typically 300-400 nm in thickness.

Figure 1 (b) shows the first processing step which consists of applying a mask and irradiating portions of the imaging layer with 13.4 nm radiation. This results in photoinduced acid generation beneath the exposed surface. The cross-section subjected to acid generation is depicted here as the area enclosed by a dashed line. In this scenario, acid generation does not occur through the entire thickness of the imaging layer.

The next step, Figure 1 (c), is the Post Exposure Bake (PEB). A typical PEB occurs for two minutes at a temperature of 400 K. This heating process causes the acid bearing portions of the imaging layer to be highly crosslinked and nearly impermeable to silylation agents. The figure implies uniform crosslinking over the acid bearing region. The actual uniformity and coverage of crosslinked region is uncertain.

Figure 1 (d) shows the silylation step for the positive tone process. Silylation increases the silicon content in certain areas thereby increasing etch selectivity for subsequent processing steps. The top surface of the imaging layer is exposed to a gaseous aminodisilane (silylation agent). Typical processing conditions call for low pressures (20-100 torr) and intermediate temperatures (300-500K) for approximately one minute. The silylating agent diffuses preferentially through the unexposed regions of the imaging layer where a localized chemical reaction occurs causing an uptake of silicon, a change in volume, and the liberation of a product gas. The magnitude and shape of the volume expansion depends on the reaction/diffusion process and the resulting stress state in the material. In Figure 1 (d) the resulting silylation region is shown in red. Shallow silylation depths of approximately 20 nm are generally observed in the exposed areas. Such unwanted silylation is believed to occur because of acid loss during PEB by volatilization from the surface of the resist.

A chlorine/argon plasma "descum" process is used to remove the thin silylated layer in exposed areas. The descum step removes all residues and improves the reproducibility and linearity of the process [20]. Figure 1 (e) shows the device cross-section after completion of the descum step.

The final step in TSI is the oxygen plasma etch, shown here in Figure 1 (f). The presence of silicon in the unexposed portions of the imaging layer restricts etch penetrations to the exposed areas.

The objective in TSI is to transfer the irradiated mask image to a thin imaging layer so that subsequent processes can be restricted to cross-sections which lie beneath either the exposed or unexposed areas. Figure 1 represents an "idealization" of the TSI process in that all processing steps result in process boundaries which are perfectly orthogonal to a "flat" top surface. In reality, the process boundaries may be far from orthogonal due to aerial image aberrations such as light scattering, nonuniform acid generation, nonuniform cross-linking, multidimensional diffusion of the silylating agent, multidimensional growth and deformation of the layer materials and multidimensional etching. Figure 2 illustrates this point by showing a cross-sectional plasma stain made after the silylation process and prior to the plasma etch. The series of equally spaced "bumps" along the top portion of the silylated resist correspond to the unexposed portions where silylation and volume expansion have taken place. Note also the presence of an unwanted Silylation "scum" layer in the exposed regions.

3.2 Silylation Modeling Considerations

The silylation model documented here is intended to represent the part of the TSI process which occurs after the PEB and before the descum step, see *e.g.* Figure 1 (d). This model does not predict the location and distribution of the crosslinking profile prior to silylation. Rather, this profile represents an initial condition for silylation modeling computations. The model can accommodate any crosslinking profile provided it is known a priori. The precise location of the crosslinking boundary, the uniformity of crosslinking, and the effectiveness of the crosslinked region in inhibiting diffusion and reaction of the silylating agent are not well known.

Zuniga and Neureuther [19] have postulated that the potential for silylation can be calculated as a function of polymer characteristics, processing and imaging conditions. In their modeling they assumed that crosslinking could be related to energy deposition during imaging. They utilized a numerical simulation (see *e.g.* [21]) to compute the energy deposition and ultimately the crosslinking profile.

While the present model is capable of treating diffusion mechanisms ranging from pure Fickian to more complex mechanisms which depend on local stress states and reaction rates, the precise nature of diffusion during silylation is not well known. Furthermore, model parameters such as diffusion coefficients and reaction rates have not been measured for most of the resists under consideration for TSI.

The present silylation model couples the complex effects of diffusion, volume change and finite deformation stress development for the silylation and crosslinked portions of the imaging layer. Furthermore, the model includes the compliance of the planarizing layer and device substrate when necessary, to compute stresses and deformations over the entire cross-section of the device. Accurate model predictions require knowledge of mechanical material parameters throughout the device cross-section. At the present time, many of these parameters can only be estimated from similar materials.

Until precise experiments can be designed to determine diffusion and reaction mechanisms and to measure transport and material parameters, predictions from this or any other silylation model must be regarded as qualitative. Nevertheless, the present model should be extremely valuable in assessing a wide range of silylation processing scenarios.

4 Model Formulation

The present silylation model couples the effects of silylating agent and reaction product mass transfer, silylation reaction, volume change, stress generation, and finite deformation of the device cross-section. This section describes the formulation of the mass transport equations, the equation of motion (momentum), and the expression for unconstrained (stress-free) volumetric expansion due to silylation chemistry. Also included is a discussion of boundary conditions and sub-models for material constitutive behavior and mass diffusion. The formulation presented here is geometry independent.

4.1 Mass Transfer and Chemistry

The silylation process studied incorporates silicon into the unexposed (and uncrosslinked) areas of the resist (typically a cresol novolac) thereby rendering those areas resistant to subsequent etching; phenomena include diffusion, chemical reaction, and large (100%) volume change of material. The process takes place in a closed, isothermal chamber that is maintained at a temperature of 70-80 C and filled with a silylating gas (e.g., dimethylaminopentamethyldisilane, DMAPMDS) to a pressure of approximately 30 Torr (*cf.* reference [20]).

In the model the silylating gas is assumed to be adsorbed onto the unexposed surface of the resist; once absorbed the silylating reagent (denoted by A) diffuses into the unexposed and unsilylated polymer resist material (denoted by C), reacts with it forming unexpanded, silylated resist (denoted by D) and releasing amines (denoted by B) which diffuse through the material and are desorbed from the resist surface. The silylating reaction considered in this study is given by:

$$A + C \xrightarrow{k_s} B + D \tag{1}$$

A second reaction (polymer relaxation), which accounts for the swelling of the resist due to the mass addition included in the silylating reaction (1), is given by:

$$D \xrightarrow{k_e} E \tag{2}$$

This chemical model has been used by Pierrat [15] and Zuniga and Neureuther [19].

From a material modeling point of view, it is desirable to represent the process in a Lagrangian reference frame, i.e., a reference frame moving with the deforming material. The derivation below accomplishes this; however, diffusion of the silylating reagent, A, and the product species, B, of the silylating reaction is allowed to take place across the system (consisting of species C and, after chemical reactions (1) and (2), species D and E as well) boundaries.

4.1.1 Species Mass Conservation Equations

The approach adopted here for species mass conservation is the arbitrary moving control volume approach of Whitaker [22] where the control volume velocity is $\mathbf{w}_{\text{arb}}$ (*cf.* Figure 3). This approach yields the following equation for mass conservation of species i :

$$\frac{d}{dt}\int_{V_a(t)} \rho Y_i dV + \int_{A_a(t)} \rho_i(\mathbf{v}_i - \mathbf{w}_{\text{arb}}) \cdot \mathbf{n} dA - \int_{V_a(t)} \dot{\omega}_i dV = 0 \tag{3}$$

When the velocity of species i equals the velocity of the control volume ($\mathbf{v}_i = \mathbf{w}_{\text{arb}}$) this equation becomes:

$$\frac{d}{dt}\int_{V_a(t)} \rho Y_i dV - \int_{V_a(t)} \dot{\omega}_i dV = 0 \tag{4}$$

Since we choose a condition that restricts the unsilylated and unexposed material C to remain within the moving volume, the control volume velocity, $\mathbf{w}$, is not arbitrary; indeed it must equal the velocity of species C, $\mathbf{v}_C$. Reactions (1) and (2) form D and E, and these materials are also contained within the moving volume so that:

$$\mathbf{v}_C = \mathbf{v}_D = \mathbf{v}_E = \mathbf{w}. \tag{5}$$

The velocity, $\mathbf{w}$, of the control volume is in general not the mass average velocity, $\mathbf{v}$. We define diffusion in the usual way relative to the mass average velocity, $\mathbf{v}$:

$$\mathbf{j}_i = \rho Y_i(\mathbf{v}_i - \mathbf{v}) = \rho Y_i \mathbf{V}_i \tag{6}$$

where

$$\mathbf{V}_i = \mathbf{v}_i - \mathbf{v}. \tag{7}$$

is the diffusion velocity of species i. Note that the sum of the mass diffusion fluxes must be zero, that is:

$$\sum \mathbf{j}_i = 0. \tag{8}$$

Equations (5), (6), and (8) can be combined to yield:

$$\mathbf{v}-\mathbf{w}=\frac{\mathbf{j}_A+\mathbf{j}_B}{\rho_C+\rho_D+\rho_E}. \tag{9}$$

The mass conservation equations of materials C, D, and E which remain within the moving control volume $V_p(t)$ (shown in Figure 4 as a two-dimensional quadrilateral control volume centered about point P) are given (for mass production rates that are constant over the control volume) by:

$$\frac{dm_{C_p}}{dt} = \dot{\omega}_{C_p} V_p(t) \tag{10}$$

$$\frac{dm_{D_p}}{dt} = \dot{\omega}_{D_p} V_p(t) \tag{11}$$

$$\frac{dm_{E_p}}{dt} = \dot{\omega}_{E_p} V_p(t). \tag{12}$$

Note that although there can be diffusion of materials C, D, and E across the moving control volume boundary (e.g., $\mathbf{V}_C \equiv \mathbf{v}_C - \mathbf{v} = \mathbf{w} - \mathbf{v} \neq 0$), there is an equal and opposite flux of these materials convected across the moving control volume boundary by the mass average velocity, $\mathbf{v}$, resulting in zero net transport of materials C, D, and E across the boundary.

There is a flux of materials A and B across the boundary of the moving control volume; the mass conservation equations for A and B are given by:

$$\frac{dm_{A_p}}{dt} = \dot{\omega}_{A_p} V_p(t) - \int_{A_p(t)} \left[\mathbf{j}_A + \frac{\tilde{\rho}_A \epsilon_A (\mathbf{j}_A + \mathbf{j}_B)}{(\tilde{\rho}_C \epsilon_C + \tilde{\rho}_D \epsilon_D + \tilde{\rho}_E \epsilon_E)}\right] \cdot \mathbf{n} dA \tag{13}$$

$$\frac{dm_{B_p}}{dt} = \dot{\omega}_{B_p} V_p(t) - \int_{A_p(t)} \left[\mathbf{j}_B + \frac{\tilde{\rho}_B \epsilon_B (\mathbf{j}_A + \mathbf{j}_B)}{(\tilde{\rho}_C \epsilon_C + \tilde{\rho}_D \epsilon_D + \tilde{\rho}_E \epsilon_E)}\right] \cdot \mathbf{n} dA. \tag{14}$$

The quantity $\tilde{\rho}_i$ is the intrinsic density of species i (grams i /(cm^3 i)); ϵ_i is the volume fraction of species i (volume i /volume mixture), and $\mathbf{j}_A$ and $\mathbf{j}_B$ are the mass diffusion fluxes of species A and B, respectively.

4.1.2 Unconstrained Volume Equation

There can be significant volume change of the resist during silylation. Estimates made by Wheeler et al. [20] of volume changes of a cresol novolac resist silylated completely using various silylating agents ranged from 12% to 124%; these estimates were based on the change in the number of atoms in the repeat unit of the polymer.

If the intrinsic densities, $\tilde{\rho}_i$ (grams i/cm^3 i), of the species are assumed to be constant and if the volume fractions of the species sum to one ($\sum \epsilon_i = 1$), then the species mass conservation Equations (10)-(14) can be added to give an explicit equation for the time rate of change of the volume of the moving control volume:

$$\frac{dV_p(t)}{dt} = \sum_k \frac{\dot{\omega}_{kp}}{\tilde{\rho}_k} V_p(t) - \int_{A_p(t)} \left[\frac{\mathbf{j}_A}{\tilde{\rho}_A} + \frac{\mathbf{j}_B}{\tilde{\rho}_B} + \frac{(\epsilon_A + \epsilon_B)}{(\tilde{\rho}_C \epsilon_C + \tilde{\rho}_D \epsilon_D + \tilde{\rho}_E \epsilon_E)} (\mathbf{j}_A + \mathbf{j}_B) \right] \cdot \mathbf{n} dA. \tag{15}$$

This equation describes the unconstrained volumetric expansion due to silylation.

4.1.3 Chemical Production Rates

The silylation reaction (1) assumes that one molecule of the silylating agent A reacts with one repeat unit of the unexposed and uncrosslinked polymer C to form one molecule of product species B and one repeat unit of silylated, unexpanded polymer D. The relaxation reaction (2) implies there is a time scale associated with swelling of the silylated polymer ([15], [19]). The mass production rates of the species are given by:

$$\dot{\omega}_A = -\frac{k_s \rho_A \rho_C}{M_C} \tag{16}$$

$$\dot{\omega}_B = \frac{k_s \rho_A \rho_C M_B}{M_A M_C} \tag{17}$$

$$\dot{\omega}_C = -\frac{k_s \rho_A \rho_C}{M_A} \tag{18}$$

$$\dot{\omega}_D = \frac{k_s \rho_A \rho_C M_D}{M_A M_C} - k_e \rho_D \tag{19}$$

$$\dot{\omega}_E = \frac{k_e \rho_D M_E}{M_D} \tag{20}$$

where the units of k_s are cm^3/mole-sec and the units of k_e are sec^{-1}. Zuniga and Neureuther [19] allowed the silylation rate constant to depend exponentially on the stress in the resist. They referred to the work of Hartney [23] who postulated that a silylation front propagates into the resist by a Case II diffusion mechanism ([24], [25]) in which the silylation rate depends exponentially on stress when that stress exceeds a critical swelling stress ([26]). We note that in the results presented later in this study the silylation rate constant k_s is assumed to be constant; if warranted the present model can be modified easily to allow a stress dependent rate constant (cf. Appendix A).

4.1.4 Diffusion Flux Expressions

The mass diffusion fluxes discussed above are given for species A and B by:

$$\mathbf{j}_A = -\rho\mathcal{D}\nabla(m_A/m) = -\rho\mathcal{D}_o e^{(w\rho_E/M_E)}\nabla(m_A/m) \tag{21}$$

and

$$\mathbf{j}_B = -\rho\mathcal{D}\nabla(m_B/m) = -\rho\mathcal{D}_o e^{(w\rho_E/M_E)}\nabla(m_B/m) \tag{22}$$

Equation (21) is similar to expressions given in [15] and [19]; for $w = 0$ Equations (21) and (22) are expressions of Fick's law (where for lack of data we have assumed equal diffusion coefficients for A and B). Pierrat [15] proposed the exponential dependence of the diffusion coefficient on the expanded, silylated resist concentration c_E, arguing that the diffusion coefficient should be larger in the silylated areas due to the swelling and decreases in density and glass transition temperature of the polymer that occur in the silylation process. Note that Crank [27] assumed an exponential dependence of the diffusion coefficient on penetrant concentration to describe non-Fickian diffusion in polymers.

4.1.5 Initial and Boundary Conditions

The dependent variables in Equations (10)-(15) are the masses of the species and the volume of the control volume; thus the initial and boundary conditions depend on volume. For example, for a control volume centered about point P (cf. Figure 4), $m_{i_P}(t) = \rho_{i_P}(t)V_P(t)$. Since initial and boundary conditions are usually specified in terms of concentration, the discussion here will refer to (mass) concentration; conversion to species masses takes place in the computer code after discretization when the volumes are available.

The initial conditions for the species mass conservation equations in the region where silylation is allowed to occur state that only C is present: $\rho_C(\mathbf{x},0)$ is specified and $\rho_A(\mathbf{x},0) = \rho_B(\mathbf{x},0) = \rho_D(\mathbf{x},0) = \rho_E(\mathbf{x},0) = 0$.

Boundary conditions are required for species A and B. For all boundaries other than the gas/polymer interface, the boundary conditions are zero normal fluxes of species A and B: $\mathbf{j}_A \cdot \mathbf{n} = \mathbf{j}_B \cdot \mathbf{n} = 0$.

At the gas/polymer interface two types of boundary conditions are implemented. For the first type, a fixed concentration of A and zero concentration of B are specified: $\rho_{A_{r,s}}$ is specified and $\rho_{B_{r,s}} = 0$. For the second type, a steady-state mass balance that includes an equilibrium assumption at the surface is the specified boundary condition for A; zero concentration of B is again specified. This second type of boundary condition for A is a flux boundary condition that can be explained with respect to the gas/polymer interface shown in Figure 5.

As the thickness (Δy) of the control volume containing the surface shown in Figure 5 shrinks to zero, the mass balance for the silylating agent A is:

$$\dot{m}_{A_g} = \dot{m}_{A_r} \tag{23}$$

where $\dot{m}_{A_r}$ is the mass flux of silylating agent A at the surface into the resist and $\dot{m}_{A_g}$ is the mass flux of silylating gas A into the surface from the gas, which can be given by:

$$\dot{m}_{A_g} = K_g(p_{A_{g,\infty}} - p_{A_{g,s}}) \tag{24}$$

where K_g is the mass transfer coefficient (in appropriate units), $p_{A_{g,\infty}}$ is the partial pressure of A far from the interface, and $p_{A_{g,s}}$ is the partial pressure of A in the gas phase at the gas/polymer interface. At the interface, equilibrium is assumed and the partial pressure $p_{A_{g,s}}$ is related to the mass fraction $Y_{A_{r,s}}$ ($Y_A \equiv \rho_A/\rho$) of species A in the resist at the surface by (Middleman [28]):

$$p_{A_{g,s}} = \frac{HY_{A_{r,s}} M_{\text{mixture}_{r,s}}}{M_A} \tag{25}$$

where H is Henry's constant (a function of temperature). Combining (24) and (25) yields:

$$\dot{m}_{A_g} = K_g \left(p_{A_{g,\infty}} - \frac{HY_{A_{r,s}} M_{\text{mixture}_{r,s}}}{M_A} \right) \tag{26}$$

which gives an equation for the unknown mass fraction (or concentration) of A at the surface of the resist in terms of the parameters K_g and H and the specified chamber pressure $p_{A_{g,\infty}}$.

4.2 Momentum

The material motion is obtained from the conservation of momentum, *i.e.*,

$$\frac{\partial(\rho \mathbf{v})}{\partial t} = \nabla \cdot \sigma + \mathbf{F} \tag{27}$$

where ρ, $\mathbf{v}$, σ and $\mathbf{F}$ are the material density, velocity, stress, and body forces respectively. The body force is included here for completeness. The only applicable body force for the silylation problem is that due to gravity which is neglected in the numerical implimentation. The inertia term on the left hand side of Equation (27) is also negligible since the material motion is quasi-static. For reasons explained in Section 5, a portion of this term will be retained to facilitate an explicit time integration for $\mathbf{v}$, the principal dependent variable in Equation (27). The material velocity can be related to the stress through the deformation rate tensor. This relationship varies depending on the kinematics and constitutive model employed (see Section 4.3).

Boundary conditions imposed on the equation of motion are straightforward. At the free surface of the imaging layer, the velocity field is computed in such a way as to insure the following stress free boundary condition:

$$\sigma \cdot \mathbf{n} = 0 \tag{28}$$

were $\mathbf{n}$ is the unit normal to the surface.

The interfaces between the imaging layer, processing layer, and device substrate are assumed to be bonded together and hence part of the interior computed solution, *i.e.*, there is no need to provide boundary conditions for material interfaces.

At some depth sufficiently far from the free surface, the material is immobile such that the following boundary condition holds:

$$\mathbf{v} = 0 \tag{29}$$

Boundary conditions placed on the in-plane and lateral directions of the device cross-section depend on whether the analysis is three-dimensional, two-dimensional, or axisymmetric. For the two-dimensional planar model developed here, symmetry boundary conditions are assumed.

4.3 Polymer Material Response

This subsection discusses the polymer constitutive model. The physical deformation mechanisms, model kinematics, inelastic flow rule, evolution law, and backstress models are formulated in the sections which follow.

4.3.1 Physical Deformation Mechanisms

To deform inelastically, polymers must overcome two distinct internal resistances. Initially, the flow strength is controlled by an internal resistance to deformation-induced rotation of the individual molecular chains that comprise the microstructure. This resistance corresponds to breaking bonds connecting randomly oriented nearest neighbor polymer chains. Subsequently, chains undergo affine rotation and realign at larger strains. As the polymer deforms into this more orderly state, an additional resistance must now be overcome corresponding to this increase in configurational entropy.

Often, polymer resists are described by a viscoelastic constitutive law. Further, the recoverable elastic strains are almost always small. As such, the material response is well-represented by a viscous element in parallel with an elastic spring. Below the glass transition temperature, however, the viscosity of the inelastic element is very large with a correspondingly large time constant for relaxation of any of the inelastic strains[1]. So while a viscoelastic constitutive law is often used, the apparent permanence of strain below the glass transition temperature makes a simpler viscoplastic law sufficient.

4.3.2 Kinematics

Glassy polymers can, in general, exhibit both elastic and inelastic deformation. In what follows, we exercise the inelastic glassy polymer model developed by Boyce, Parks & Argon and described in detail in [30]. The formulation used here is restricted to small elastic strains while allowing for arbitrarily large inelastic deformation. The motion is prescribed by a multiplicative decomposition of the total deformation gradient into elastic and plastic parts

$$\mathbf{F} = \mathbf{F}^{\bullet}\mathbf{F}^{p} = \mathbf{V}^{\bullet}\hat{\mathbf{R}}\mathbf{U}^{p} \tag{30}$$

where **V** and **U** are the left and right stretch tensors, respectively.

Further restricting the elastic deformation gradient to be symmetric

$$\mathbf{F}^{\bullet\mathbf{T}} = \mathbf{F}^{\bullet} = \mathbf{V}^{\bullet} \tag{31}$$

the plastic deformation gradient

$$\mathbf{F}^{p} = \hat{\mathbf{R}}\mathbf{U}^{p} \tag{32}$$

then describes the relaxed configuration upon elastic unloading to a stress free state ***without*** rotation. It follows that the velocity gradient may be written

---

[1] "Because the internal viscosity is relatively high, only a small part of the deformation is recovered at normal temperatures so that the plastic deformations have the appearance of permanence." [29]

$$\mathbf{L} = \dot{\mathbf{V}}^{\bullet}\mathbf{V}^{\bullet -1} + \mathbf{V}^{\bullet}\left[\mathbf{D}^{p} + \mathbf{W}^{p}\right]\mathbf{V}^{\bullet -1} \tag{33}$$

where $\mathbf{D}^{p}$ and $\mathbf{W}^{p}$ are, respectively, the symmetric and skew parts of the plastic velocity gradient, known respectively as the plastic rate of deformation and the plastic spin.

The Cauchy stress, $\boldsymbol{\sigma}$, is uniquely defined by the natural logarithm of the elastic deformation gradient

$$\sigma = \frac{1}{\det(\mathbf{V}^{\bullet})}\mathcal{C}^{\bullet} : [\ln\{\mathbf{V}^{\bullet}\} - (\alpha_{\theta}\Delta\Theta + \Delta\Phi)\mathbf{I}] \tag{34}$$

where the volumetric terms are the thermal and silylation swelling , respectively, and the elastic modulus tensor is given by

$$\mathcal{C}^{\bullet} = 2\mu\mathbf{II} + \lambda\mathbf{I}\otimes\mathbf{I} \tag{35}$$

where μ and λ are the elastic Lamé constants and **II** and **I** are, respectively, the fourth and second order identity tensors. The swelling $\Delta\Phi$ is the net unconstrained volumetric expansion calculated from Equation (15) For small elastic strains, the development by Hoger [31] can be used to show that

$$[\ln(\mathbf{V}^{\bullet})]^{\bullet} \approx \mathbf{D}^{\bullet} \tag{36}$$

where $\mathbf{D}^{\bullet}$ is the elastic deformation rate tensor. Using the finite deformation kinematics outlined in Bammann & Johnson [32] and Bammann & Aifantis [33], a rate formulation for the Cauchy stress can be written as

$$\hat{\sigma} = \dot{\sigma} - \mathbf{W}^{\bullet}\sigma + \sigma\mathbf{W}^{\bullet} \approx \mathcal{C}^{\bullet} : [ln\mathbf{V}^{\bullet}]^{\bullet} = \mathcal{C}^{\bullet} : \mathbf{D}^{\bullet} \tag{37}$$

where

$$\mathbf{D}^{\bullet} = \mathbf{D} - \mathbf{D}^{p} - \{\alpha\dot{\Theta} + \dot{\Phi}\}\mathbf{I} \tag{38}$$

and

$$\mathbf{W}^{\bullet} = \mathbf{W} - \mathbf{W}^{p} \tag{39}$$

The quantity $\dot{\Phi}$ is the unconstrained silylation strain rate and is determined from:

$$\dot{\Phi} = \frac{1}{V_p(t)} \frac{dV_p(t)}{dt} \tag{40}$$

where $\frac{dV_p(t)}{dt}$ is determined from Equation (15).

For small elastic strains and, owing to the symmetric choice for $\mathbf{F}^{\bullet}$[30],

$$\mathbf{W}^{\mathrm{p}} \approx \mathbf{W} \tag{41}$$

and[2]

$$\dot{\sigma} = \mathcal{C}^{\bullet} : \mathbf{D}^{\bullet} \tag{42}$$

4.3.3 Inelastic Flow Rule for Polymer Segment Rotation

The initial resistance to polymer deformation has its origin in the restriction imposed on molecular chain rotation from neighboring chains as depicted in Figure 6. Inelastic deformation commences once a free energy barrier to molecular mobility is surpassed. This barrier is overcome by thermally activated rotation of chain segments under stress. The result is a Boltzmann expression for the inelastic deformation rate magnitude

$$\dot{\gamma}^p = \dot{\gamma}_o \exp\left[\frac{-As}{\Theta}\left\{1 - \left(\frac{\tau}{s}\right)^{\frac{p}{q}}\right\}\right] \tag{43}$$

where $\dot{\gamma}_o$ is a reference strain rate, s_o is the athermal flow resistance, *i.e.* the resistance at absolute zero, Θ is the absolute temperature, τ is the local stress magnitude, p and q are material parameters and A is a proportionality constant given by

$$A = \frac{39\pi\xi^2 a^3}{16k} \tag{44}$$

Here ξ is the net angle of molecular chain rotation, a is the mean molecular radius and k is Boltzmann's constant.

---

[2] NOTE: The approximation resolved in (41) indicates that $\mathbf{W}^{\bullet} \approx \mathbf{0}$. Under an arbitrary superposed rotation, $\tilde{\mathbf{Q}}(t)$, $\tilde{\mathbf{W}}^{\mathbf{e}}$ would be given by $\tilde{\mathbf{W}}^{\mathbf{e}} = \dot{\tilde{\mathbf{Q}}}(t)\tilde{\mathbf{Q}}^{\mathrm{T}}(t)$ thus guaranteeing that the rate expression in (37) remains objective.

A typical illustration of this strain rate dependence on stress is given in Figure 7. In this example, an Eyring dashpot element would exhibit negligible strain for stresses below the temperature-dependent yield, here approximately $25 - 30 \times 10^7$ dynes/cm^2. Above such stresses, the molecular chain segment rotation becomes progressively easier resulting in a strain rate that increases rapidly with stress.

We assume an associative flow rule with the plastic deformation rate and deviatoric stress coaxial

$$\mathbf{D}^p = \dot{\gamma}^p \mathbf{N} \tag{45}$$

$$\mathbf{N} = \frac{\sigma'}{|\sigma'|} \tag{46}$$

4.3.4 Evolution Law

The response of glassy polymers is characterized by stress relaxation after yield. The stress relaxation is modeled by allowing the internal resistance to decrease with continued straining. The Voce-type phenomenological softening evolution described in [30] is used here

$$\dot{s} = h\{1 - \frac{s}{s_{ss}}\}\dot{\gamma}^p \tag{47}$$

where s is the current athermal deformation resistance in the Eyring dashpot, s_{ss} is the steady state value at large strain and h is the softening modulus, *i.e.* the slope of the yield drop with respect to inelastic strain. The initial value of this athermal resistance is given by

$$s_o = \frac{0.077\mu}{1 - \nu} \tag{48}$$

The difference between the initial yield and the saturation value of the dashpot resistance is the value of the total stress relaxation in uniaxial extension. In this way, the characteristic time constant for the inelastic response is determined by the model parameters h and s_{ss}. A typical strain-induced yield drop during volumetric swelling will be illustrated in the section describing individual response modes.

4.3.5 Resistance to Changes in Configurational Entropy

At very large strain, there is a second contribution to resistance to inelastic deformation. Associated with large rotations of long chain molecules is a change in configurational entropy that corresponds to resistance of the bulk polymer to large scale alignment and ordering of the molecular chains. In [30], a highly nonlinear Langevin spring element represents the locking behavior consistent with a non-Gaussian statistical mechanics description of rubber elasticity. In this formulation, an internal back stress develops in the polymer chain network as illustrated in Figure 6. This internal stress represents the ever increasing stress locked in the aligned structure, *i.e.* the stress beyond which the polymer must be loaded to further strain and align the chain network so that now the constitutive law becomes

$$(\sigma - \beta)^{\bullet} = \mathcal{C}^{\circ} : \mathbf{D}^{\circ} \tag{49}$$

The back stress is assumed to remain coaxial with the left plastic stretch tensor, V^p, with principal values given by

$$\beta_i = C^R \frac{\sqrt{N}}{3}\left[V_i^p \mathcal{L}^{-1}\left(\frac{V_i^p}{\sqrt{N}}\right) - \frac{1}{3}\sum_{j=1}^{3} V_j^p \mathcal{L}^{-1}\left(\frac{V_j^p}{\sqrt{N}}\right)\right] \tag{50}$$

where

$$\mathbf{F}^{\mathrm{p}} = \hat{\mathbf{R}}\mathbf{U}^{\mathrm{p}} = \mathbf{V}^{\mathrm{p}}\hat{\mathbf{R}} \tag{51}$$

$$\mathbf{V}^{\mathrm{p}} = V_k^p \ell_k \otimes \ell_k \tag{52}$$

and N is the number of rigid chain links between entanglements. C^R is the rubbery modulus, and $\mathcal{L}$ is the Langevin function given by

$$\mathcal{L}(\eta_i) = \coth(\eta_i) - \frac{1}{\eta_i} = \frac{V_i^p}{\sqrt{N}} \tag{53}$$

This locking behavior is shown in Figure 8 where the nonlinear behavior of the Langevin function is illustrated. Effectively, the alignment of polymer chains requires increasingly larger stresses. Because the strength of the back stress is proportional to the rigid chain link density, this spring element provides an appealing means of modeling crosslinked polymers through its observed locking behavior.

Because the swelling strains have been shown to be of order unity, we describe this element of the complete model for illustration. However, as the locking behavior may not be realized by silylating polymer resists and because it has no counterpart in viscoelastic material models, this element is not exercised in simulations reported here.

5 Solution Method

This section describes the numerical implementation of the silylation model for two-dimensional (2D) transient problems. The equations formulated in Section 4 are reduced to a set of first order ordinary differential equations that can be explicitly integrated in time. The computational space is discretized into 2D Lagrangian finite elements and all conservation equations are solved simultaneously on the same moving mesh. The model has been formulated so that each element contains a volume of solid mass that may or may not undergo a chemical transformation depending on the material type and whether it is crosslinked. During a simulation, no solid mass is permitted to cross the boundaries of an element. The element may, however, deform and grow in volume due to silylation. All mass transport across the boundaries of an element is due to diffusion and convection of the silylation agent and reaction product.

Figure 9 shows a typical four node quadrilateral element in the global 2D planar ($x-y$) coordinate system. Each element is assumed to have a uniform and constant thickness of unity in the z direction (the plane strain assumption). The goal in finite element discretization is to obtain a set of ordinary differential equations for the dependent variables at each node in the mesh. The dependent variables include the nodal masses of all five species, the unconstrained (stress-free) nodal volume expansion rate, the x and y components of nodal velocity, and the x and y nodal displacements. Equations for nodal masses and volume expansion rate are obtained from a control volume finite element discretization of the mass conservation equations (see Section 5.1). Equations for nodal velocities are obtained from a traditional Galerkin one-point-quadrature finite element discretization of the momentum equation (see Section 5.2).

Typically, nodes are shared by several adjacent elements. Thus the element contributions to a nodal variable equation must be superimposed in order to determine the complete equation for each nodal variable. Adding these contributions is commonly referred to in the finite element literature (*e.g.* [34]) as the "assembly process." After the assembly process is compete, explicit time integration for the nodal masses, unconstrained nodal volume rate, and nodal velocities can then take place.

The stress rate in each element is computed at the single Gauss-point from the deformation rate tensor and the Gauss-point interpolated unconstrained volume expansion rate (see Section 5.3). The stress, x displacement, and y displacement are obtained from a straightforward explicit time integration of the stress rate, x velocity and y velocity. Explicit time integration and time stepping is discussed in Section 5.4.

Before proceeding to Sections 5.1 and 5.2, it is useful to introduce a few concepts. The four node quadrilateral elements used in the numerical implementation of the silylation model employ the following equation for spatial interpolation:

$$\Phi = \sum_{I=1}^{4} \Phi_I N_I \tag{54}$$

where I is the node number, N is the bilinear shape function, and Φ is the nodal dependent variable (mass, volume rate, or velocity).

The global $x - y$ coordinate system shown in Figure 9 is transformed into the isoparametric local $\xi - \eta$ coordinate system shown in Figure 10. Mapping of points between the $x - y$ and $\xi - \eta$ coordinate systems is accomplished using the following equations:

$$x(\xi, \eta) = \sum_{I=1}^{4} N_I(\xi, \eta) x_I \tag{55}$$

$$y(\xi, \eta) = \sum_{I=1}^{4} N_I(\xi, \eta) y_I \tag{56}$$

where the bilinear shape function N_I is

$$N_I(\xi, \eta) = \frac{1}{4}(1 + \xi\xi_I)(1 + \eta\eta_I) \tag{57}$$

and x_I and y_I are the x and y coordinates of node I. The values ξ_I and η_I are the coordinates of node I in the $\xi - \eta$ plane shown in Figure 10. Depending on the node number, these values are either -1 or 1.

5.1 Mass Transfer and Chemistry

The species mass conservation Equations (10)-(14) and the unconstrained silylation volume expansion Equation (15) described in Section 4.1 have been discretized and solved on 1D and 2D domains using two different numerical methods. In the absence of stress, Equations (10)-(15) have been solved on a 1D domain using an implicit ODE integrator, DVODE [35], which is a double precision variable coefficient ODE solver for stiff or nonstiff problems. The solution (not shown) compares well with the solution of the model formulation described in Appendix A. The 2D formulation described here has been solved on a 1D domain in the absence of stress; again the results agree well (cf. Section 6) with those obtained from the solution of the 1D formulation.

Equations (10)-(15) have been discretized on a 2D domain using the control volume finite element method (*cf.* [36], [37]). This method has been applied to ablation problems with moving control volumes [38]. The control volume finite element method (CVFEM) applies local conservation principles to the finite element method. Figure 11 shows a four node quadrilateral element that is divided into four regions labeled SCV1 through SCV4; these regions are associated with local nodes 1 through 4 of the element. Each of these nodes corresponds to point P of the control volume shown in Figure 4 (note that if the node is on a boundary, it will not be at the center of the control volume); e.g., if node 1 corresponds to point P then SCV1 is part of the control volume $V_p(t)$ associated with node P, and other parts of the control volume $V_p(t)$ lie in adjacent elements (not shown in Figure 11). The conservation Equations (10)-(15) are discretized on the control volume; however the matrix is assembled on an element by element basis as done in finite element method applications. As an example, the element matrix equation for the conservation of mass of unsilylated polymer resist material C can be written as:

$$[M_c]\{\dot{\Phi}_c\} = \{b_c\} \tag{58}$$

where

$$\{\dot{\Phi}_c\} = \left\{ \begin{array}{c} \dot{m}_{c_1} \\ \dot{m}_{c_2} \\ \dot{m}_{c_3} \\ \dot{m}_{c_4} \end{array} \right\} \tag{59}$$

$$[M_c] = [I] \tag{60}$$

and

$$\{b_c\} = \left\{ \begin{array}{c} \dot{\omega}_{c_1} V_{\mathrm{SCV1}} \\ \dot{\omega}_{c_2} V_{\mathrm{SCV2}} \\ \dot{\omega}_{c_3} V_{\mathrm{SCV3}} \\ \dot{\omega}_{c_4} V_{\mathrm{SCV4}} \end{array} \right\}. \tag{61}$$

Although the left hand side of Equation (58) is written in element matrix form, it is not assembled into a global matrix because the solution method is explicit and the left hand side of Equation (10) is simply the time rate of change of mass of C. The right hand side of the element matrix equation, Equation (61), is assembled from the element level into a global matrix for the mass of C at the nodes by summing the contributions of all the elements to each node. Similar expressions apply for material species D and E .

For the mass conservation Equations (13) and (14) of species A and B and for the unconstrained volume Equation (15), fluxes across control volume boundaries must be evaluated. Referring again to the element shown in Figure 11, the surface areas of the control volumes across which fluxes are determined are labeled ss1 through ss4; the midpoints of these lines are designated as integration points ip1 through ip4; the fluxes are evaluated at the integration points. For example, for the subcontrol volume SCV1 of Figure 11, the contribution of the mass diffusion flux, given in Equation (21), of species A to the total mass diffusion flux of species A (for the control volume centered at node 1) is:

$$\int_{\text{scv1}} \mathbf{j}_A \cdot \mathbf{n} dA = \int_{\text{ss1}} \mathbf{j}_A \cdot \mathbf{n} dA - \int_{\text{ss4}} \mathbf{j}_A \cdot \mathbf{n} dA \tag{62}$$

where

$$\int_{\text{ss1}} \mathbf{j}_A \cdot \mathbf{n} dA = j_{Ax}|_{ip1} \Delta y_1 - j_{Ay}|_{ip1} \Delta x_1 \tag{63}$$

and

$$\int_{\text{ss4}} \mathbf{j}_A \cdot \mathbf{n} dA = j_{Ax}|_{ip4} \Delta y_4 - j_{Ay}|_{ip4} \Delta x_4 \tag{64}$$

In Equations (63) and (64), $\Delta x_1 = x_c - x_{\text{mp1}}$, $\Delta y_1 = y_c - y_{\text{mp1}}$, $\Delta x_4 = x_c - x_{\text{mp4}}$, and $\Delta y_4 = y_c - y_{\text{mp4}}$, where the coordinates of the points (x_c, y_c), $(x_{\text{mp1}}, y_{\text{mp1}})$, and $(x_{\text{mp4}}, y_{\text{mp4}})$ are determined using Equations (55) and (56).

The mass diffusion flux components of species A at the integration points are then given by (cf. Equation (21)):

$$j_{A_x}\Big|_{ip1} = -\rho \mathcal{D}_o e^{(w\rho_E/M_E)}\Big|_{ip1} \sum_{j=1}^{4} \left(\frac{\partial N_j}{\partial x}\bigg|_{ip1} \frac{m_{A_j}}{m_j} \right) \tag{65}$$

$$j_{A_y}\Big|_{ip1} = -\rho \mathcal{D}_o e^{(w\rho_E/M_E)}\Big|_{ip1} \sum_{j=1}^{4} \left(\frac{\partial N_j}{\partial y}\bigg|_{ip1} \frac{m_{A_j}}{m_j} \right) \tag{66}$$

$$j_{A_x}\Big|_{ip4} = -\rho \mathcal{D}_o e^{(w\rho_E/M_E)}\Big|_{ip4} \sum_{j=1}^{4} \left(\frac{\partial N_j}{\partial x}\bigg|_{ip4} \frac{m_{A_j}}{m_j} \right) \tag{67}$$

$$j_{A_y}\Big|_{ip4} = -\rho \mathcal{D}_o e^{(w\rho_E/M_E)}\Big|_{ip4} \sum_{j=1}^{4} \left(\frac{\partial N_j}{\partial y}\bigg|_{ip4} \frac{m_{A_j}}{m_j} \right) \tag{68}$$

where the shape function derivatives are given by:

$$\begin{bmatrix} \frac{\partial N}{\partial x} \\ \frac{\partial N}{\partial y} \end{bmatrix} = [J]^{-1} \begin{bmatrix} \frac{\partial N}{\partial \xi} \\ \frac{\partial N}{\partial \eta} \end{bmatrix} \tag{69}$$

$$J^{-1} = \frac{1}{|J|} \begin{bmatrix} \frac{\partial y}{\partial \eta} & -\frac{\partial y}{\partial \xi} \\ -\frac{\partial x}{\partial \eta} & \frac{\partial x}{\partial \xi} \end{bmatrix} \tag{70}$$

and $|J|$ is the determinant of the Jacobian of the transformation, given by Equation(77) in the next section.

Similar expressions hold for the mass diffusion flux components of B at integration points ip1 and ip4 as well as for the mass diffusion flux components of A and B at integration points ip2 and ip3. The area integrals and source terms on the right hand sides of Equations (13), (14), and (15) are thus evaluated, yielding a right hand side vector for each element. The element right hand side vector is then summed over all nodes in the problem to yield the global right hand side vector, which is the discretization of the right hand side of Equations (13), (14), and (15) for each control volume in the problem. The discretized equations for the conservation of mass of species A, B, C, D, and E at each control volume are then integrated in time as discussed in section 5.4. The discretized equation for the unconstrained volume is not integrated in time; rather it is the *time rate of change* of the unconstrained volume (the discretized right hand side of Equation(15)) that is required by the material model and discussed further in section 5.3.

5.2 Momentum

Chain rule differentiation of the inertia term in Equation (27) yields

$$\dot{\rho}\mathbf{v} + \rho\dot{\mathbf{v}} = \nabla \cdot \sigma + \mathbf{F}. \tag{71}$$

As discussed in Section 4.2, the material motion is quasi-static (negligible inertia). However, to facilitate the time integration for velocity, $\mathbf{v}$, only the first term in Equation (71) is neglected, resulting in

$$\rho\dot{\mathbf{v}} = \nabla \cdot \sigma + \mathbf{F}. \tag{72}$$

The method of weighted residuals (see *e.g.* [34]) is applied to Equation (72) in order to obtain expressions for the contribution of each element's the nodal velocity components. The process begins by casting the momentum equation into the so-called "weak-form" by multiplying its residual by a set of weighting functions, W, and integrating the result over the volume of an element, *i.e.*,

$$\int_V (\rho\dot{\mathbf{v}} - \mathbf{F} - \nabla \cdot \sigma)\mathbf{W}\mathbf{dV} = \mathbf{0}. \tag{73}$$

The method of weighted residuals seeks to approximate the dependent variables (nodal velocities) using simple functional forms like that expressed in Equation (54). The functions are selected in such a way as to minimize the residual in Equation (73) thus approximating the solution over the element domain.

For the planar problem solved here, a special form of the method of weighted residuals referred to as Galerkin's method is used. In Galerkin's method, the weighting functions are chosen to be the same as the shape or interpolation functions in Equation (54), *i.e.* $W = N$. Furthermore, for an assumed element thickness of unity, $dV = dA$, where A is the element area. Thus for the planar problem:

$$\int_A (\rho\dot{\mathbf{v}} - \mathbf{F} - \nabla \cdot \sigma)\mathbf{NdA} = \mathbf{0} \tag{74}$$

Integration of the first two terms in the above equation is straighforward, but the last term requires special treatment because of the spatial gradient operator ∇. The last term is integrated by parts using Green's theorem. This results in two integrals for the third term: an area integral and a line integral, where the line represents the perimeter of the element, *i.e.*:

$$\int_A \rho\dot{\mathbf{v}} N dA - \int_A \mathbf{FNdA} + \int_\mathbf{A} \sigma \cdot \nabla\mathbf{NdA} - \int_\mathbf{S} \sigma \cdot \mathbf{nNdS} = \mathbf{0} \tag{75}$$

The line integrals provide a means of applying the appropriate global boundary conditions. They vanish for all elements which do not have a physical boundary (*i.e.*, all interior elements). The vector $\mathbf{n}$ represents the outward pointing normal to the line S (element side on a physical boundary). Hence in Equation (75), the last term represents the influence of boundary traction and pressure on the boundary elements. As discussed in Section 4.2, this term is zero for the elements along the free surface for the silylation problem.

Integration of Equation (75) proceeds in the $\xi - \eta$ coordinate system (Figure 10 and Equations (55) through (57)) by noting that

$$dA = dxdy = |J|\, d\xi d\eta. \tag{76}$$

where $|J|$ is the determinant of the Jacobian transformation matrix, *i.e.*,

$$|J| = \frac{\partial x}{\partial \xi}\frac{\partial y}{\partial \eta} - \frac{\partial y}{\partial \xi}\frac{\partial x}{\partial \eta}. \tag{77}$$

It can be shown that the determinant of the Jacobian is directly related to the element area,

$$|J| = \frac{A}{4} \tag{78}$$

where the element area is expressed in terms of the element nodal coordinates as

$$A = \frac{(x_3 - x_1)(y_4 - y_2) + (x_2 - x_4)(y_3 - y_1)}{2}. \tag{79}$$

Substituting $\xi - \eta$ transformations into Equation (75) and neglecting the boundary integrals yields,

$$\int_{-1}^{+1}\int_{-1}^{+1} \rho\dot{\mathrm{v}}N\,|J|\,d\xi d\eta - \int_{-1}^{+1}\int_{-1}^{+1} \mathbf{F}\mathbf{N}\,|\mathbf{J}|\,\mathbf{d}\xi\mathbf{d}\eta + \int_{-1}^{+1}\int_{-1}^{+1} \sigma\cdot\nabla\mathbf{N}\,|\mathbf{J}|\,\mathbf{d}\xi\mathbf{d}\eta = 0. \tag{80}$$

Integration of the terms in the above equations is performed numerically at a single Gauss point for which $\xi = \eta = 0$. The "one point quadrature" assumption is a popular simplification (see *e.g.* [16, 39, 40, 41]) that permits $\rho, \mathbf{F}$ and σ to be taken as constant over the element and moved outside of the integral. The element stress tensor, σ, is the time integrated value of the element stress rate tensor which is determined from the deformation rate tensor and the unconstrained volumetric strain rate. The element deformation rate tensor is, in turn, computed from the nodal velocities. The remaining functions inside the integrals such as N_I are easily integrated since, *e.g.*,

$$N_I(\xi, \eta) = N_I(0,0) = \frac{1}{4}. \tag{81}$$

where $I = 1, 2, 3, 4$.

After some algebra, Equation (80) takes the form,

$$\frac{\rho A}{16}[M]\{\dot{\mathbf{v}}\} = \frac{\mathbf{A}}{4}\{\mathbf{F}\} + \frac{1}{2}[\Lambda]\{\sigma\}. \tag{82}$$

The mass matrix $[M]$ is given by

$$[M] = \begin{bmatrix} 1 & 0 & 1 & 0 & 1 & 0 & 1 & 0 \\ 0 & 1 & 0 & 1 & 0 & 1 & 0 & 1 \\ 1 & 0 & 1 & 0 & 1 & 0 & 1 & 0 \\ 0 & 1 & 0 & 1 & 0 & 1 & 0 & 1 \\ 1 & 0 & 1 & 0 & 1 & 0 & 1 & 0 \\ 0 & 1 & 0 & 1 & 0 & 1 & 0 & 1 \\ 1 & 0 & 1 & 0 & 1 & 0 & 1 & 0 \\ 0 & 1 & 0 & 1 & 0 & 1 & 0 & 1 \\ 1 & 0 & 1 & 0 & 1 & 0 & 1 & 0 \\ 0 & 1 & 0 & 1 & 0 & 1 & 0 & 1 \end{bmatrix}. \tag{83}$$

The "lumped" matrix approximation is made for the mass matrix, *i.e.*, each row of the mass matrix is summed and the result placed at the diagonal. Hence,

$$[M] = 4[I] \tag{84}$$

where $[I]$ is the identity matrix.

The column vectors $\{\dot{\mathbf{v}}\}, \{\mathbf{F}\}$ and $\{\sigma\}$ and the matrix $[\Lambda]$ in Equation (82) are given by

$$\{\dot{\mathbf{v}}\} = \left\{ \begin{array}{c} \ddot{u}_1 \\ \ddot{v}_1 \\ \ddot{u}_2 \\ \ddot{v}_2 \\ \ddot{u}_3 \\ \ddot{v}_3 \\ \ddot{u}_4 \\ \ddot{v}_4 \end{array} \right\} \tag{85}$$

$$\{\mathbf{F}\} = \left\{ \begin{array}{c} F_{x1} \\ F_{y1} \\ F_{x2} \\ F_{y2} \\ F_{x3} \\ F_{y3} \\ F_{x4} \\ F_{y4} \end{array} \right\} \tag{86}$$

$$\{\sigma\} = \left\{ \begin{array}{c} \sigma_{xx} \\ \sigma_{yy} \\ \sigma_{xy} \\ \sigma_{zz} \end{array} \right\} \tag{87}$$

$$[\Lambda] = \begin{bmatrix} y_2 - y_4 & 0 & x_4 - x_2 & 0 \\ 0 & x_4 - x_2 & y_2 - y_4 & 0 \\ y_3 - y_1 & 0 & x_1 - x_3 & 0 \\ 0 & x_1 - x_3 & y_3 - y_1 & 0 \\ y_4 - y_2 & 0 & x_2 - x_4 & 0 \\ 0 & x_2 - x_4 & y_4 - y_2 & 0 \\ y_1 - y_3 & 0 & x_3 - x_1 & 0 \\ 0 & x_3 - x_1 & y_1 - y_3 & 0 \end{bmatrix} \tag{88}$$

Equations (82) through (88) represent a set of eight ordinary differential equations that determine the contribution of each element to the nodal accelerations $\ddot{u}_I$ and $\ddot{v}_I$ where $I = 1, 2, 3, 4$. Once the total contribution is determined from the finite element assembly process, $\ddot{u}_I$ and $\ddot{v}_I$ are integrated with respect to time to yield the nodal velocities $\dot{u}_I$ and $\dot{v}_I$. The nodal velocities are then integrated with respect to time to yield the nodal displacements u_I and v_I. For the silylation problem the body forces F_x and F_y due to gravity are neglected.

Spatial integration of elements at a single Gauss point (*i.e.* the one point quadrature used here), though computationally efficient, can lead to the calculation of spurious energy modes. If these modes are not supressed, a severe and usually fatal mesh distortion known as "hourglassing" may occur. The term hourglassing was coined because of the shape taken by adjacent affected elements in structural calculations. The problem arises when a single gauss point is used to calculate the deviatoric part of the stess. When this is done, it is possible for certain element deformations to produce no stress. Such deformations are commonly refered to as "zero energy modes."

A number of procedures have been developed to eliminate hourglassing (see *e.g.* [42, 43, 44]). In the present work, the method of Flanagan and Belytschko [43, 44] was used. Details of their procedure and its implementation into the silylation model will not be presented here.

5.3 Polymer Material Response

As is typical for constitutive laws involving inelastic deformation with an evolving microstructure, the equations for the material point stress and state variables form a coupled system and must be solved simultaneously. To do this, both Equations (42) and (47) are discretized in time and coupled using Equation (43) for the plastic strain rate.

5.3.1 Coupled Newton-Raphson Algorithm

A *trial* stress state is computed by assuming that the strain step is entirely elastic. Using (37) and (38)

$$\sigma'^{trial} = \sigma'_n + \mathcal{C}^\bullet : [\mathbf{D}' - \mathbf{D}^p - \{\alpha\dot{\Theta} + \dot{\Phi}\}\mathbf{I}]\Delta t \tag{89}$$

and

$$\sigma'_{n+1} = \sigma'^{trial} - \dot{\gamma}^p \mathcal{C}^\bullet : \mathbf{N}\Delta t \tag{90}$$

Use of the associative flow rule allows (90) to be reduced to an equation for the stress magnitude alone in terms of the as yet unknown plastic strain increment

$$\tau_{n+1} \equiv |\sigma'_{n+1}| = |\sigma'^{trial}| - 2\mu\dot{\gamma}^p\Delta t \tag{91}$$

In order to satisfy the consistency condition for yielding at the end of the time increment, from (43)

$$\dot{\gamma}^p = \dot{\gamma}_o \exp\left[\frac{-As_{n+1}}{\Theta}\left\{1 - \left(\frac{\tau_{n+1}}{s_{n+1}}\right)^{\frac{p}{q}}\right\}\right] \tag{92}$$

Finally, the strain softening state variable evolution depends upon the plastic strain increment

$$s_{n+1} = s_n + h\{1 - \frac{s_{n+1}}{s_{ss}}\}\dot{\gamma}^p\Delta t \tag{93}$$

Now Equations (91) and (93), coupled through the plastic strain rate magnitude, are formed into residuals which must ultimately vanish. This is accomplished using a Newton-Raphson iteration scheme which, after some manipulation, results in the matrix equation

$$\left\{ \begin{array}{c} G^{(k)} \\ H^{(k)} \end{array} \right\} + \left[\begin{array}{cc} A^{(k)} & B^{(k)} \\ C^{(k)} & D^{(k)} \end{array} \right] \left\{ \begin{array}{c} \Delta\tau_{n+1}^{(k)} \\ \Delta s_{n+1}^{(k)} \end{array} \right\} = \left\{ \begin{array}{c} 0 \\ 0 \end{array} \right\} \tag{94}$$

where

$$A^{(k)} = 1 + \frac{2p}{q}\frac{A\mu}{\Theta}\Delta t \left\{ \frac{s_{n+1}^{(k)}}{\tau_{n+1}^{(k)}} \right\}^{\frac{p-q}{q}} f_{n+1}^{(k)} \tag{95}$$

$$B^{(k)} = \frac{-2A\mu}{\Theta}\Delta t \left[1 - \left\{ \frac{\tau_{n+1}^{(k)}}{s_{n+1}^{(k)}} \right\}^{\frac{p}{q}} + \frac{p}{q}\frac{\tau_{n+1}^{(k)}}{s_{n+1}^{(k)}} \left(\frac{s_{n+1}^{(k)}}{\tau_{n+1}^{(k)}} \right)^{\frac{p-q}{q}} \right] f_{n+1}^{(k)} \tag{96}$$

$$C^{(k)} = \frac{-p}{q}\frac{hA}{\Theta}\Delta t \left\{ \frac{s_{n+1}^{(k)}}{\tau_{n+1}^{(k)}} \right\}^{\frac{p-q}{q}} \left[1 - \frac{s_{n+1}^{(k)}}{s_{ss}} \right] f_{n+1}^{(k)} \tag{97}$$

$$\begin{aligned} D^{(k)} &= 1 + \frac{h}{s_{ss}}\Delta t f_{n+1}^{(k)} + \frac{hA}{\Theta}\Delta t \left\{ 1 - \frac{s_{n+1}^{(k)}}{s_{ss}} \right\} \\ &\quad \left[1 - \left\{ \frac{\tau_{n+1}^{(k)}}{s_{n+1}^{(k)}} \right\}^{\frac{p}{q}} + \frac{p}{q}\frac{\tau_{n+1}^{(k)}}{s_{n+1}^{(k)}} \left(\frac{s_{n+1}^{(k)}}{\tau_{n+1}^{(k)}} \right)^{\frac{p-q}{q}} \right] f_{n+1}^{(k)} \end{aligned} \tag{98}$$

are the components of the Jacobian matrix and

$$f_{n+1}^{(k)} = \dot{\gamma}_o \exp\left[\frac{-As_{n+1}^{(k)}}{\Theta} \left\{ 1 - \left(\frac{\tau_{n+1}^{(k)}}{s_{n+1}^{(k)}} \right)^{\frac{p}{q}} \right\} \right] \tag{99}$$

is the plastic strain rate iterate. Equation (94) is solved iteratively for the increments in stress, flow resistance and plastic strain.

5.3.2 Radial Return Algorithm

While the Newton-Raphson algorithm is generally very fast, it can exhibit difficulties when the local Jacobian vanishes. For strain softening polymers, this can happen during the elastic-plastic transition where the local material stiffness tends to zero. At the expense of somewhat less accurate simplifying assumptions which vanish with decreasing time step size, a simpler radial return algorithm does not suffer this drawback. While a general radial return algorithm would necessitate iteration owing to the nonlinear constitutive law, we examine a simpler case for illustration here. For glassy polymers below the glass transition temperature, $\frac{p}{q} \to 1$ [3]. In this limit, a single iterate radial return is possible. To formulate this algorithm, however, a quasi-yield function must be defined by inverting the flow rule.

Writing (43) in terms of the stress magnitude required to produce strain rate $\dot{\gamma}^p$ for $\frac{p}{q} = 1$,

$$\tau - \left\{ s + \frac{\Theta}{A} \ln\left(\frac{\dot{\gamma}_o}{\dot{\gamma}^p} \right) \right\} = 0 \tag{100}$$

Now (100) takes on the form of a yield function

$$\mathcal{Y} = \tau - R \tag{101}$$

where the yield resistance, R, has two contributions: a part, s due to flow resistance inherent in the material structure and a rate dependent contribution

$$\beta(\Theta, \dot{\gamma}) = \frac{\Theta}{A} \ln\left\{ \frac{\dot{\gamma}_o}{\dot{\gamma}^p} \right\} \tag{102}$$

Taking an elastic strain step[4]

$$\tau^{trial} = \tau_n + 2\mu|\mathbf{D}|\Delta t \tag{103}$$

$$s^{trial} = s_n - h\frac{s_n}{s_{ss}}|\mathbf{D}|\Delta t \tag{104}$$

The yield condition (101) is then checked. If $\mathcal{Y} \leq 0$, the step is elastic and the solution

$$\tau_{n+1} = \tau^{trial} \tag{105}$$

$$s_{n+1} = s_n \tag{106}$$

---

[3] For the representative polymer PMMA, for instance, the ratio $\frac{p}{q} = \frac{5}{6}$.

[4] It has been shown [32] that, for large inelastic strain problems of this type, it is a good approximation to replace $\dot{\gamma}^p$ with $|\mathbf{D}|$ in the yield condition and the state variable recovery terms.

is accepted. If $\mathcal{Y} > 0$, then the consistency condition $\dot{\mathcal{Y}} = 0$ must be enforced in order for the stress solution to remain on the inverted yield surface. This results in an expression for the appropriate plastic strain increment

$$\Delta\gamma^p = \dot{\gamma}^p \Delta t = \frac{\tau^{trial} - s^{trial} - \beta}{2\mu + h} \tag{107}$$

which is then used to update the stress and the flow strength

$$\tau_{n+1} = \tau^{trial} - 2\mu\Delta\gamma^p \tag{108}$$

$$s_{n+1} = s_n + h\Delta\gamma^p \tag{109}$$

5.4 Time Integration

Solving for the dependent variables in the silylation model is accomplished by integrating first order differential equations in time. The general form for each of these equations is

$$\frac{d\Phi}{dt} = RHS. \tag{110}$$

where Φ represents Gauss point stress or nodal velocity, mass, or unconstrained volumetric expansion rate. The shorthand notation "*RHS*" is used to indicate the right hand side of the equation which in general is a function of other dependent variables.

A simple "upwind" difference in time is used to approximate the time derivative, *i.e.*,

$$\frac{\Phi^{n+1} - \Phi^{n}}{\Delta t} = RHS. \tag{111}$$

where $n+1$ refers to the value at the new time step and n the previous time step. Whether the integration is explicit or implicit depends, of course, on how RHS is evaluated. If it is evaluated at $n+1$, then the integration is implicit and a nonlinear algebra problem must be solved. If it is evaluated at n, as in the present model, the integration is explicit, resulting in the following simple expression for Φ^{n+1},

$$\Phi^{n+1} = \Phi^{n} + (\Delta t) RHS^{n} \tag{112}$$

Explicit integrations are conditionally stable which requires careful selection of the time step Δt. The Courant stability limits for the mass transport (diffusion) and mechanical calculations are functions of element geometry (shape and size) and the properties of the material. For quadrilateral elements it can be shown that

$$\Delta t_d = \frac{A^2}{\mathcal{D}B} \tag{113}$$

$$\Delta t_m = \sqrt{\frac{\rho A^2}{(\lambda + 2\mu)B}} \tag{114}$$

where Δt_d and Δt_m are the stable diffusion and mechanical time steps, respectively. In the above equations $\mathcal{D}$ is the diffusion coefficient, λ and μ are Lamé elastic constants, A is the element area (given by Equation (79)) and B is an element geometric parameter given by,

$$B = \frac{(y_2 - y_4)^2 + (y_1 - y_3)^2 + (x_1 - x_3)^2 + (x_2 - x_4)^2}{2}. \tag{115}$$

Generally Δt_d is orders of magnitude larger than Δt_m. Hence, the time step is controlled by the mechanical part of the problem. In quasi-static mechanical calculations such as this one, an arbitrary scaling of the mechanical density can be used to bring the stable mechanical time step more in line with the stable diffusion time step. Hence for the purpose of computing material momentum, the density can be increased by some arbitrary scaling factor, f_d, where $f_d \gg 1$. The effect of this density scaling is to add artificial inertia to the momentum equation. Care must be taken to insure that density scaling does not compromise the quasi-static behavior of the momentum equation. When this occurs, the solution exhibits obvious nonphysical behavior. In order to avoid excessively long computational times, some measure of mechanical density scaling was used for all silylation calculations presented in Section 6.

5.5 Mesh Generation and Post Processing

A Fortran 77 computer program was written to solve the 2D silylation equations presented here. The program reads a keyword driven problem description file using the parsing language developed by Perano and Kaliakin (see *e.g.* [45, 46]) and generates a two-dimensional computational mesh using the Sandia developed mesh generator AP [47]. During the solution phase a series of time-state files are written, typically one time-state file for each second of simulated time. Post processing of these time state files is also performed using AP. This relatively mature pre and post processing interface makes it possible to set up, solve and post process a wide variety of 2D silyation problems quickly and accurately.

6 Results

Calculations made using the previously described models are presented in this section. The first two subsections deal with model verification for simple geometries including transient behavior at a single point and transient behavoir in one spacial dimension. The remaining subsection discusses the fully coupled transient behavior of the silylation model (2D Model) in two spacial dimensions.

6.1 Constitutive Model Material Point Simulations

The polymer constitutive model consists of the coupled system of Equations (42), (43), and (47). They are parametrized by a set of material constants $\{\mu, \lambda, \dot{\gamma}_o, s_o, s_{ss}, A, h, p, q\}$. These parameters are generally either derived from other physical quantities whose values are known for a class of materials (*e.g.* see Equation (44) for A) or fit to experimental data. A complete set of parameters have been fit for the amorphous polymer, polymethylmethacrylate (PMMA) elsewhere [30]. These are used here to illustrate features of the model behavior for a material point under three distinct homogeneous deformation paths. We exercise the model for constant strain rate uniaxial extension to show that it recreates the intermediate strain tensile data. We then use the model to simulate one-dimensional free surface swelling characteristic of the behavior of the silylating layer far from the substrate edge. Lastly, we artificially restrict the model to elastic deformations only to illustrate the effect of non-volume conserving flow on the degree of free surface swelling. For all the discussions which follow, the material properties correspond to a constant temperature of $\Theta = 90\ °C < \Theta_g$ and are given by

$$\mu = 1 \times 10^{10}\ \frac{\text{dyne}}{\text{cm}^2} \tag{116}$$

$$\lambda = 3.33 \times 10^{9}\ \frac{\text{dyne}}{\text{cm}^2} \tag{117}$$

$$\dot{\gamma}_o = 1.0 \times 10^{11}\ \text{s}^{-1} \tag{118}$$

$$s_o = 8.8 \times 10^{8}\ \frac{\text{dyne}}{\text{cm}^2} \tag{119}$$

$$s_{ss} = 7.7 \times 10^{8}\ \frac{\text{dyne}}{\text{cm}^2} \tag{120}$$

$$A = 1.7 \times 10^{-5} \ \frac{\mathrm{K-cm^2}}{\mathrm{dyne}} \tag{121}$$

$$h = 9 \times 10^{9} \ \frac{\mathrm{dyne}}{\mathrm{cm^2}} \tag{122}$$

$$p = q = 1 \tag{123}$$

6.1.1 Uniaxial Extension

The viscous inelastic softening response prior to polymer locking behavior can be parameterized entirely by scalar state variables in the model. These can be estimated by fitting the model to uniaxial deformation paths. Here, we adopt the set of material parameters in [30] listed above. These have been chosen, for illustrative purposes, to reproduce the uniaxial tensile data for PMMA [30]. The response of PMMA pulled in uniaxial extension at a rate of unity is shown in Figure 12 along with the response reported by Boyce et al. [30]. Only the softening portion of the response is included in the model presented here. Further, the rate-dependent yield and post-yield softening response are functions of the applied deformation rate magnitude $|D|$, the hardening modulus h, and the steady state inelastic flow strength s_{ss}. The mechanical response depends on these model parameters as illustrated in Figures 13, 14, and 15 respectively. A similarly isolated integration of the model equations is compared in Figure 16 with its implementation in the two-dimensional finite element code.

6.1.2 Free Surface Swelling

Because we interface the material model with a displacement-based finite element code, the constitutive subroutine is generally driven by a strain history discretized in time. This is straightforward when kinematic or Dirichlet boundary conditions are imposed on the finite element mesh. When Neumann, flux or stress boundary conditions are imposed, iteration is generally necessary in order to converge on the appropriate strain step necessary to satisfy this boundary condition. This is the case for the one-dimensional silylation experiment described in Appendix A where the free surface of the silylating layer is traction-free. In order to test the constitutive algorithm for this case, an iterative loop was added which imposed a stress free boundary condition in one-dimension. To do this, an elastic strain step is presumed for the out-of-plane swelling response:

$$\Delta\epsilon_{22} = D_{22}\Delta t = \frac{\lambda + \frac{2}{3}\mu}{\lambda + 2\mu}\Delta\Phi \tag{124}$$

This strain step is applied, resulting in a non-zero normal component of the stress at the layer surface. The strain step is iteratively adjusted until the normal stress component vanishes. At each increment, the corresponding compressive in-plane layer stresses accompanying the induced silylation swelling are given by

$$\Delta\sigma_{11} = \Delta\sigma_{33} = -2\mu\Delta\epsilon_{22} \tag{125}$$

The deviatoric resultant in-plane compressive stress associated with a constant rate of swelling, $\dot{\Phi}$, is shown in Figure 17. Note that the response is similar qualitatively to the kinematically driven response described in the previous Section. After yielding, the polymer inelastic flow strength evolves in accordance with Equation (47). This state variable evolution is depicted in Figure 18 for one-dimensional free surface swelling.

6.1.3 Idealized Elastic Swelling

As a final case study, we restrict the mechanical constitutive model to purely elastic behavior. For this example, the free surface expansion can be computed in closed form as a means of verifying the numerical implementation. Such a case will only be physically plausible for very small deformations. To simulate this behavior, however, the yield strength, s_o, can be artificially increased to ensure that no plasticity occurs. For this limiting case, the incremental relations (124) and (125) can be replaced by total quantities and the free surface strain will be given by

$$\epsilon_{22} = \frac{\lambda + \frac{2}{3}\mu}{\lambda + 2\mu}\Phi = \frac{1+\nu}{3(1-\nu)}\Phi \tag{126}$$

and the accompanying lateral compressive stresses in the silylation layer are

$$\sigma_{11} = \sigma_{33} = -2\mu\epsilon_{22} = \frac{-E}{3(1-\nu)}\Phi \tag{127}$$

both in agreement with the one-dimensional model presented in Appendix A. The dependence of free surface swelling on Poisson's ratio is shown in Figure 19. For swellings to large strain, the fully elastic-plastic free surface motion is closely approximated by the elastic limit as $\nu \to \frac{1}{2}$. The isolated model integration is shown in this limit in Figure 20 along with the two-dimensional finite element model implementation.

6.2 Comparison of 1D and 2D Model Results

A simple one-dimensional transient problem was formulated for the purpose of comparing the 1-D model discussed in Appendix A and the more general 2D silylation model. It is assumed that a layer of unsilylated and uncrosslinked resist 1×10^{-5} cm thick is applied to a perfectly rigid surface. The resist and the surface it is attached to are infinite in the plane orthogonal to the thickness direction. At t=0 a fixed concentration of the silylation agent is imposed on the free surface of the resist. As time proceeds the agent diffuses into the resist from the free surface and reacts with the resist, causing silicon deposition and swelling of the entire resist layer. Material parameters and boundary conditions are selected such that an unstressed layer would double in thickness when the layer becomes fully silylated.

Figure 21 illustrates the mesh and application of boundary conditions for the transient 1-D problem. A single row of 100 elements was used in the 2D simulation. (Correspondingly, 100 grid points were used in the model described in Appendix A). The lower two nodes of the bottom element (at $z = L(t)$) are fixed to the rigid surface and no mass transfer is permitted across the element face. Symmetry boundary conditions are imposed on the right and left boundaries of the element row to simulate the "infinite layer". Constant values for the concentrations of species A and E are imposed on the free surface. The coordinate z shown in the figure is the nondimensional distance (*i.e.*, actual distance divided by current length $L(t)$) from the free end.

It should be noted that the model of Appendix A does not account for the presence of a silylation reaction product species B. Furthermore, the constitutive model used in Appendix A relating stress to strain is a simple elastic model and therefore not realistic for real silylation problems undergoing large strains. Nevertheless, the model is useful for verifying coupled momentum/diffusion behavior in 1D.

Dimensional parameters used in the 2D model are related to the dimensionless parameters of the 1D model according to the following:

$$\tau = \frac{k_s \rho_{A_s}}{M_A}\, t \tag{128}$$

$$\hat{P} = \frac{\rho_A}{\rho_{A_s}} \tag{129}$$

$$\hat{Q} = \frac{\rho_C}{\tilde{\rho}_C} \tag{130}$$

$$\hat{U} = \frac{\rho_D}{\tilde{\rho}_C}\frac{M_C}{M_D} \tag{131}$$

$$\hat{E} = \frac{\rho_E}{\tilde{\rho}_C}\frac{M_C}{M_E} \tag{132}$$

$$\alpha = \frac{M_E}{\tilde{\rho}_E}\frac{\tilde{\rho}_D}{M_D} = 2.0 \tag{133}$$

$$\gamma = \frac{\tilde{\rho}_C}{M_C}\frac{M_A}{\rho_{A_s}} = 1.0 \tag{134}$$

$$\tau_r = \frac{k_s \rho_{A_s}}{M_A} {k_e}^{-1} = 1.0 \tag{135}$$

$$\beta = \frac{w c_o}{\alpha} = 0 \tag{136}$$

where,

$$c_o = \frac{\tilde{\rho}_C}{M_C} = 0.0113207 \text{ mol/cm}^3 \tag{137}$$

Note that if the silylation reaction rate does not depend on stress, then $b = 0$ in Equation (180) and $k_1 = k_o = k_s$. Also note that the diffusion coefficient, D, in Appendix A is equal to $\mathcal{D}_o$ in Equations (21) and (22).

In Equations (128) through (136), τ is dimensionless time, and $\hat{P}, \hat{Q}, \hat{U}$, and $\hat{E}$ are dimensionless dependent variables. The remaining dimensionless parameters depend on material properties and boundary conditions and remain constant throughout the calculation. The dimensional properties used in the 2D calculation were determined from the constants specified in Equations (128) through (136) and can be summarized as follows:

$$\rho_A = 39.62 \text{ g/cm}^3 \tag{138}$$

$$\rho_C = 1.2 \text{ g/cm}^3 \tag{139}$$

$$\rho_D = 2.6717 \text{ g/cm}^3 \tag{140}$$

$$\rho_E = 1.3359 \text{ g/cm}^3 \tag{141}$$

$$M_A = 175 \text{ g/mol} \tag{142}$$

$$M_C = 106 \text{ g/mol} \tag{143}$$

$$M_D = 236 \text{ g/mol} \tag{144}$$

$$M_E = 236 \text{ g/mol} \tag{145}$$

$$\rho_{A_s} = 19810 \text{ g/cm}^3 \tag{146}$$

$$k_s = 175 \text{ cm}^3/(\text{mol} - \text{s}) \tag{147}$$

$$\mathcal{D}_o = 2 \times 10^{-12} \text{ cm}^2/\text{s} \tag{148}$$

$$L_o = 1 \times 10^{-5} \text{ cm} \tag{149}$$

$$k_e = 1.981 \text{ s}^{-1} \tag{150}$$

Comparisons of predictions from the 1D and 2D models are shown in Figures 22 and 23. Figure 22 shows the growth of the silylation layer as a function of time for two different Poisson ratios, $\nu = 0.3$ and $\nu = 0.5$. It can be shown that the final layer thicknesses corresponding to $\nu = .3$ and $\nu = .5$ are 1.62×10^{-5} cm and 2.00×10^{-5} cm respectively. The latter value follows from the observation that all elastic deformation for the case where $\nu = .5$ must be volume conserving. In each case, the 2D model correctly predicts the final layer thickness. The 1D model of Appendix A predicts slightly lower values of layer thickness than the 2D model throughout the transient. These differences tend to disappear when more grid points are used in the 1D model. The dashed blue line shown in Figure 22 illustrates the effect of including plasticity in the material response. The 2D model prediction of the layer thickness for $\nu = .3$ shows that when plasticity is included, the growth of the silylation layer is nearly volume conserving. This is the case because only a small portion of the total deformation is elastic. The volume-preserving plastic deformation comprises a substantially larger percentage of the total deformation.

Figure 23 compares 1D and 2D model predictions for mass concentrations and stress distributions at three different times during "elastic" silylation with $\nu = .5$. Figure 23 (a) shows the mass concentration of the silylation agent at $2.5, 10$, and 60 seconds. Results are plotted using the nondimensional length $z(t)$. Similar comparisons for the mass concentration of unsilylated resist and silylated resist are shown in (b) and (c). In each case the comparisons are excellent. The lateral stress distributions (σ_{xx} and σ_{zz}) are compared in Figure 23 (d). Each model predicts a final compressive lateral stress of 1.05×10^{10} dynes/cm^2. Transient stress distributions also compare favorably, although the 2D model predicts a small compressive stress through the layer thickness during the propagation of the silylation front.

6.3 Transient 2D Silylation - Nominal Calculation

In this subsection the results of a 2D transient silylation simulation will be presented. The objective is to simulate the material behavior observed during a process similar to that shown in Figure 2. Figure 24 shows the computational mesh for the nominal 2D silylation problem. A resist 4×10^{-5} cm in thickness is bonded to a rigid surface (fixed surface). Part of the free surface has been crosslinked to a depth of 6×10^{-6} cm. The planes of symmetry shown in Figure 24 are used to simulate a series of silylation lines parallel to the z axis. The distance between any two adjacent silylation centerlines is 4.8×10^{-5} cm. In this simulation, crosslinked behavior is modeled by reducing the diffusivity,$\mathcal{D}_o$, of the silylation agent in crosslinked elements by three orders of magnitude relative to the uncrosslinked elements. Except for the diffusion coefficient, all other crosslinked and uncrosslinked material properties are assumed to be identical. These properties are summarized as follows:

$$E = 2.25 \times 10^{10} \text{ dyne/cm}^2 \tag{151}$$

$$\nu = .125 \tag{152}$$

$$s_0 = 8.8 \times 10^8 \text{ dyne/cm}^2 \tag{153}$$

$$h = 9.0 \times 10^9 \text{ dyne/cm}^2 \tag{154}$$

$$A = 1.7 \times 10^{-5} \text{ K} - \text{cm}^2/\text{dyne} \tag{155}$$

$$s_{ss} = 7.7 \times 10^8 \text{ dyne/cm}^2 \tag{156}$$

$$\alpha = 0.0 \tag{157}$$

$$\dot{\gamma}_0 = 1.0 \times 10^{11} \text{ s}^{-1} \tag{158}$$

$$M_A = 175. \text{ g/mol} \tag{159}$$

$$M_B = 45.\ \text{g/mol} \tag{160}$$

$$M_C = 106.\ \text{g/mol} \tag{161}$$

$$M_D = 236.\ \text{g/mol} \tag{162}$$

$$M_E = 236.\ \text{g/mol} \tag{163}$$

$$\rho_A = 39.62\ \text{g/cm}^3 \tag{164}$$

$$\rho_B = 100.0\ \text{g/cm}^3 \tag{165}$$

$$\rho_C = 1.2\ \text{g/cm}^3 \tag{166}$$

$$\rho_D = 1.2\ \text{g/cm}^3 \tag{167}$$

$$\rho_E = 1.2\ \text{g/cm}^3 \tag{168}$$

$$k_e = 2.0\ \text{s}^{-1} \tag{169}$$

$$k_s = 175\ \text{cm}^3/(\text{mol} - \text{s}) \tag{170}$$

$$w = 0\ \text{cm}^3/\text{mol} \tag{171}$$

$$\text{Crosslinked } \mathcal{D}_\text{o} = 2.0 \times 10^{-15}\ \text{cm}^2/\text{s} \tag{172}$$

$$\text{Uncrosslinked } \mathcal{D}_\text{o} = 2.0 \times 10^{-12}\ \text{cm}^2/\text{s} \tag{173}$$

Initially the resist is assumed to be unsilylated; *i.e.*, it is composed entirely of species C. At time zero the free surface is exposed to the silylation agent, species A, and mass transport, chemistry, and material swelling proceed for a simulated time of 60 seconds.

Boundary conditions for mass transfer may be summarized as follows:

At the free surface: $\epsilon_A = .05, \epsilon_E = .95$

At the right symmetry boundary: No mass transfer

At the left symmetry boundary: No mass transfer

At the bottom fixed boundary: No mass transfer

Boundary conditions for momentum may be summarized as follows:

At the free surface: Stress free, see Equation (28).

At the right symmetry boundary: $\dot{u} = 0$

At the left symmetry boundary: $\dot{u} = 0$

At the bottom fixed boundary: $\dot{u} = \dot{v} = 0$

Figure 25 shows cross-sections of silylation agent (species A) concentration and material swelling for time states corresponding to 0, 1, 3, 5, 10, 30 and 60 seconds. To aid in visualization, results have been mirrored across the left symmetry boundary which corresponds to the y axis and the centerline of a typical silylation cross-section. At t=0 seconds, the resist is unsilylated except for the imposed concentration of A at the free surface. As early as t=1 second, evidence of species A diffusion, silylation reaction, and the onset of material swelling is clearly visible in the uncrosslinked region. As time proceeds the silylation agent continues to diffuse preferentially into the uncrosslinked resist causing a localized material swelling similar to that observed in Figure 2. In this particular simulation, the effect of crosslinking was modeled using a reduced diffusion coefficient for the crosslinked material. As a result, mass transport, chemistry and material swelling in the crosslinked region were localized to a very thin layer along the free surface. This layer is most visible at t=60 seconds and resembles the so-called "scum" layer observed over crosslinked regions after silylation experiments.

Figure 26 shows concentration profiles of the silylation reaction product (species B), the unsilylated solid (species C), the unexpanded silylated solid (species D) and the expanded silylated solid (species E) at the end of the simulation (t=60 seconds). As expected the highest concentration of the silylation reaction product (species B) occurs above the reaction front. The contour plot of unsilylated solid (species C) clearly shows the depletion of species C above the reaction front. The blue core representing low concentrations of C shows that the reaction front is beginning to move under the crosslinked portion of the resist. Because of the relatively short relaxation time for the conversion of species D to E ($k_e = 2.0$ s^{-1}), significant amounts of D are confined to a relatively narrow band (shown in green in the D concentration plot) near the reaction front. The portions of the resist which have completed the conversion to the expanded silylated solid are clearly visible as a yellow band in the concentration plot for species E.

Stresses developed during the silylation process ultimately determine the amount of swelling and the final shape of the material. Figure 27 shows cross-sectional contours of stress at 60 seconds. Included are contours for the through-thickness stress, σ_{yy}, the lateral stress, σ_{xx}, and the shear stress, σ_{xy}. Note that the individual in-plane deviatoric stress component, σ'_{xx}, reaches values beyond the rate-dependent yield strength. This indicates that substantial inelastic flow can occur at swelling rates typically seen in the silylation process. We point out for clarification that this is true if the polymer plastic properties are reasonably represented by those for PMMA. When there is substantial inelastic flow, volume conservation dictates that the amount of swelling will be only marginally affected by the stress response. The stresses and kinematic constraints, *i.e.* the geometry of the crosslinked region, however, can play a substantial role in the overall shape change of the material.

The relationship between crosslinked and uncrosslinked regions at the conclusion of the simulation is shown in

Figure 28. Elements of the crosslinked polymer are distinguished solely by their reduced diffusion coefficient relative to the uncrosslinked material. Elements in the crosslinked region are shown in blue and elements in the uncrosslinked region are shown in red. The original shapes of these regions prior to silylation are shown in Figure 24. As expected, nearly all material swelling has been confined to the uncrosslinked region. Some swelling is evident in the crosslinked area along the free surface (the "scum layer") and in the interior interface between the crosslinked and uncrosslinked regions. This was to be expected since, in this modeling scenario, the crosslinked region was assigned a finite (but low) diffusion coefficient and the silylation reaction was permitted to proceed unimpeded when the silylation agent was present. Here, the crosslinked polymer has been assigned the same constitutive parameters as the uncrosslinked polymer. Figure 28 shows that in this case, silylation extends to the material below the crosslinked region. The resulting swelling causes substantial upward movement of the crosslinked material. The simulation suggests that such movement is likely to occur whenever crosslinking is sufficiently shallow and silylation times are long. It may be expected, however, that these response features would be sensitive to changes in the inelastic mechanical properties of the crosslinked region. For future reference, it may prove worthwhile to implement the locking Langevin spring element in the large strain model (this may represent crosslinked behavior as described in Section 4.3.5) or perform a parameter study over a range of stiffer effective elastic moduli for the crosslinked polymer.

7 Concluding Remarks

This report documents the development of a new two-dimensional transient finite element model of the positive tone silylation process. The 2D model focuses on the part of the process in which crosslinked and uncrosslinked resist is exposed to a diffusing silylation agent. The model accounts for the combined effects of mass transport (silylation agent and reaction product), the chemical reaction leading to the uptake of silicon and material swelling, the generation of stresses, and the resulting material motion. Both Fickian and Case II diffusion models are incorporated. The model provides for the appropriate mass transport and momentum boundary conditions and couples the behavior of uncrosslinked and crosslinked materials as well as the compliance of any underlying device topology.

The 2D model behavior has been verified using independent material point simulations and a one-dimensional transient finite difference model. Finite element mesh generation, problem setup, and post processing of computed results is sufficiently mature to permit the 2D model to be used in the investigation of a broad parameter space which includes material properties and geometry issues (*e.g.*, alternate crosslinking distributions, resist thickness, etc.).

The authors recommend that future work in the area of silylation modeling be directed toward exercising the present model over a range of parameter space to determine which properties and phenomena have the largest affects on the silylation process. In addition, studies should be undertaken to determine relevant material properties. In order for the model to become a predictive design tool, it is recommended that it be verified against a set of well controlled silylation experiments.

A APPENDIX - A One-Dimensional Model

A logical first step in simulating a process such as silylation is to develop a one-dimensional model. This can be used to obtain a basic understanding of at least some aspects of the process with a minimum of computational effort, and it can also serve as a validation tool for multidimensional codes that will eventually be used to describe the process in detail. The model to be presented here is similar to that developed by Zuniga and Neureuther [19], but there are some differences in implementation. In particular, the bulk (convective) flow arising from the volume change of the solid is now accounted for explicitly in the species conservation equations, and simple analytical relations for the amount of swelling and the induced stresses are derived. However, since the stress-strain relations are based on the linearized equations of elasticity, the model is strictly valid only for small deformations.

If it is assumed that the gas phase is well mixed and nonreacting, then the modeling effort can be confined to the solid. According to Zuniga and Neureuther, there are four chemical species of interest: the (dissolved) silylating agent P, the unreacted hydroxyl group Q, the silylated but unexpanded group U, and the expanded group E. In what follows, the latter three species will be assumed to include the associated part of the polymer chain, so that all of the solid material is accounted for. Clearly, only species P is free to diffuse, and it can react with Q according to

$$\mathrm{P} + \mathrm{Q} \xrightarrow{k_1} \mathrm{U} + \ldots$$

Here k_1 is a second-order rate constant, provided that mass-action kinetics is appropriate. While there may be mobile reaction products in addition to the fixed group U, they will not be important as long as their volumes are negligible and the reaction is irreversible. In any case, the newly formed U is eventually converted to E with a characteristic relaxation time t_r:

$$\mathrm{U} \xrightarrow{t_r} \mathrm{E}$$

The primary task is to determine the time-dependent concentration profiles for the four species and, of particular interest, the total amount of swelling as a function of time.

The differential equations governing the process can be obtained by applying the general material balance [48] to each species. In molar units and in one dimension,

$$\frac{\partial c_i}{\partial t} + v\frac{\partial c_i}{\partial x} = -c_i\frac{\partial v}{\partial x} - \frac{\partial J_i}{\partial x} + R_i \tag{174}$$

where t is time, x is the spatial coordinate (measured perpendicular to the gas-solid interface), v is the mass-average velocity, c_i is the molar concentration of species i, J_i is its diffusion flux, and R_i is its volumetric production rate by chemical reactions. Letting $c_{\mathrm{P}} \equiv P$, and so forth, one has

$$\frac{\partial P}{\partial t} + v\frac{\partial P}{\partial x} = -P\frac{\partial v}{\partial x} - \frac{\partial J_{\mathrm{P}}}{\partial x} - k_1 PQ \tag{175}$$

$$\frac{\partial E}{\partial t} + v\frac{\partial E}{\partial x} = -E\frac{\partial v}{\partial x} + \frac{U}{t_r} \tag{176}$$

$$\frac{\partial Q}{\partial t} + v\frac{\partial Q}{\partial x} = -Q\frac{\partial v}{\partial x} - k_1 PQ \tag{177}$$

$$\frac{\partial U}{\partial t} + v\frac{\partial U}{\partial x} = -U\frac{\partial v}{\partial x} + k_1 PQ - \frac{U}{t_r} \tag{178}$$

Following Zuniga and Neureuther, we approximate the diffusion flux by

$$J_{\mathrm{P}} = -D\, e^{wE}\, \frac{\partial P}{\partial x} \tag{179}$$

where w is a parameter that allows the diffusivity of species P to vary with the extent of swelling; D is simply the diffusivity in the initial state. In addition, at fixed temperature the rate constant k_1 is assumed to vary with the local stress σ according to

$$k_1 = k_0\, e^{b\sigma} \tag{180}$$

Equation (175) then becomes

$$\frac{\partial P}{\partial t} + v\frac{\partial P}{\partial x} = -P\frac{\partial v}{\partial x} + D\,\frac{\partial}{\partial x}\left(e^{wE}\,\frac{\partial P}{\partial x}\right) - k_0\, e^{b\sigma} PQ \tag{181}$$

and there are similar modifications to Equations (177) and (178).

Since there are now four differential equations but six unknowns (P, E, Q, U, v, and σ), two additional equations are needed. These can be obtained by relating the stress level and the overall molar concentration of the fixed species to the extent of the swelling reaction. The first step is to introduce a parameter α, which is the ratio of the molar volumes of species E and U in a completely unconstrained system; it is assumed that the molar volumes of Q and U are identical. Then, in the absence of stresses, the fractional increase in volume at any point (neglecting the effect of the dissolved gas P) is

$$\Phi = \frac{E(\alpha - 1)}{Q + U + E} \tag{182}$$

The quantity Φ plays the same role as a thermal expansion in the equations of statics. For the one-dimensional system being considered here, there is no stress in the x-direction, while there are no strains in y and z. The equations of equilibrium [49] then show that the axial strain is

$$\epsilon_x = \Phi\frac{1+\nu}{3(1-\nu)} \tag{183}$$

and the transverse compressive stress is

$$\sigma_y = \sigma_z \equiv \sigma = -\Phi\frac{Y}{3(1-\nu)} \tag{184}$$

where Y is Young's modulus and ν is Poisson's ratio. From Equations (182) and (183) it can be shown that the molar concentrations of the fixed solid species are related by

$$Q + U + E\alpha + E(\alpha - 1)\frac{2(2\nu - 1)}{3(1 - \nu)} = c_0 \tag{185}$$

where c_0 is the initial molar concentration of Q. For the special case $\nu = \frac{1}{2}$ this reduces to

$$Q + U + E\alpha = c_0 \tag{186}$$

which is identical to the result that would be obtained for a completely unconstrained system.

Now, the initial conditions to be used with the differential equations are

$$Q = c_0\,, \quad P = E = U = 0\,, \quad \text{and} \quad v = 0 \quad \text{at} \quad t = 0 \tag{187}$$

Likewise, if the gas-solid interface is defined to be the position $x = 0$, then two boundary conditions are

$$P = P_s \quad \text{and} \quad v = 0 \quad \text{at} \quad x = 0 \tag{188}$$

Here P_s is assumed to be given by the solubility of the gaseous silylating agent in the solid, i.e., equilibrium prevails across the interface. Analysis of the first-order partial differential equations (176)–(178) shows that all of the associated characteristic base curves originate on the line $t = 0$ in the t–x plane; therefore, the initial conditions on E, Q, and U are sufficient to determine these functions without any boundary conditions being specified. However, a second boundary condition is needed for P. If the thickness of the silylation layer is denoted by L, and if the solid substrate at $x > L$ is impermeable to the diffusing species P, then an appropriate condition is

$$\frac{\partial P}{\partial x} = 0 \quad \text{at} \quad x = L \tag{189}$$

Finally, because the swelling reaction causes the silylation layer to thicken over time, L varies and must be determined as a function of t by means of the kinematic condition

$$\frac{dL}{dt} = v(L, t) \tag{190}$$

together with the initial condition

$$L = L_0 \quad \text{at} \quad t = 0 \tag{191}$$

The set of governing equations and auxiliary conditions is now complete. However, in order to assist in dealing with the moving boundary at $x = L(t)$, it is convenient to introduce the new spatial variable $z = x/L(t)$, so that the problem is now defined over the interval $0 \leq z \leq 1$. With this transformation, Equation (181) becomes

$$\frac{\partial P}{\partial t} + \frac{1}{L}\frac{\partial P}{\partial z}\left(v - z\frac{dL}{dt}\right) = -\frac{P}{L}\frac{\partial v}{\partial z} + \frac{D}{L^2}\frac{\partial}{\partial z}\left(e^{wE}\frac{\partial P}{\partial z}\right) - k_0\, e^{b\sigma} PQ \tag{192}$$

and similar results are obtained from Equations (176)–(178).

It can be seen that the mathematical model involves eleven different parameters, namely D, w, k_0, b, t_r, α, c_0, ν, Y, P_s, and L_0. In order to reduce this number somewhat and to make the solutions more general, one can write the system in dimensionless form using the following variables:

$$\tau = k_0 P_s t\,, \quad \hat{P} = \frac{P}{P_s}\,, \quad \hat{Q} = \frac{Q}{c_0}\,, \quad \hat{U} = \frac{U}{c_0}\,, \quad \hat{E} = \frac{E}{c_0}\,, \quad \phi = \frac{v}{k_0 P_s L_0}\,, \quad l = \frac{L}{L_0}\,, \quad \hat{\sigma} = \frac{\sigma}{Y} \tag{193}$$

The new equations need not be given here, but suffice it to say that they involve seven dimensionless parameters (as could have been anticipated from the Buckingham Pi Theorem [50]):

$$\theta = \frac{D}{L_0^2 k_0 P_s}\,, \quad \beta = \frac{w c_0}{\alpha}\,, \quad \tau_r = k_0 P_s t_r\,, \quad \alpha\,, \quad \gamma = \frac{c_0}{P_s}\,, \quad \nu\,, \quad \lambda = bY \tag{194}$$

All of the sample solutions to follow will be characterized in terms of these dimensionless groups.

The most straightforward way to solve the system is via the method of lines. The first step is to replace all spatial derivatives with finite differences; this leads to a mixture of algebraic equations and time-dependent ordinary differential equations. Upwind differencing is used in order to assure stability. The differential/algebraic system is then integrated in time using the packaged solver DASSL [51], which is ideally suited to problems of this kind.

A sample set of solutions will now be presented for an arbitrarily chosen set of parameters. The quantities β and λ are both taken as unity, so that the diffusivity of the silylating agent increases with time while the rate constant for the silylation reaction decreases. The values of the swelling factor α and Poisson's ratio ν are 2 and 0.5, respectively; these should be fairly realistic for the polymeric materials used in this process. The concentration ratio γ and the parameter τ_r, which is a ratio of characteristic times for the swelling and silylation reactions, are set equal to unity. Finally, the parameter θ, which is a ratio of characteristic times for silylation and diffusion, is assigned a value of 0.01. The relatively slow diffusion should lead to the appearance of a fairly well-defined reaction front that moves into the material as time progresses.

The results of the computations are shown in Figures 29–36. In all but the last two figures, spatial profiles are plotted for fixed moments in time separated by $\Delta\tau = 0.5$. Figure 29 shows that the concentration of P in the solid builds up only slowly, because the silylating agent cannot diffuse very far before being consumed by the relatively fast chemical reaction. This situation is alleviated only when the fixed reactant Q is consumed. Concentration profiles for the latter are shown in Figure 30, where the aforementioned reaction front is evident (although not particularly sharp). In Figure 31 one sees typical behavior for a reaction intermediate: at any position, the concentration of U initially rises as a result of the silylation reaction, but it eventually erodes as U is converted to E. Since the concentration of U is generally small even at its peak, it is not surprising that the profiles for E in Figure 32 are complementary to those for Q in Figure 30. However, it should be noted that the maximum concentration of E is 0.5 rather than 1.0, as a result of the swelling factor $\alpha = 2$.

The dimensionless velocity profiles are shown in Figure 33. To reiterate, these nonzero velocities arise entirely as a result of the swelling reaction. Since the boundary at $z = 0$ is fixed, the maximum velocity at any time must always occur at the other boundary $z = 1$ ($x = L(t)$), even if the reaction front has not yet reached that point. However, the value of the maximum velocity is a nonmonotonic function of time; this is obvious from the fact that it must start at zero and then eventually return to zero when the process is complete. For the case at hand, the velocity at $z = 1$ appears to reach a maximum at about $\tau = 2.5$.

The stress profiles in Figure 34 bear a strong resemblance to the concentration profiles for species E in Figure 32. This would be very obvious if one were to plot the absolute values of the stress; the actual values are of course negative because the stress is compressive. As noted above, this causes the rate constant for the silylation reaction to decrease with time, and this (together with the increased diffusivity of P) leads to a reaction front that is not as sharp as it would otherwise be.

Finally, Figures 35 and 36 show (as solid curves) the overall layer thickness l as a function of time. The time span in Figure 35 is the same as in Figures 29–34. Since the value of l at $\tau = 10$ is still less than 1.4, the process is obviously very far from completion ($l = 2.0$), in accordance with Figure 32. Figure 35 also gives results for a different value of Poisson's ratio, namely $\nu = 0.3$, which is appropriate to a wide variety of elastic solids. The volume increase in this case is considerably smaller; this is expected, because the compressive stresses will have a larger effect on the volume the more ν deviates from the value of 0.5 for an incompressible solid.

The behavior of $l(\tau)$ over the entire course of the process is shown in Figure 36. There are four identifiable although indistinct regimes: a short induction period (more obvious in Figure 35) due to the preliminary formation of U; a period of rapid, unconstrained expansion; a period of slower growth after the leading edge of the expansion front reaches the impermeable boundary; and a final stage of no growth after the reactions are complete. The ultimate value of l at $\tau = \infty$ can be obtained from Equation (185) by realizing that the layer thickness is inversely proportional to the total concentration of Q, U, and E at any time. This gives

$$l_\infty = 1 + \frac{(1+\nu)(\alpha - 1)}{3(1-\nu)} \tag{195}$$

For $\nu = \frac{1}{2}$ the result is simply $l_\infty = \alpha$, as expected. For $\nu = 0.3$ and $\alpha = 2$ one finds $l_\infty = 1.619$, which agrees well with the asymptotic value in Figure 36.

Many more parameter studies could be undertaken, but it should be remembered that the results are largely fictitious due to the assumption of purely (and linearly) elastic behavior. Therefore, as noted earlier, this model should be used primarily to check the functioning of the multidimensional codes.

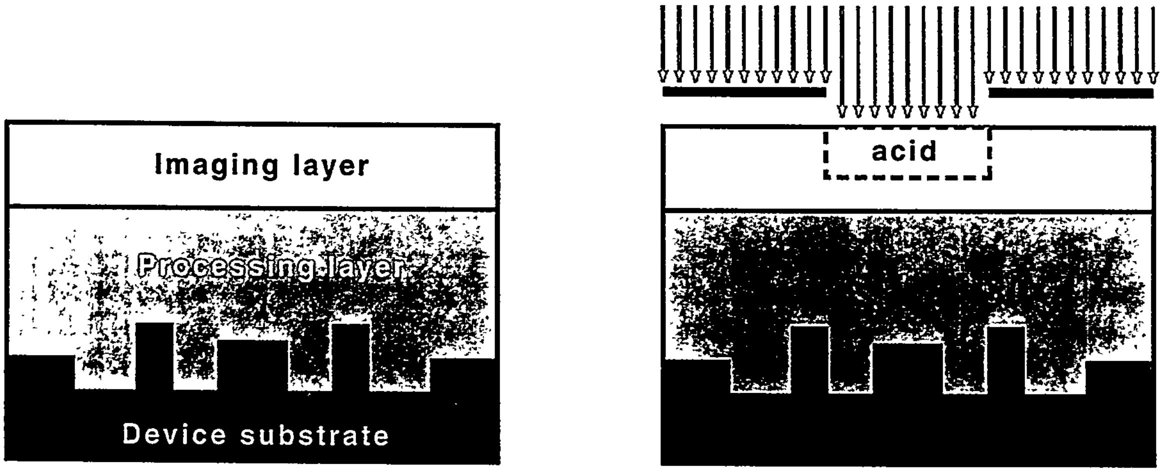

(a) Cross-section prior to TSI

(b) Exposure

(c) Post exposure bake

(d) Silylation

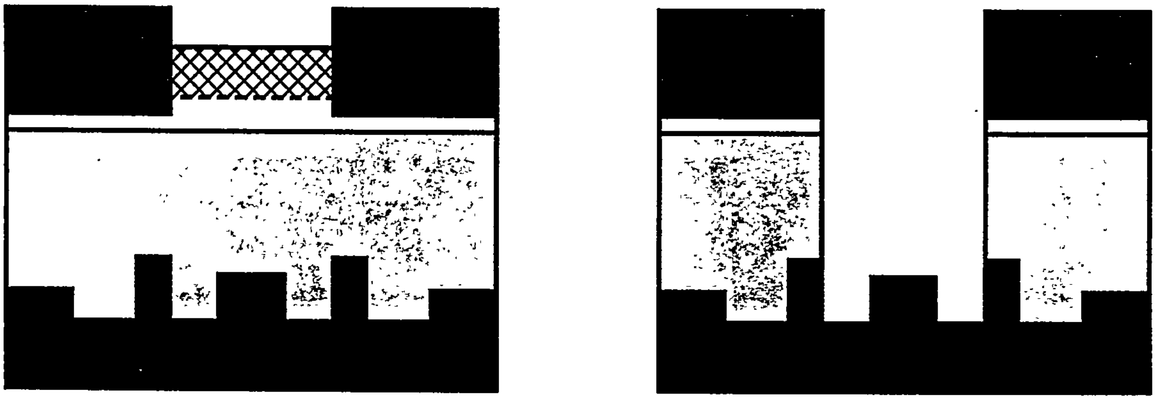

(e) Plasma descum

(f) Plasma etch

Figure 1: TSI processing steps.

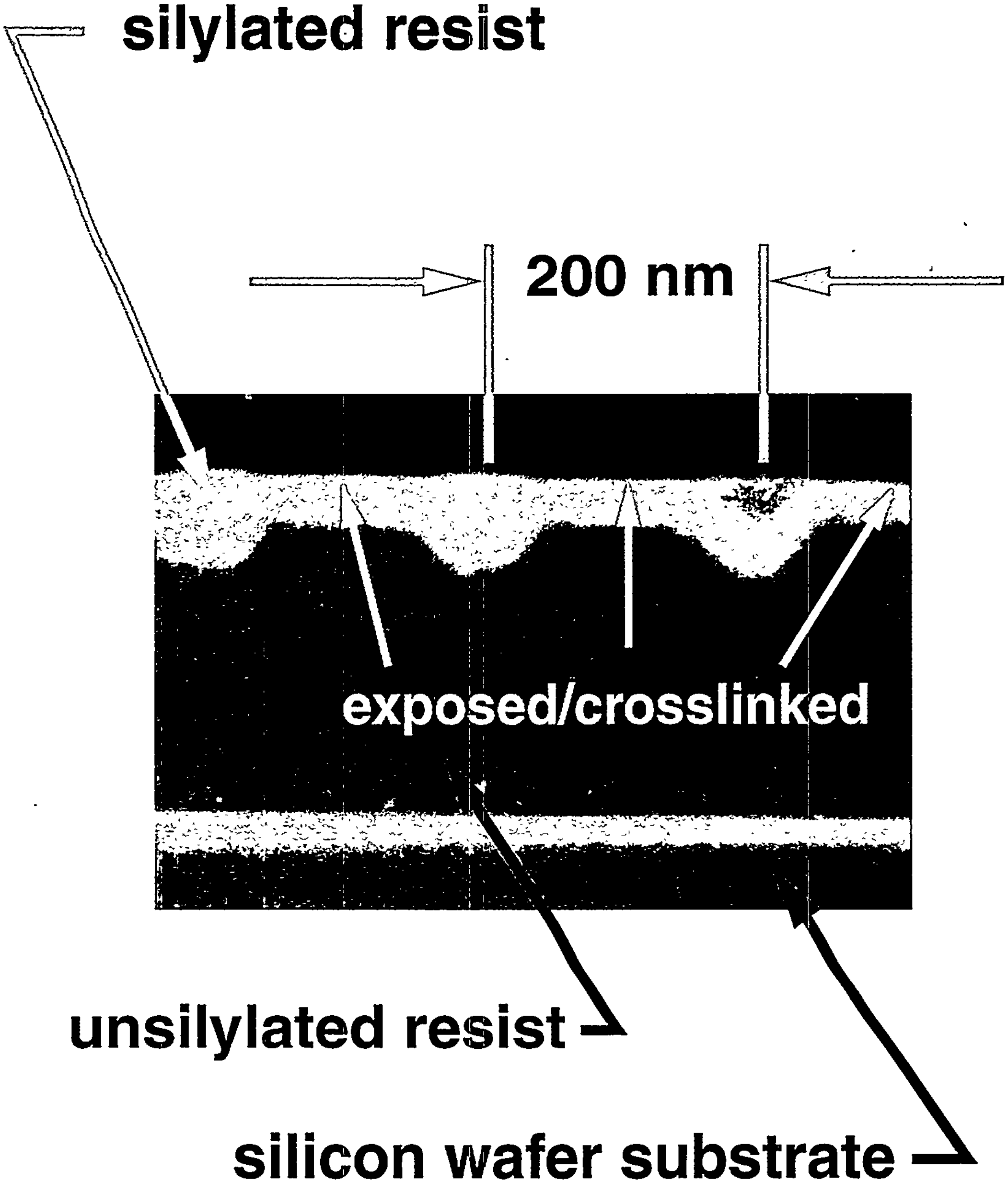

Figure 2: Cross-sectional plasma stain of silylation prior to etch.

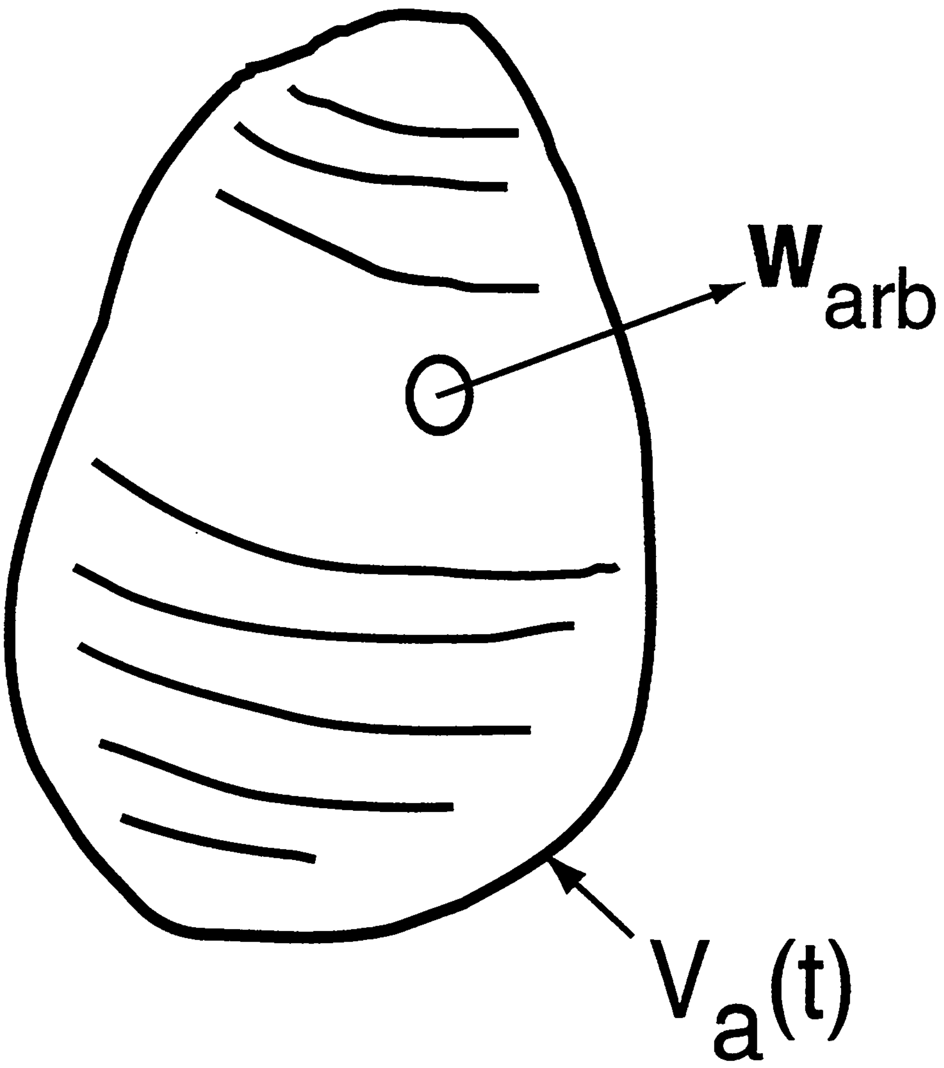

Figure 3: Arbitrary moving control volume.

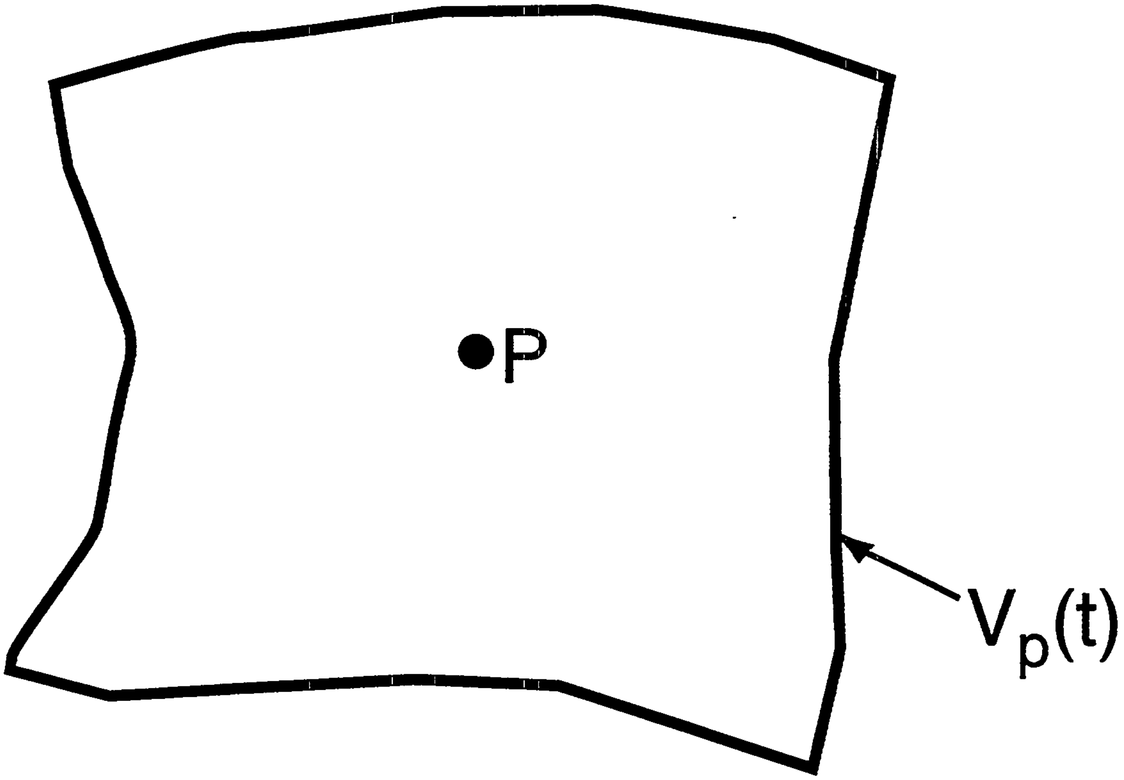

Figure 4: A two-dimensional quadrilateral control volume centered about point P.

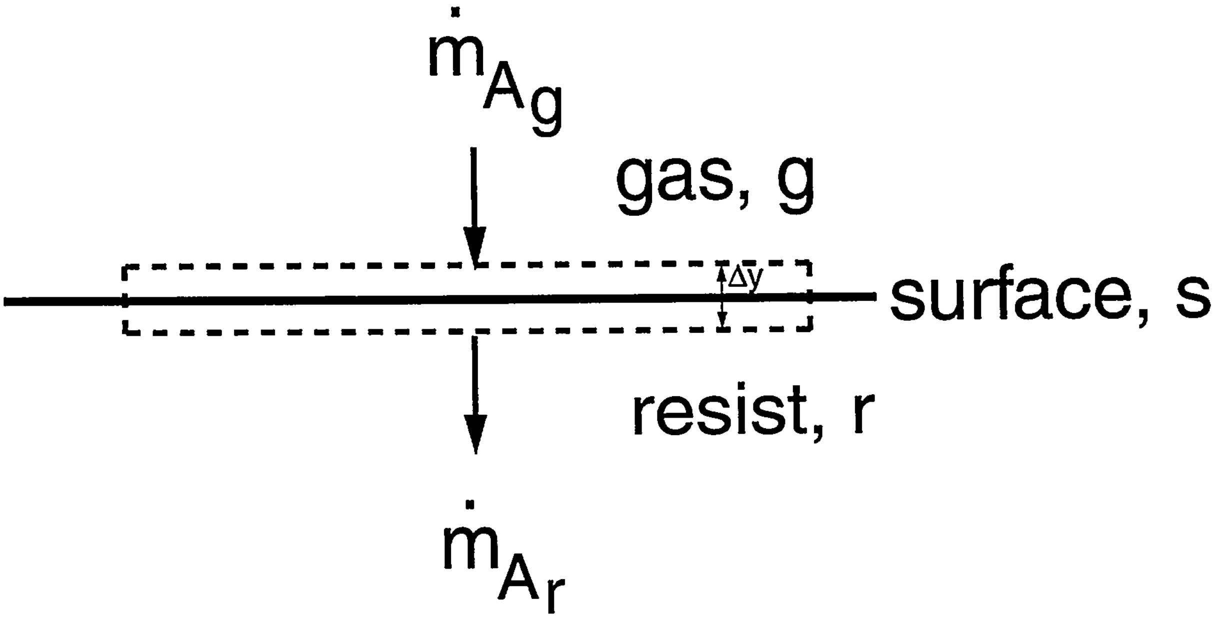

Figure 5: Control volume and fluxes at resist/gas interface.

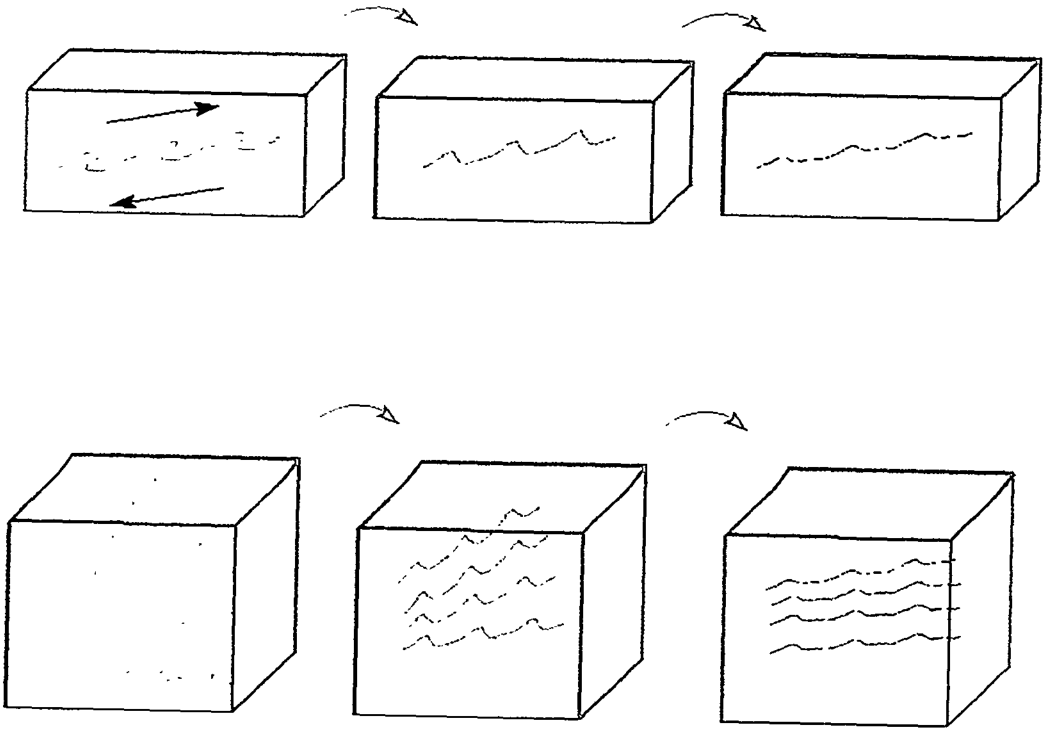

Figure 6: The Eyring dashpot element (upper figure) and the Langevin spring element (lower figure).

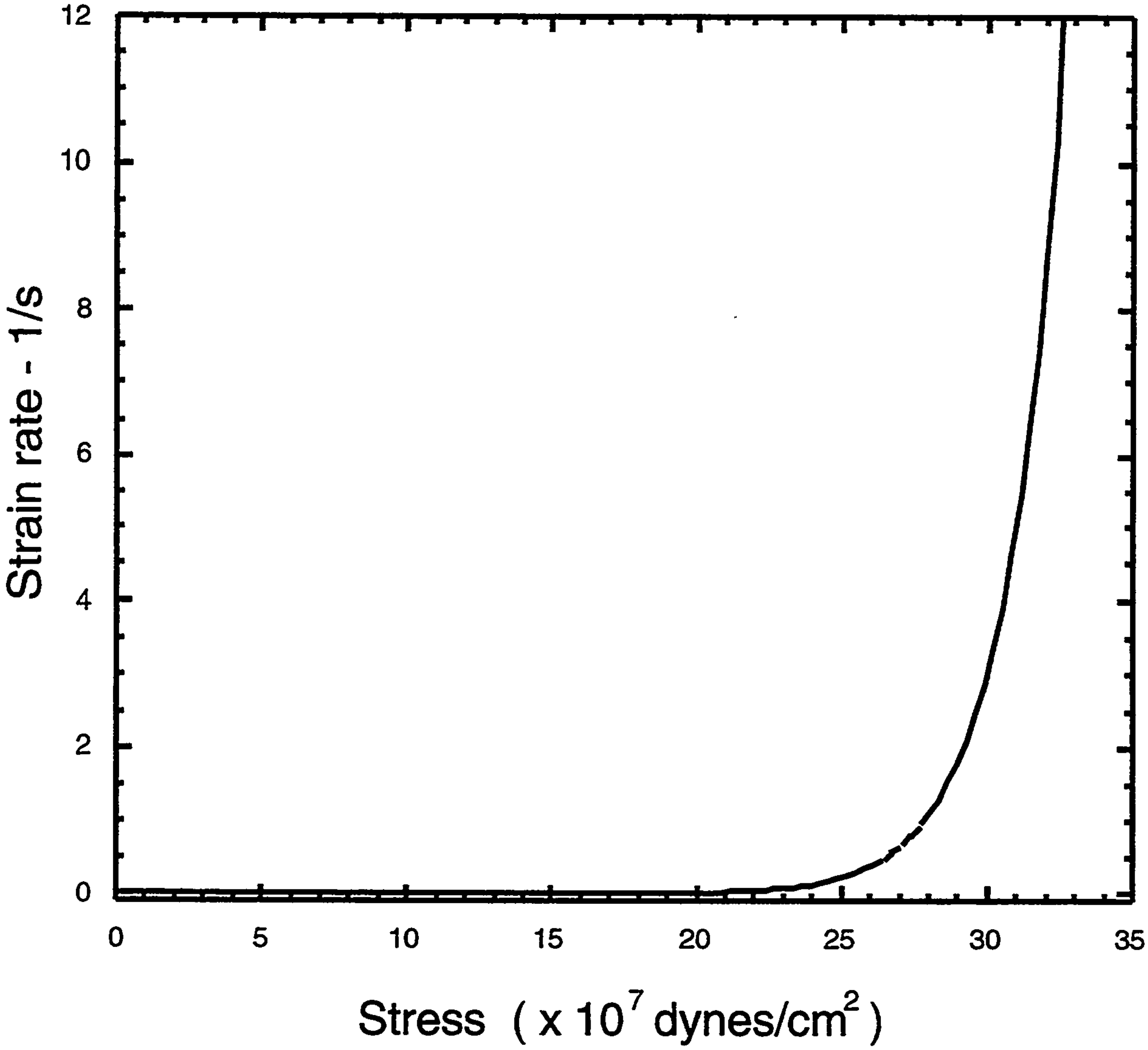

Figure 7: Dashpot response.

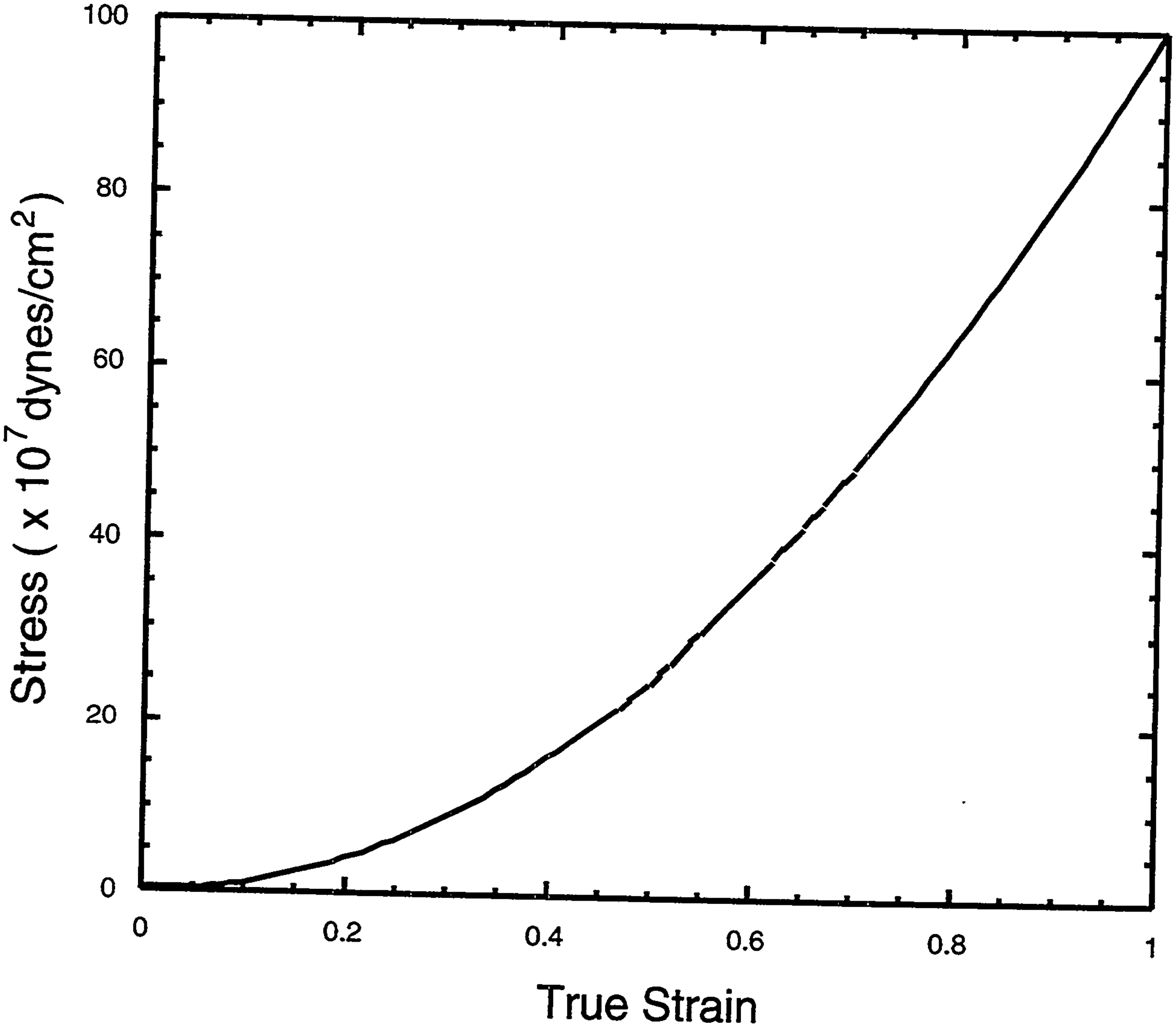

Figure 8: Langevin spring response.

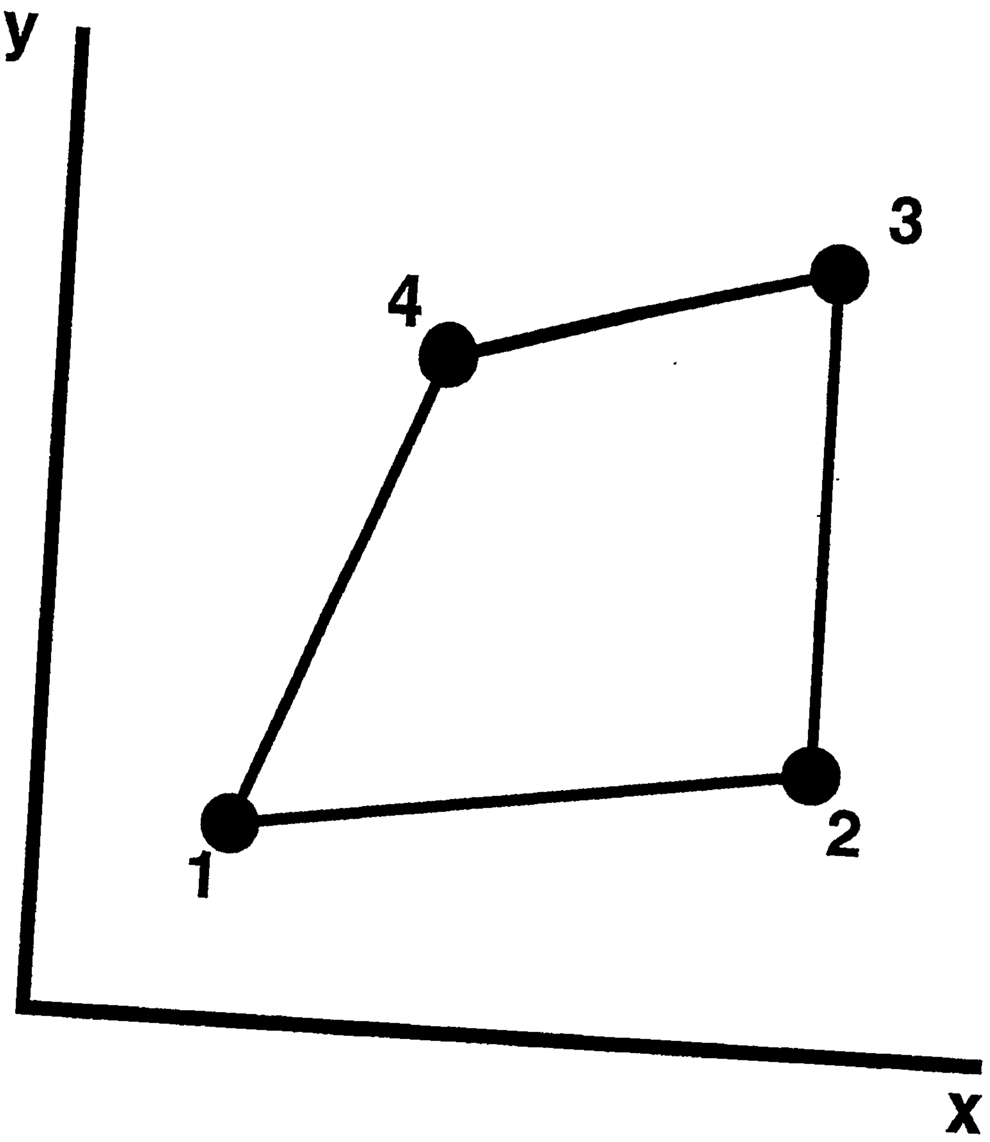

Figure 9: Four node quadrilateral element in global coordinate system.

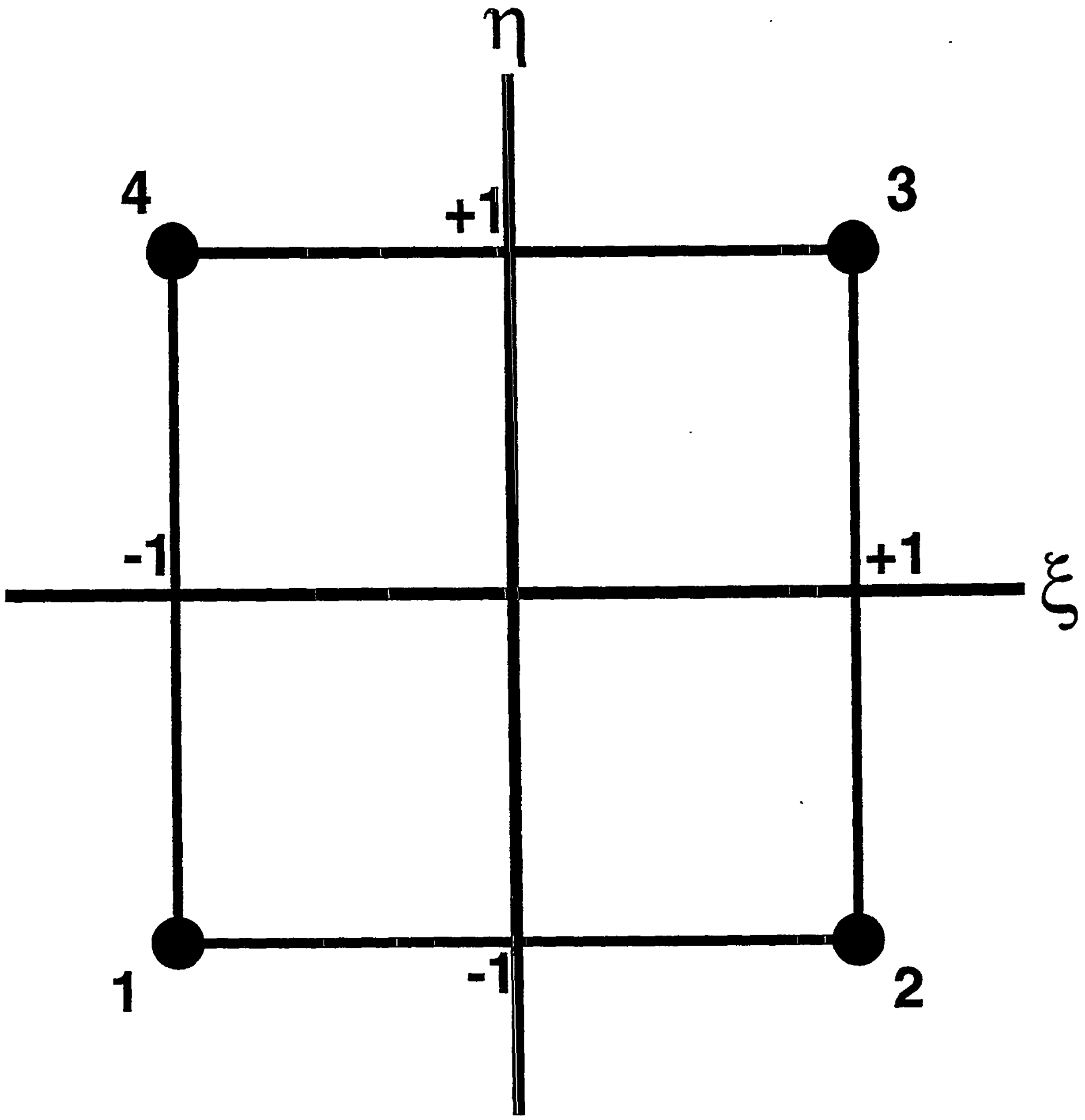

Figure 10: Four node quadrilateral element in local isoparametric coordinate system.

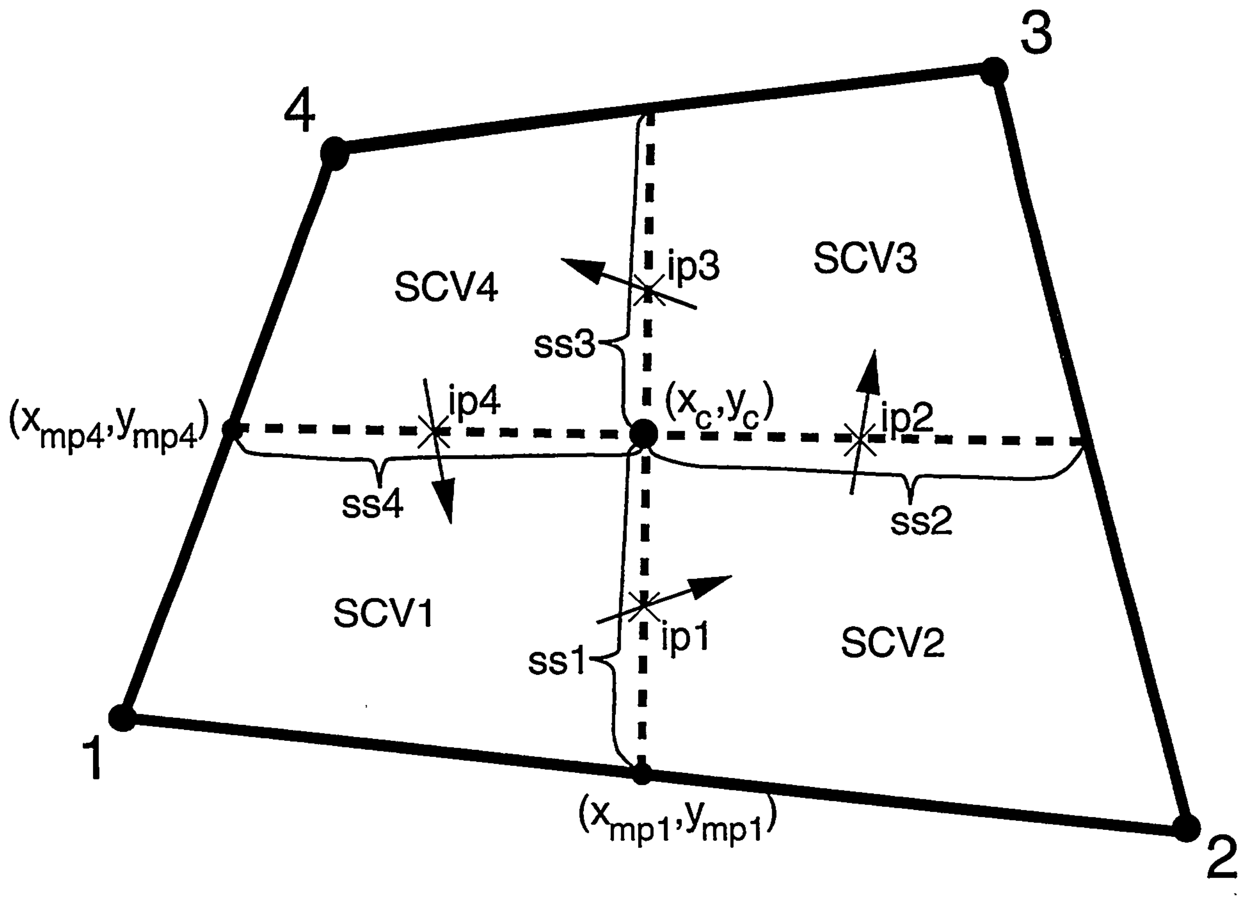

Figure 11: A four node quadrilateral element showing sub control volumes and integration points for the CVFEM.

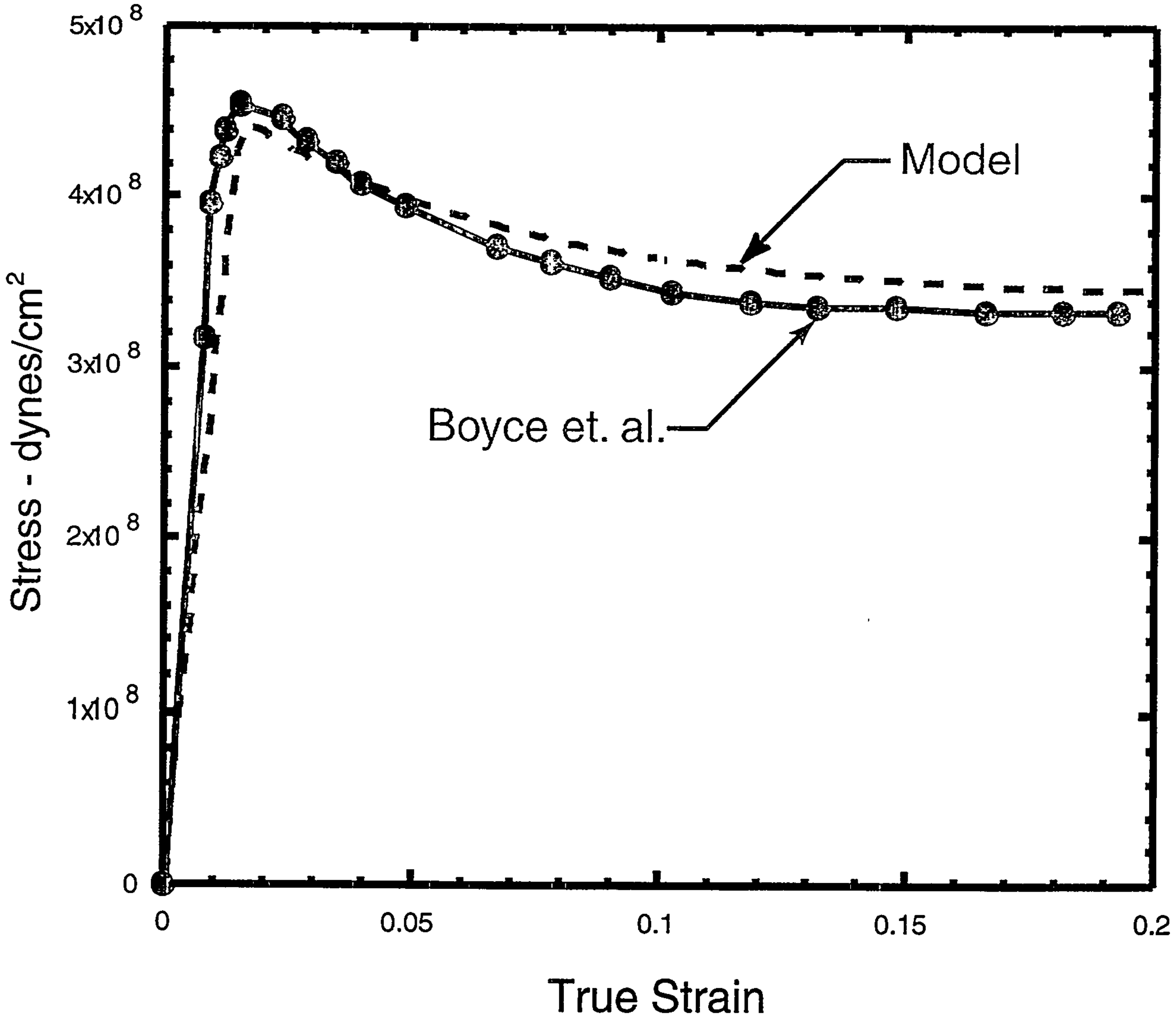

Figure 12: Response in uniaxial extension.

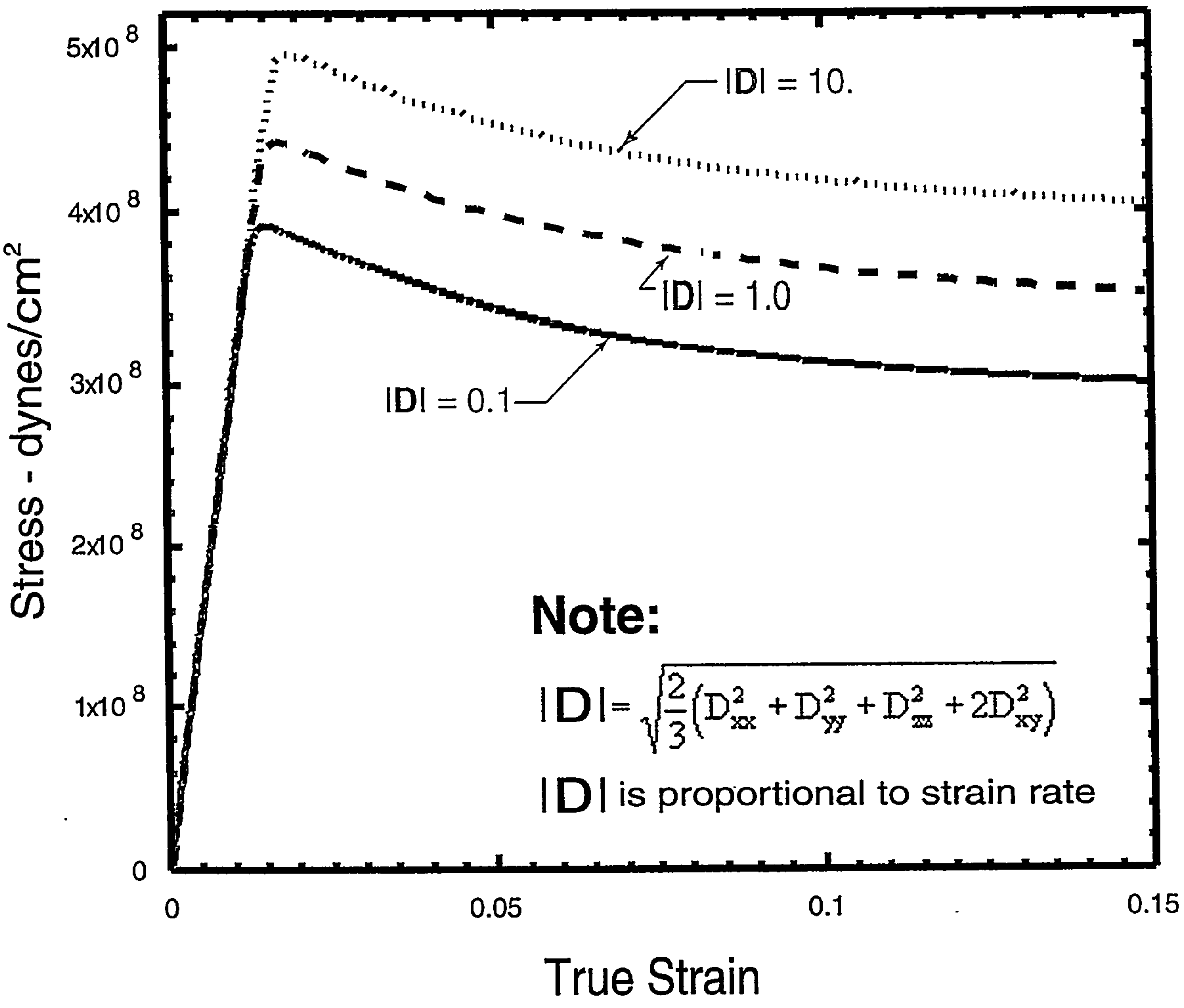

Figure 13: Rate dependence of flow strength in uniaxial extension.

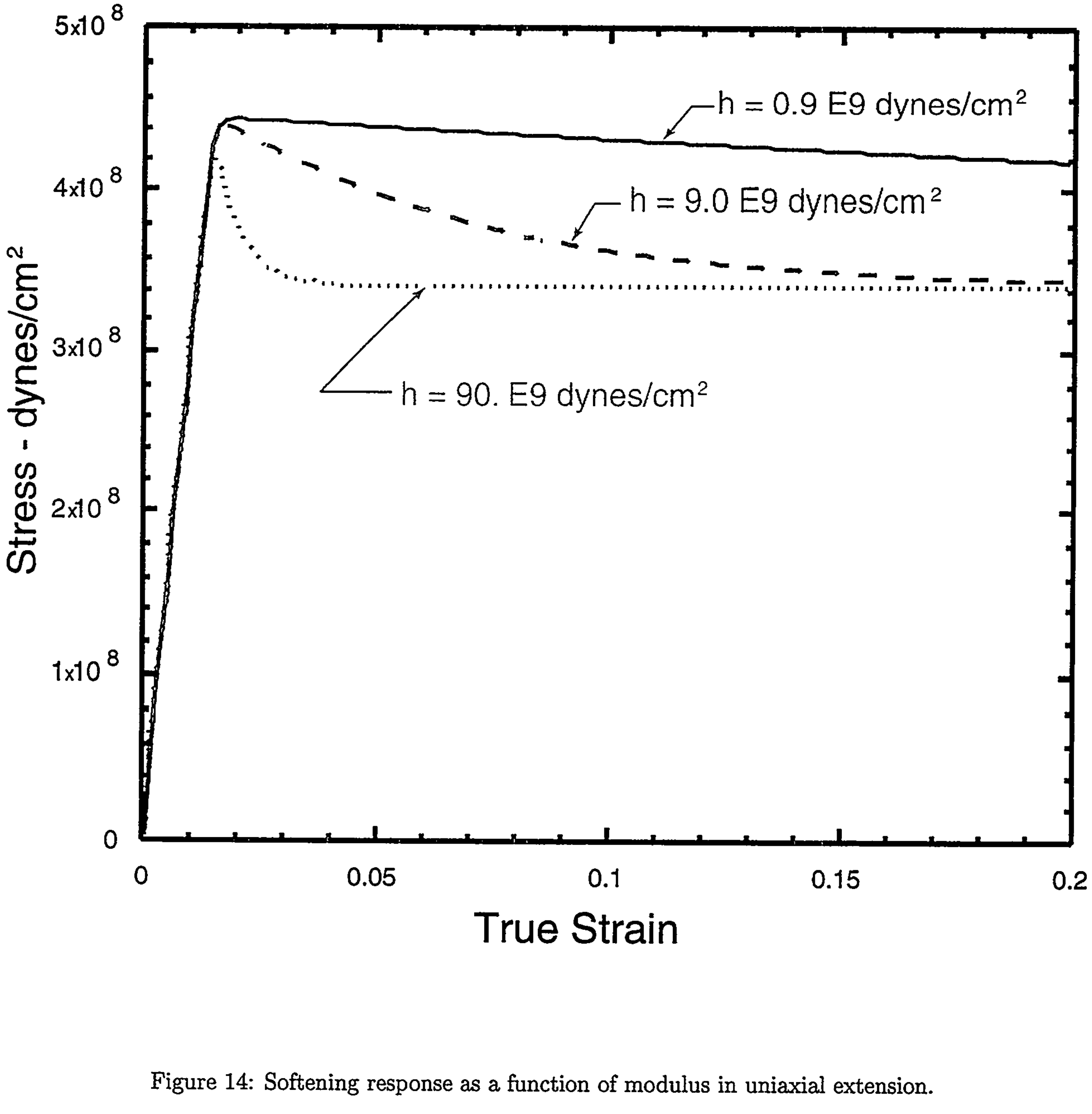

Figure 14: Softening response as a function of modulus in uniaxial extension.

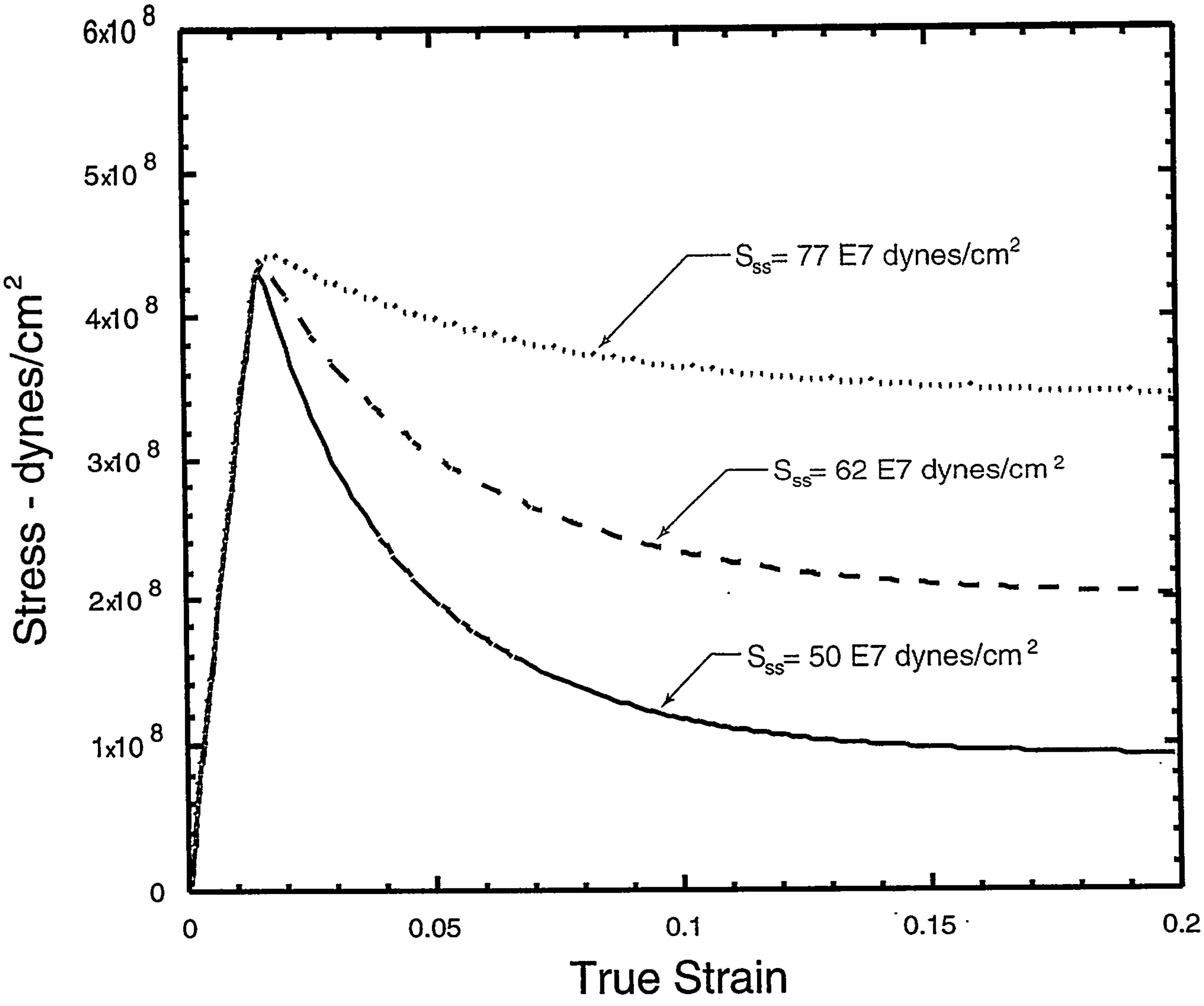

Figure 15: Steady state flow strength response in uniaxial extension.

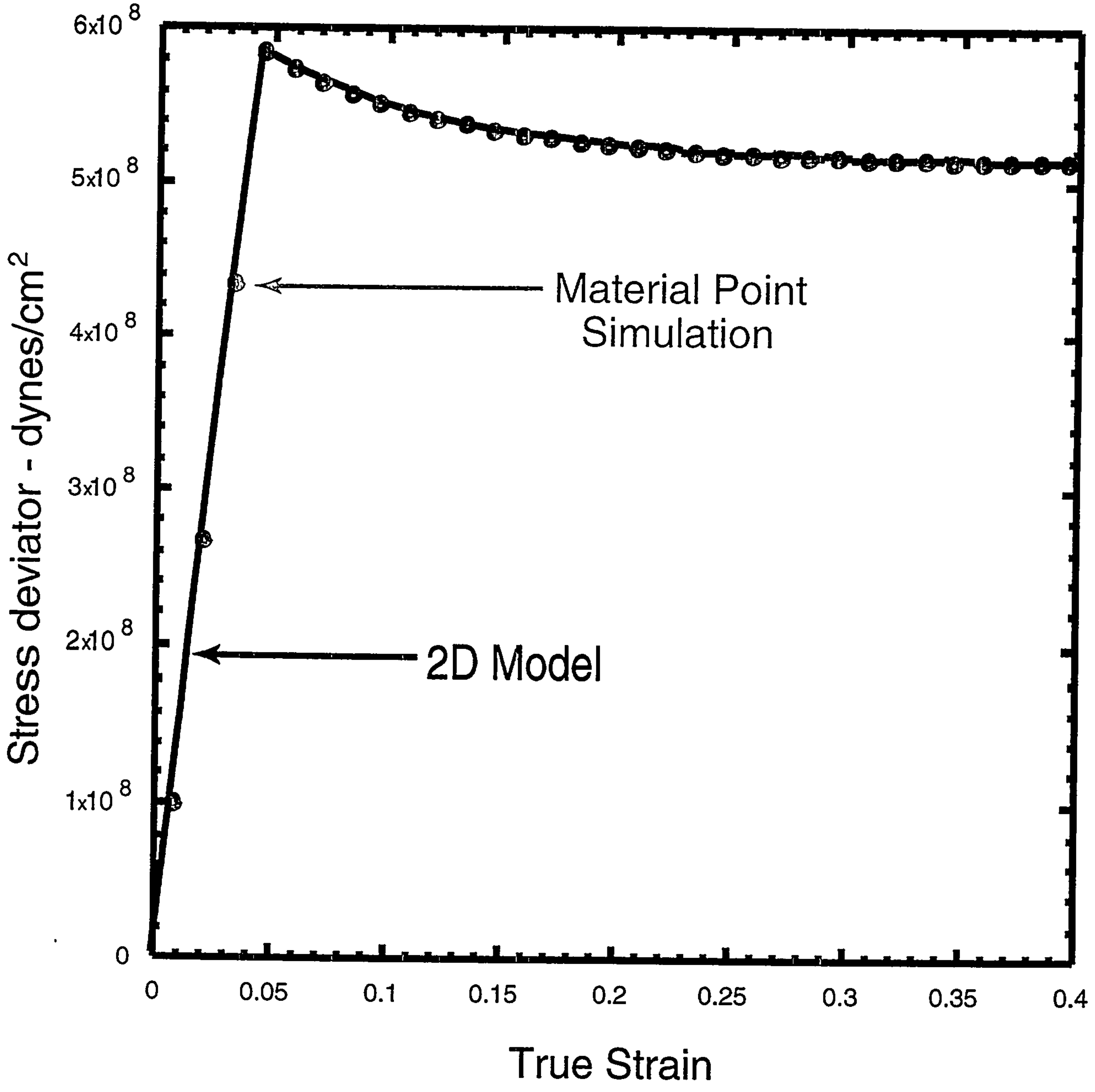

Figure 16: Large strain uniaxial extension simulation: Comparison of material point simulation and 2D model.

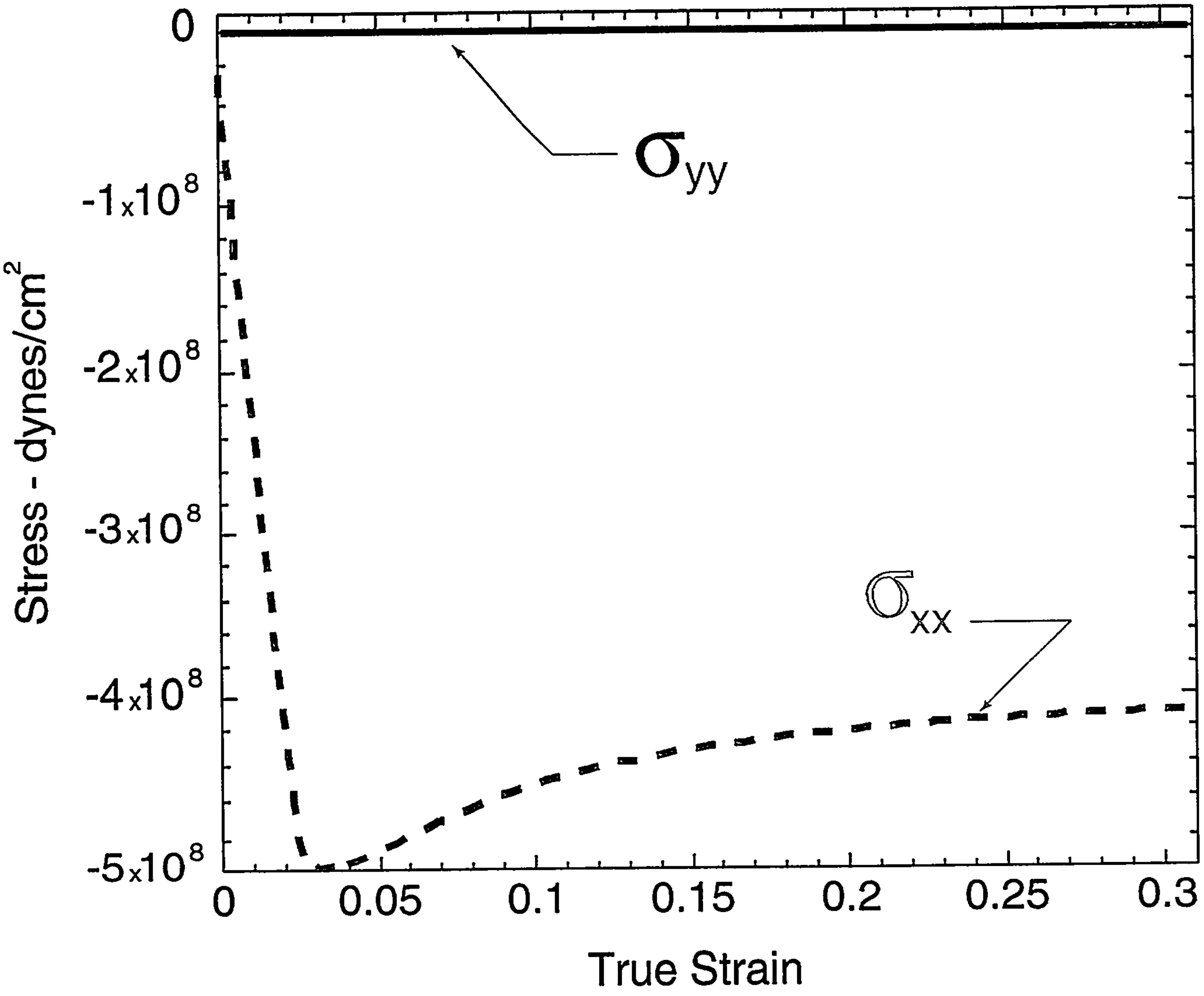

Figure 17: Response in free surface swelling.

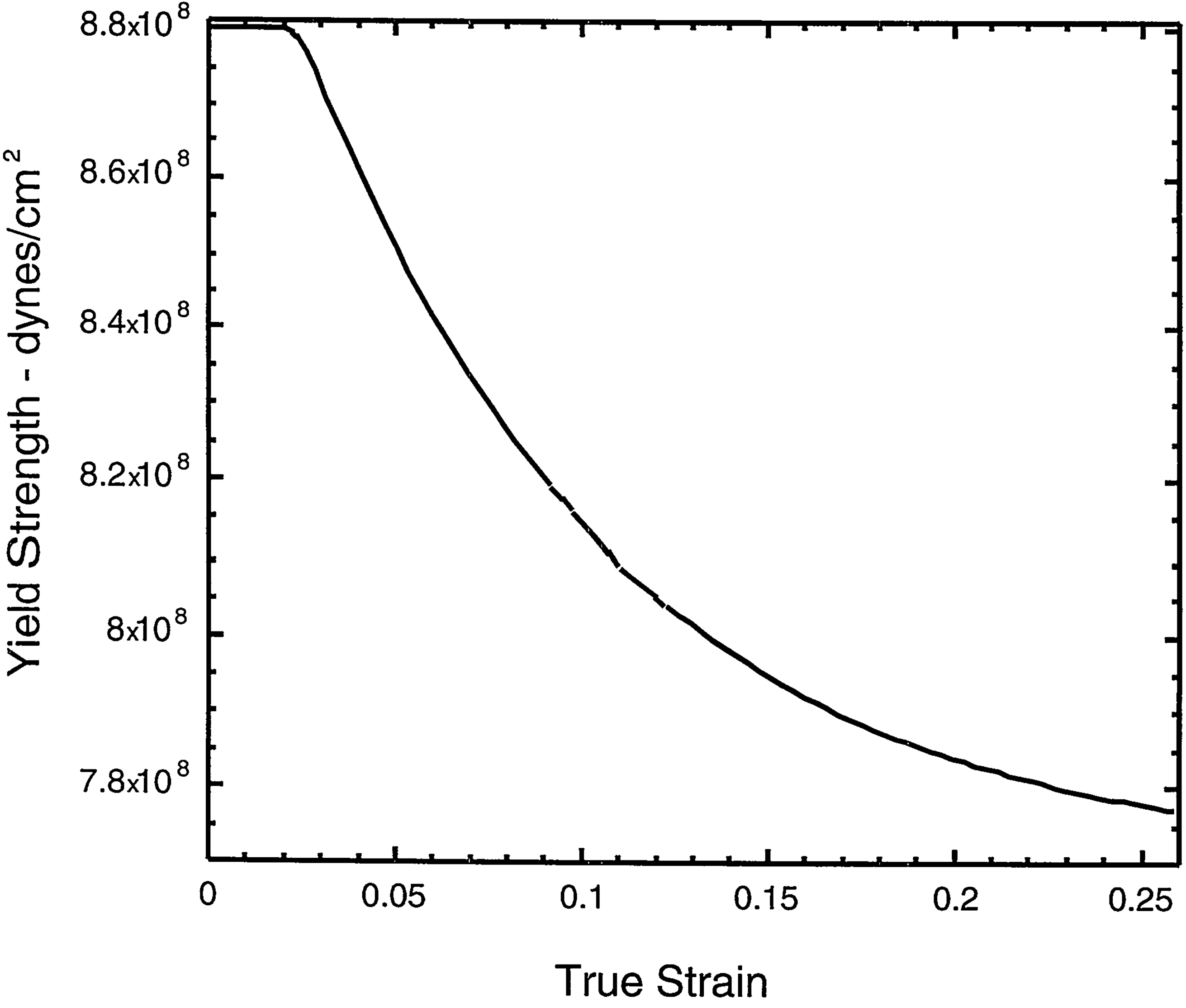

Figure 18: Strain softening response in free surface swelling.

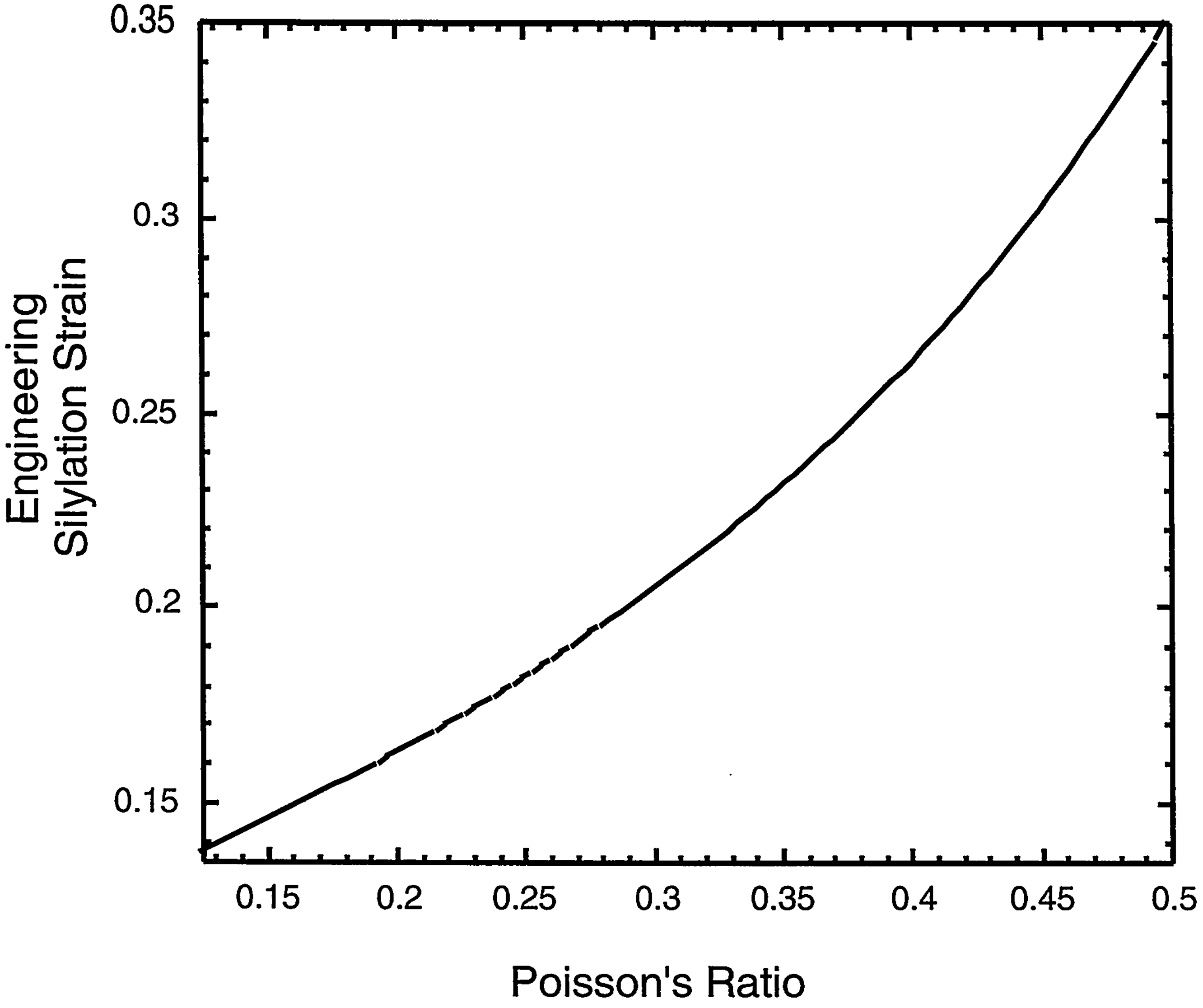

Figure 19: Free surface expansion for idealized elastic response.

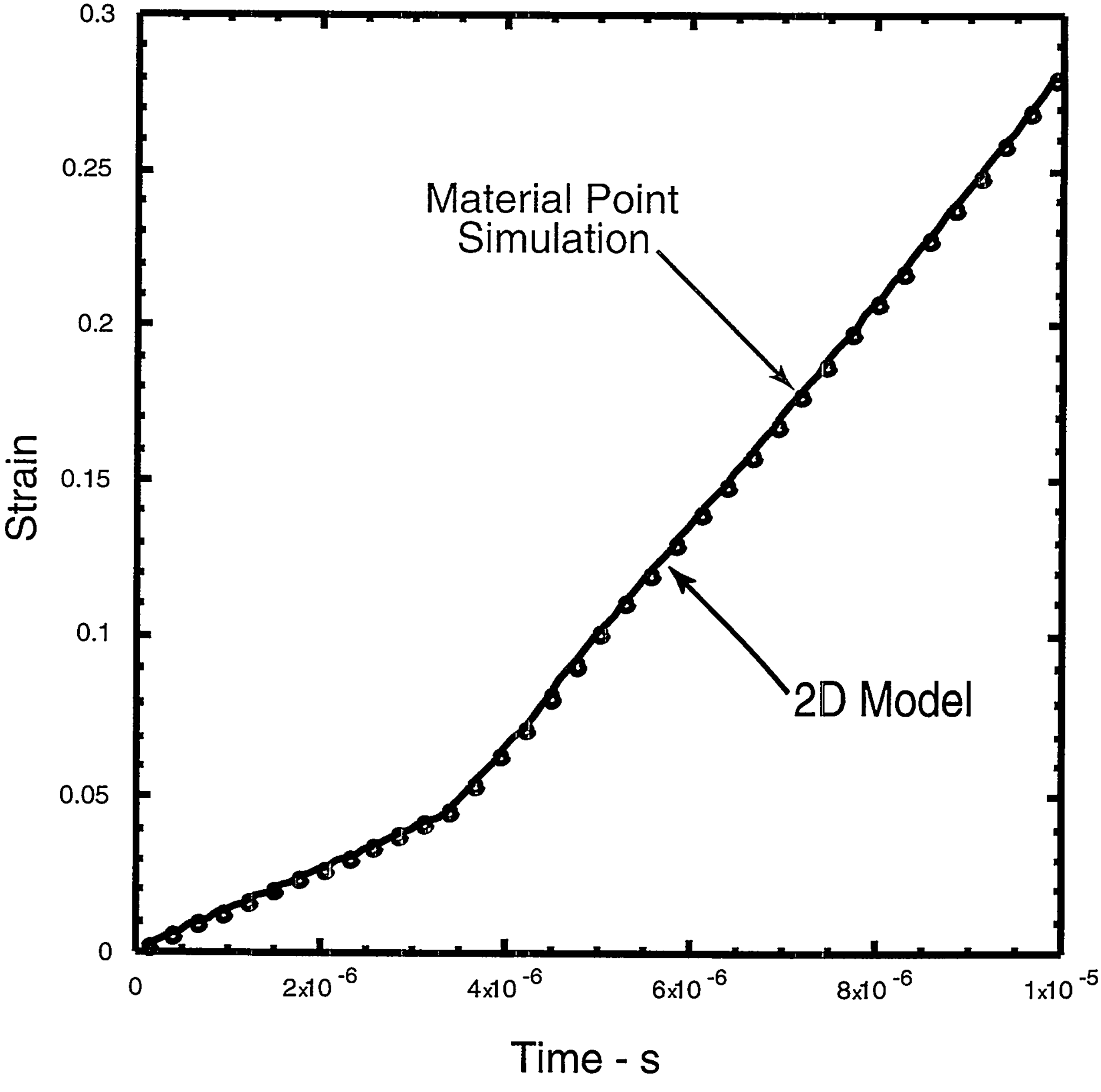

Figure 20: Large strain swelling simulation: Comparison of material point simulation and 2D model.

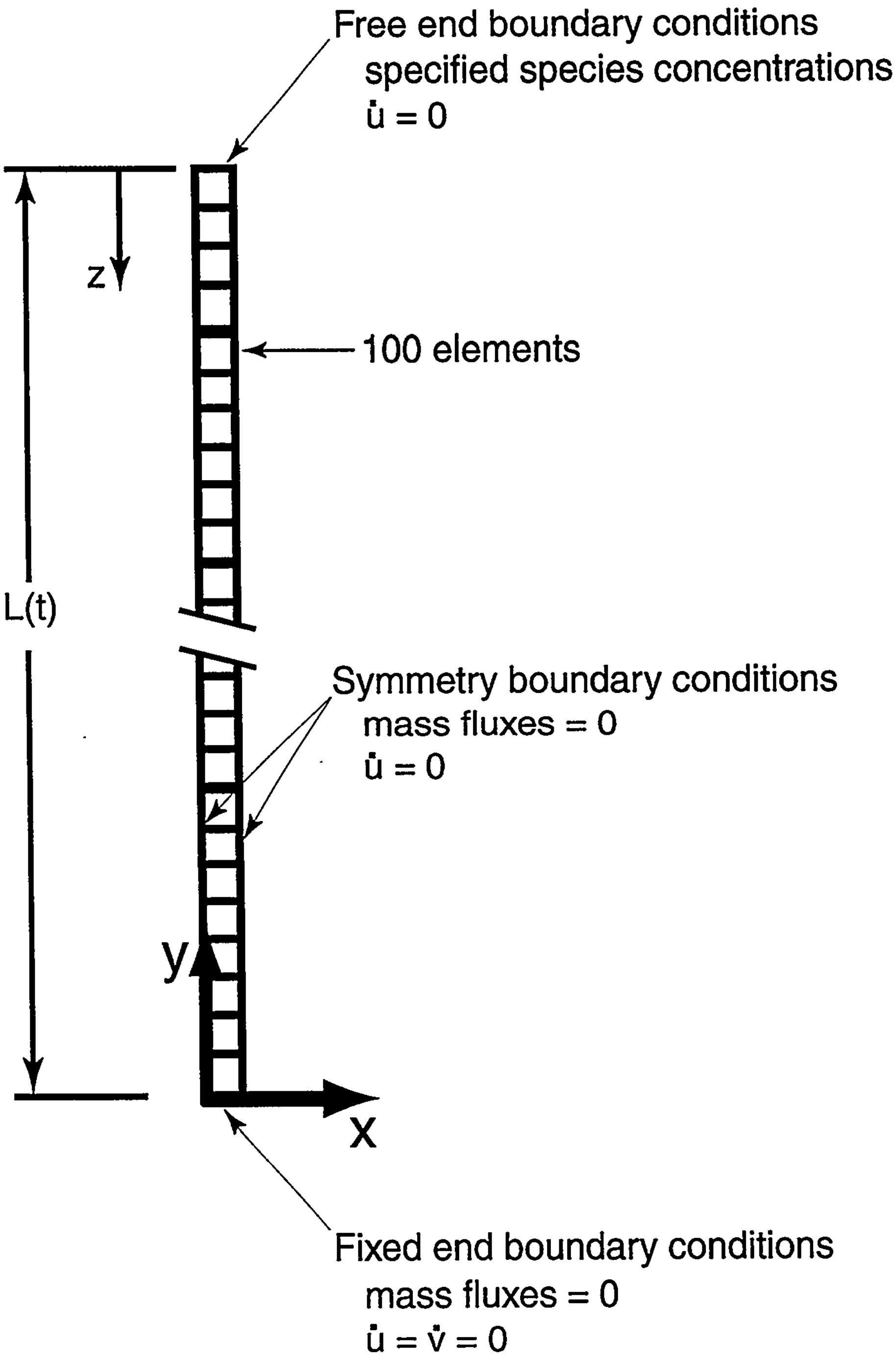

Figure 21: Geometry for 1-D solution comparisons.

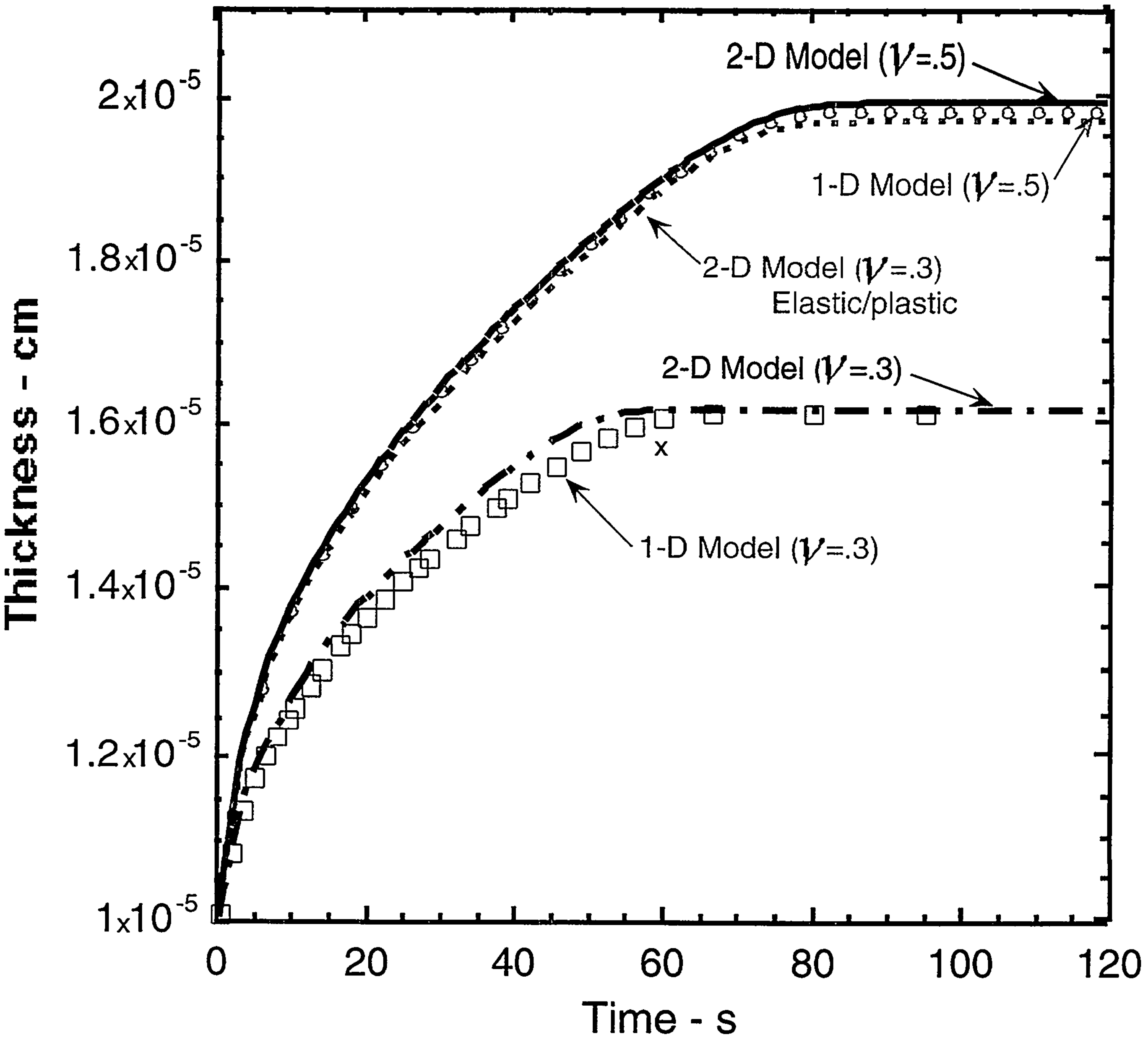

Figure 22: 1-D and 2-D model predictions for layer thickness as a function of time.

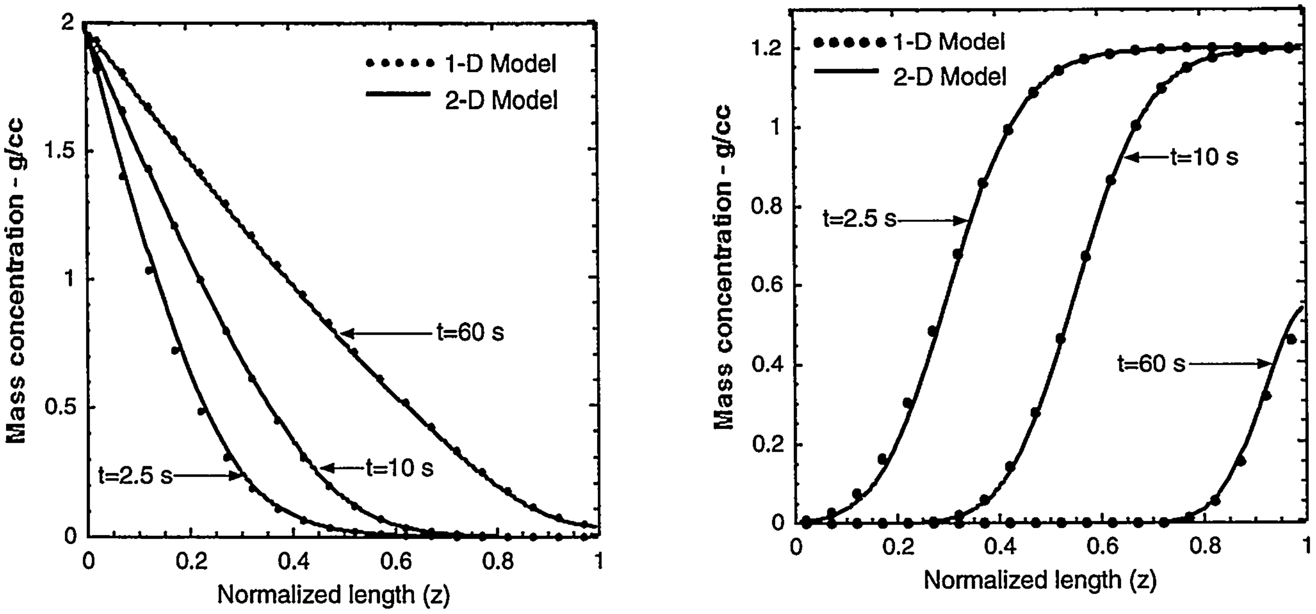

(a) Distribution of silylating agent

(b) Distribution of unsilylated resist

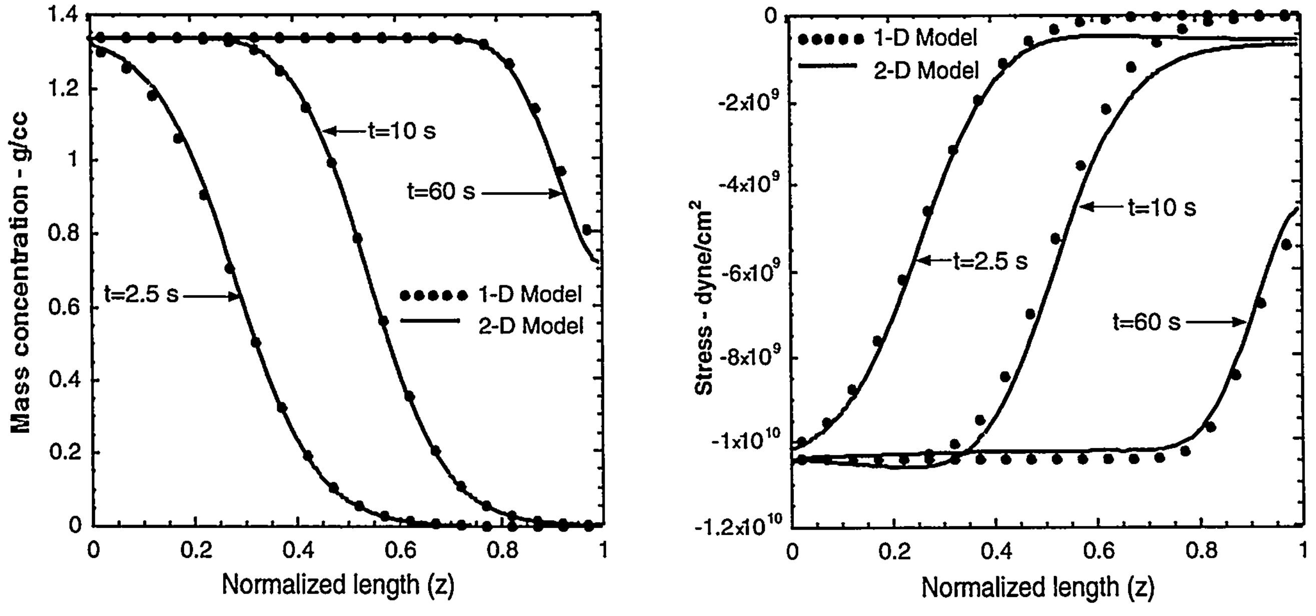

(c) Distribution of silylated resist

(d) Lateral stress distribution

Figure 23: Distributions of species concentrations and stress at three different times for $\nu = 0.5$.

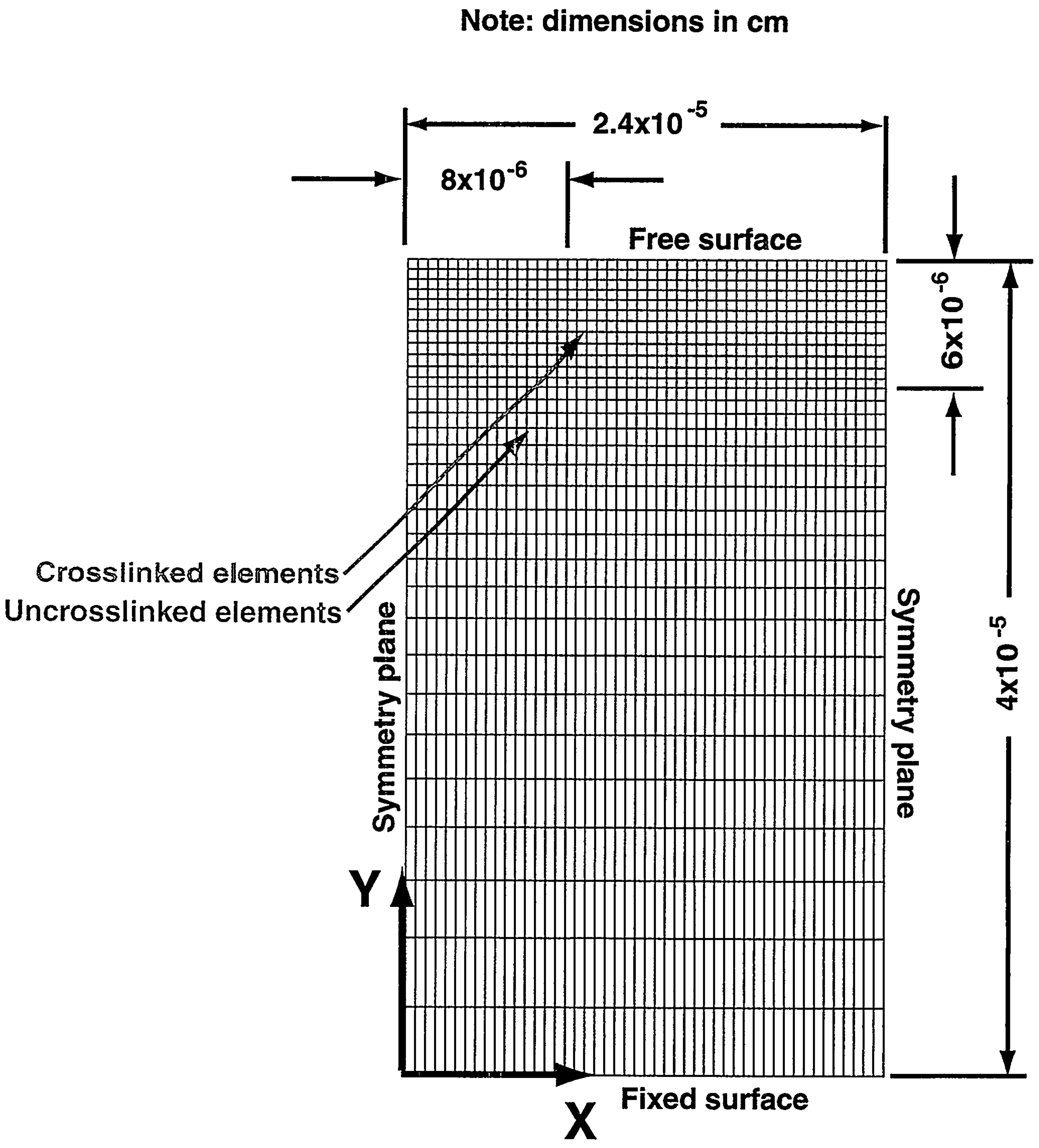

Figure 24: Computational mesh for the nominal 2D silylation simulation.

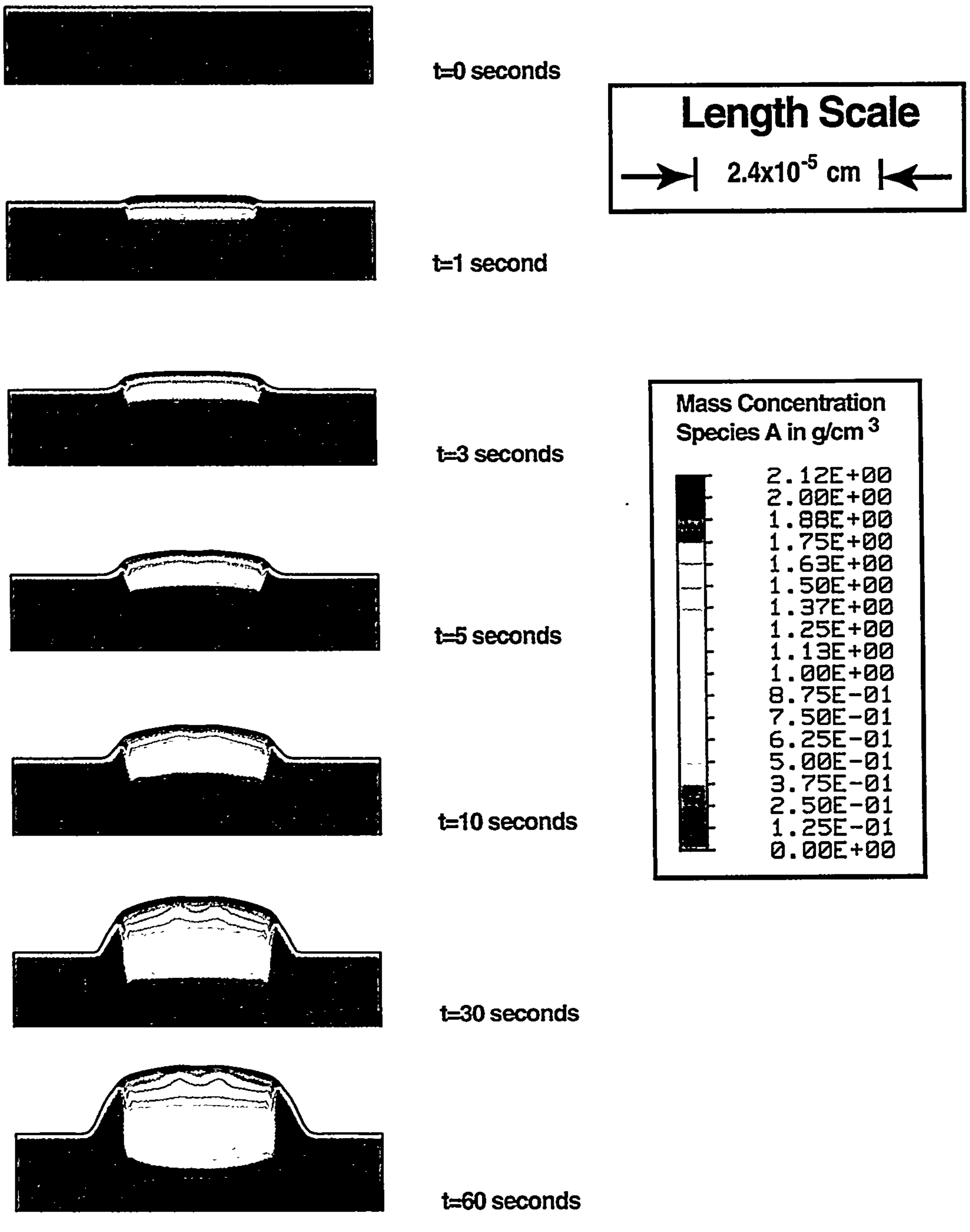

Figure 25: 2D material swelling with superimposed concentration profiles of the silylation agent (species A) as a function of time.

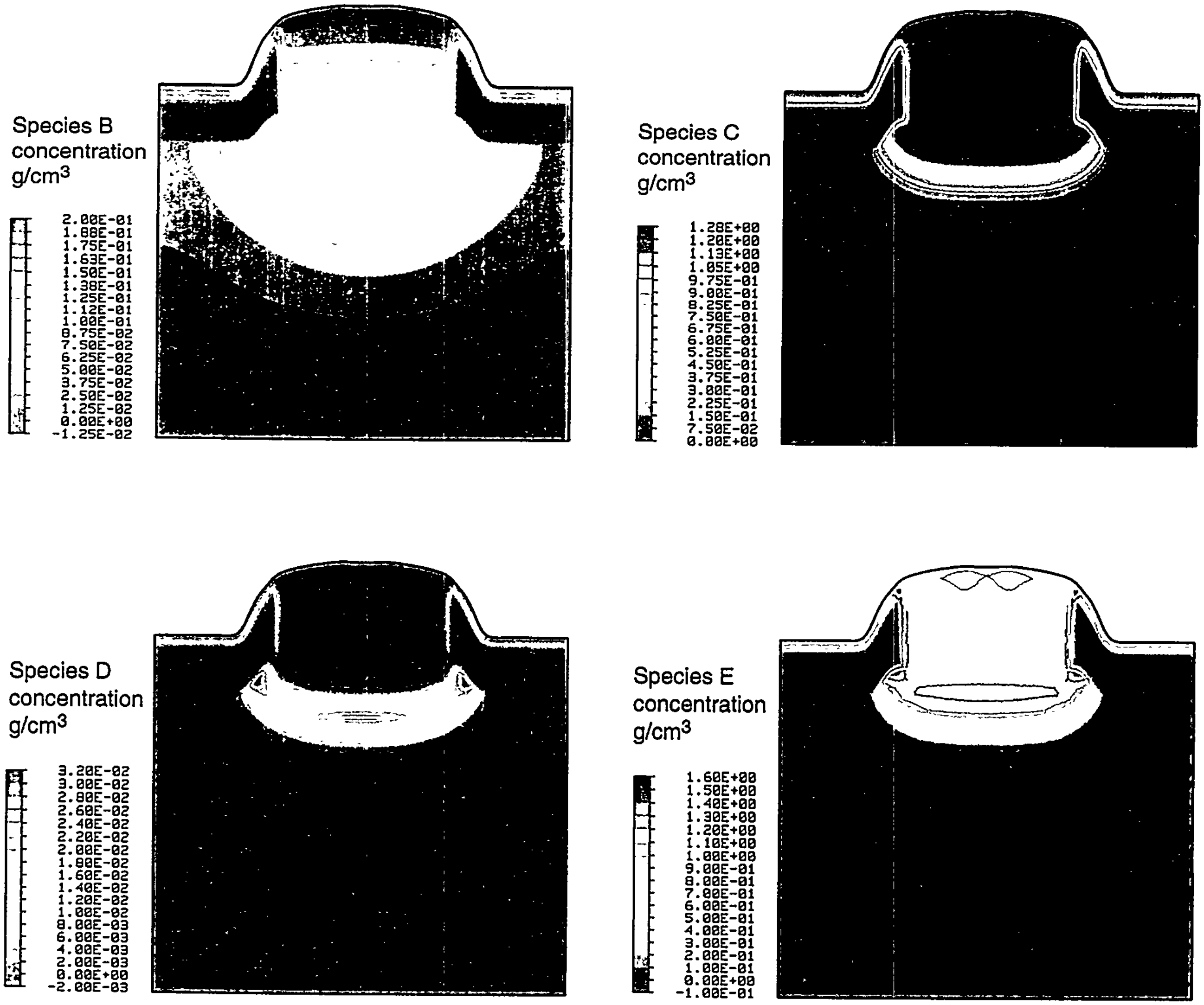

Figure 26: 2D concentration profiles for species B, C, D, and E at 60 seconds.

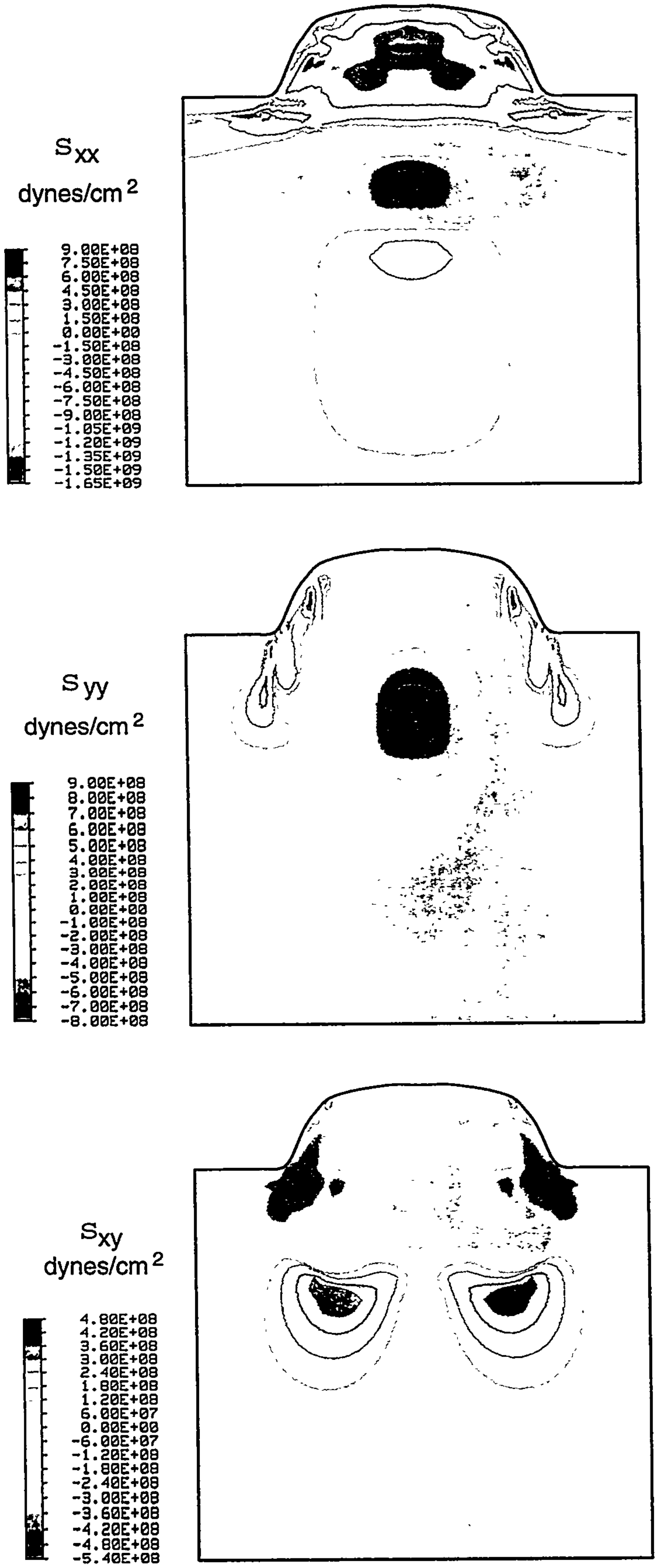

Figure 27: 2D stress distributions at 60 seconds.

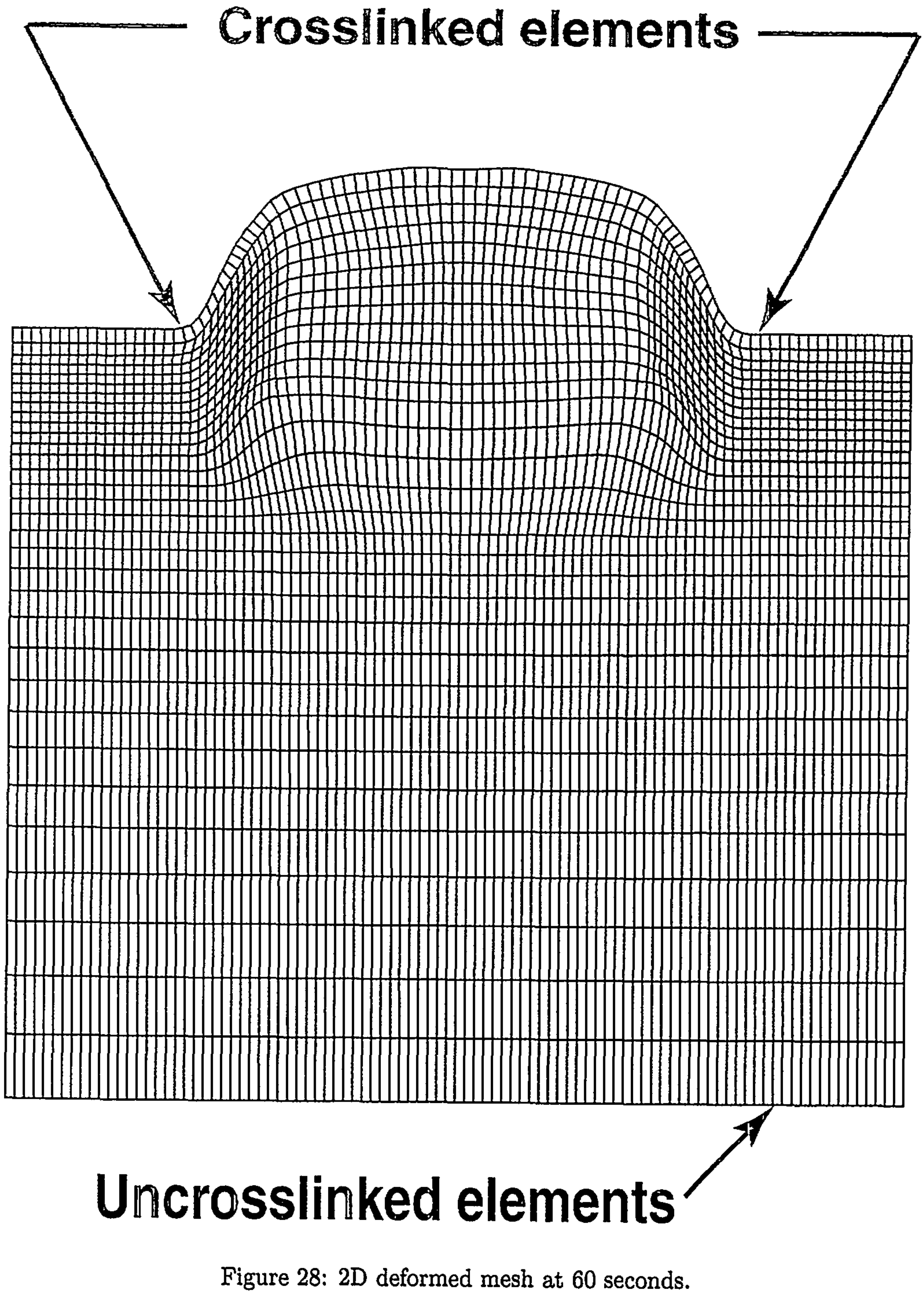

Figure 28: 2D deformed mesh at 60 seconds.

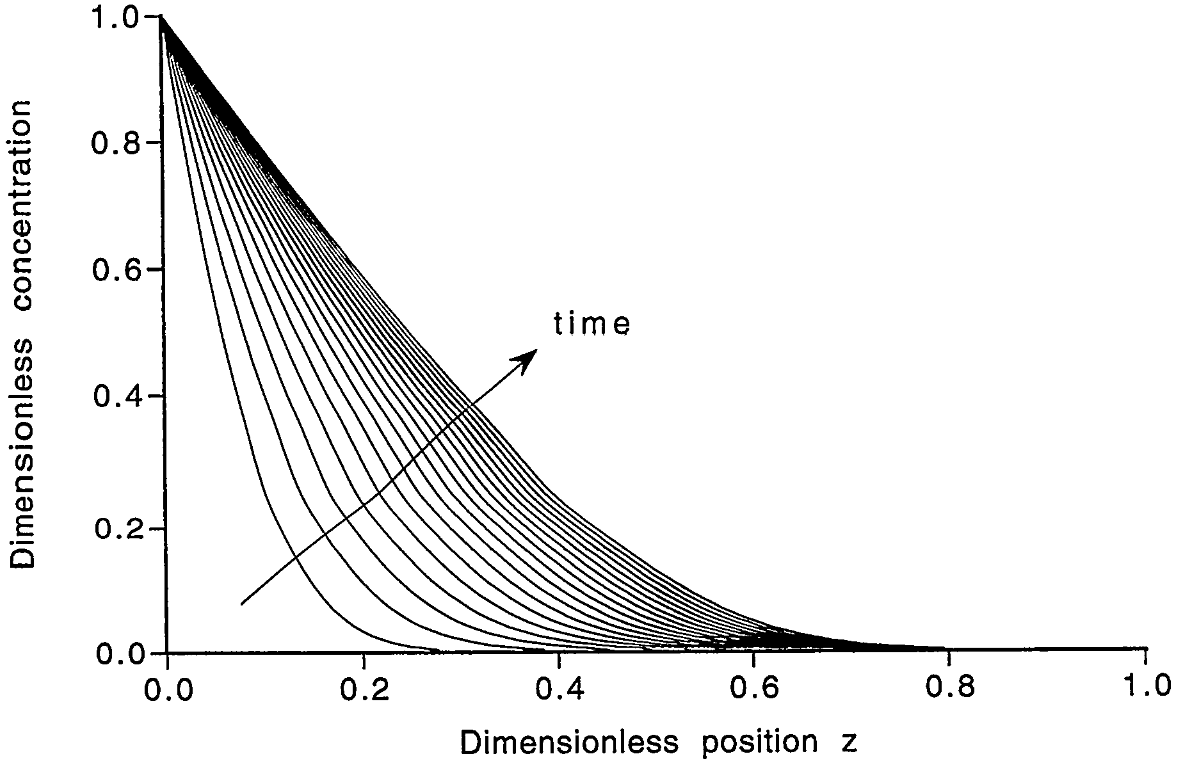

Figure 29: Concentration profiles for silylating agent P in one-dimensional model for $\theta = 0.01$, $\beta = 1$, $\tau_r = 1$, $\alpha = 2$, $\gamma = 1$, $\nu = 0.5$, and $\lambda = 1$.

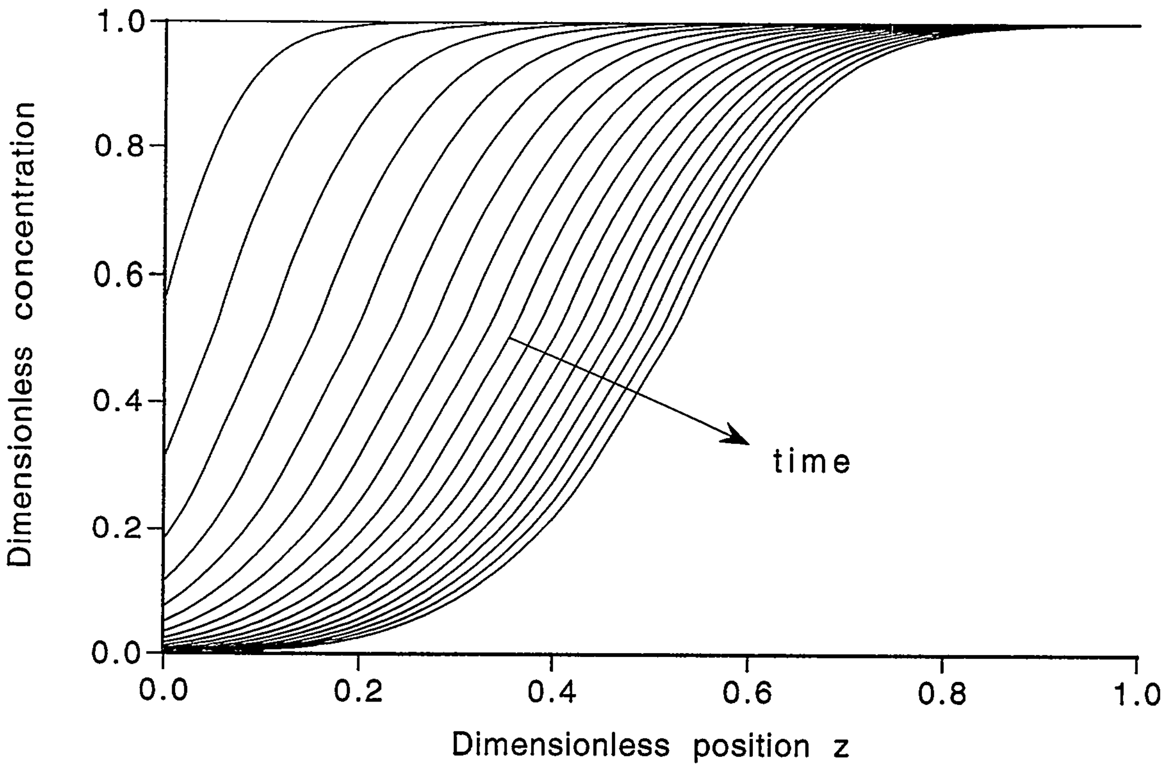

Figure 30: Concentration profiles for unreacted solid Q in one-dimensional model for $\theta = 0.01$, $\beta = 1$, $\tau_r = 1$, $\alpha = 2$, $\gamma = 1$, $\nu = 0.5$, and $\lambda = 1$.

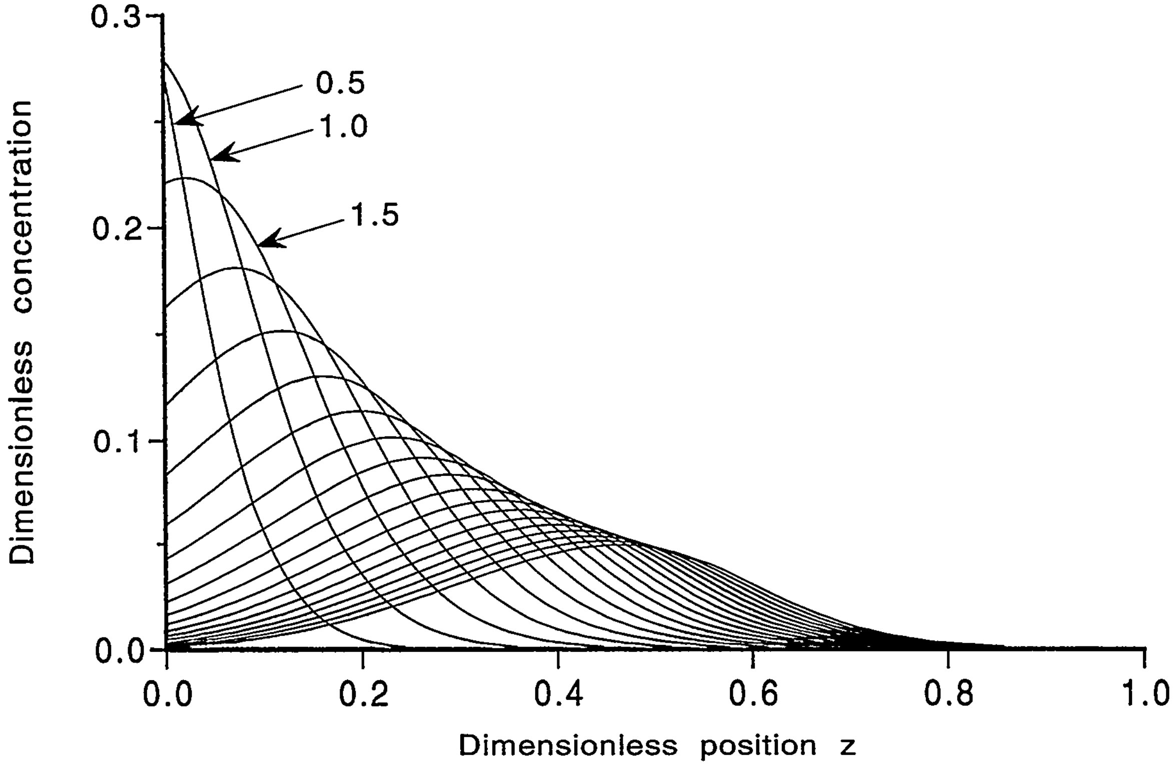

Figure 31: Concentration profiles for reacted but unexpanded solid U in one-dimensional model for $\theta = 0.01$, $\beta = 1$, $\tau_r = 1$, $\alpha = 2$, $\gamma = 1$, $\nu = 0.5$, and $\lambda = 1$.

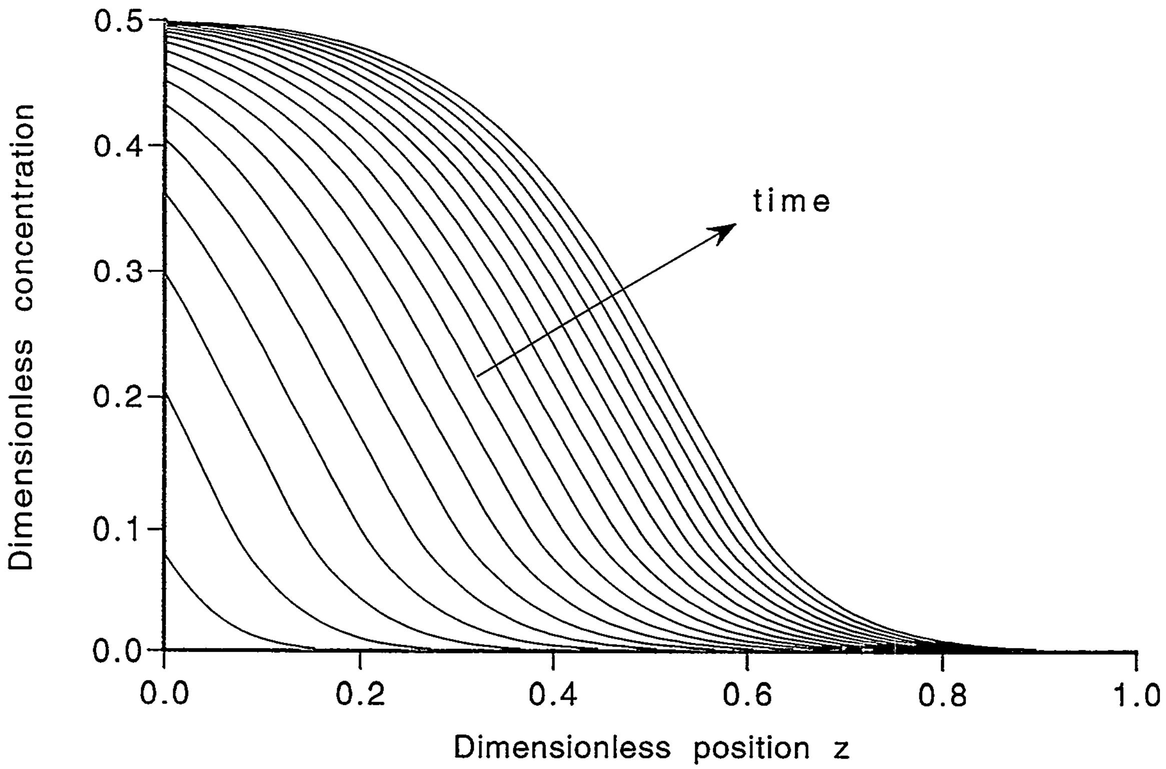

Figure 32: Concentration profiles for reacted and expanded solid E in one-dimensional model for $\theta = 0.01$, $\beta = 1$, $\tau_r = 1$, $\alpha = 2$, $\gamma = 1$, $\nu = 0.5$, and $\lambda = 1$.

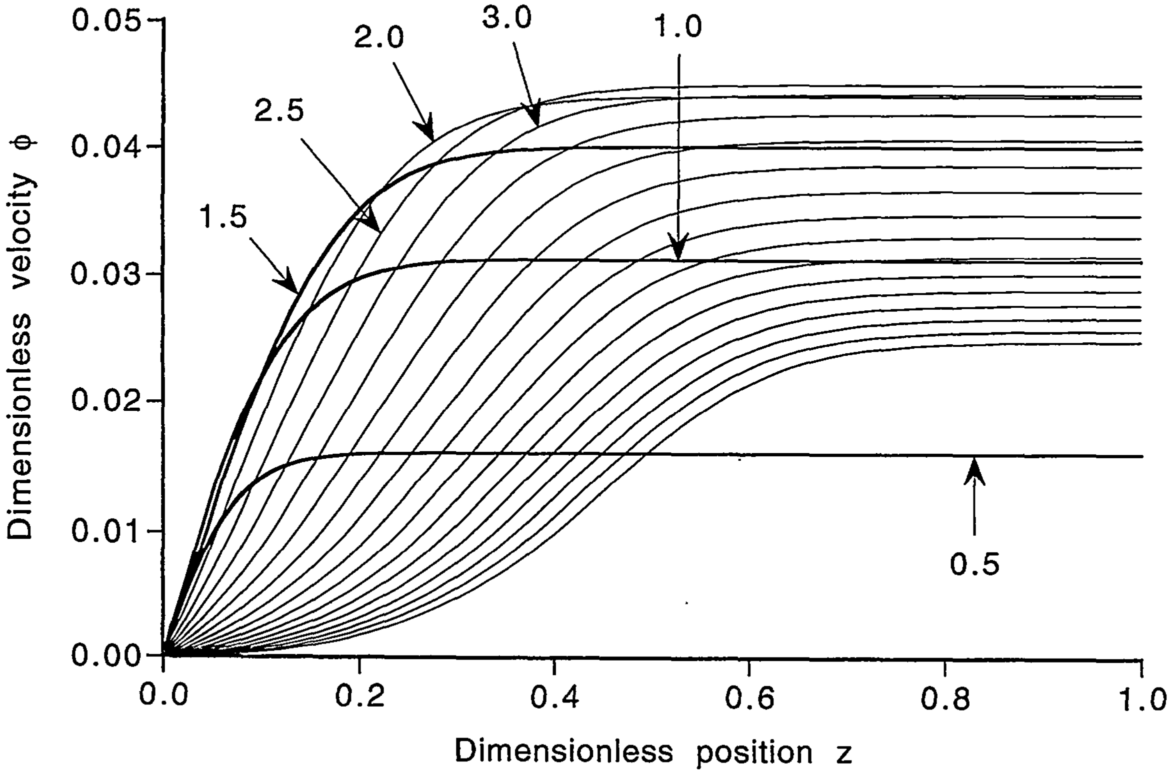

Figure 33: Velocity profiles in one-dimensional model for $\theta = 0.01$, $\beta = 1$, $\tau_r = 1$, $\alpha = 2$, $\gamma = 1$, $\nu = 0.5$, and $\lambda = 1$.

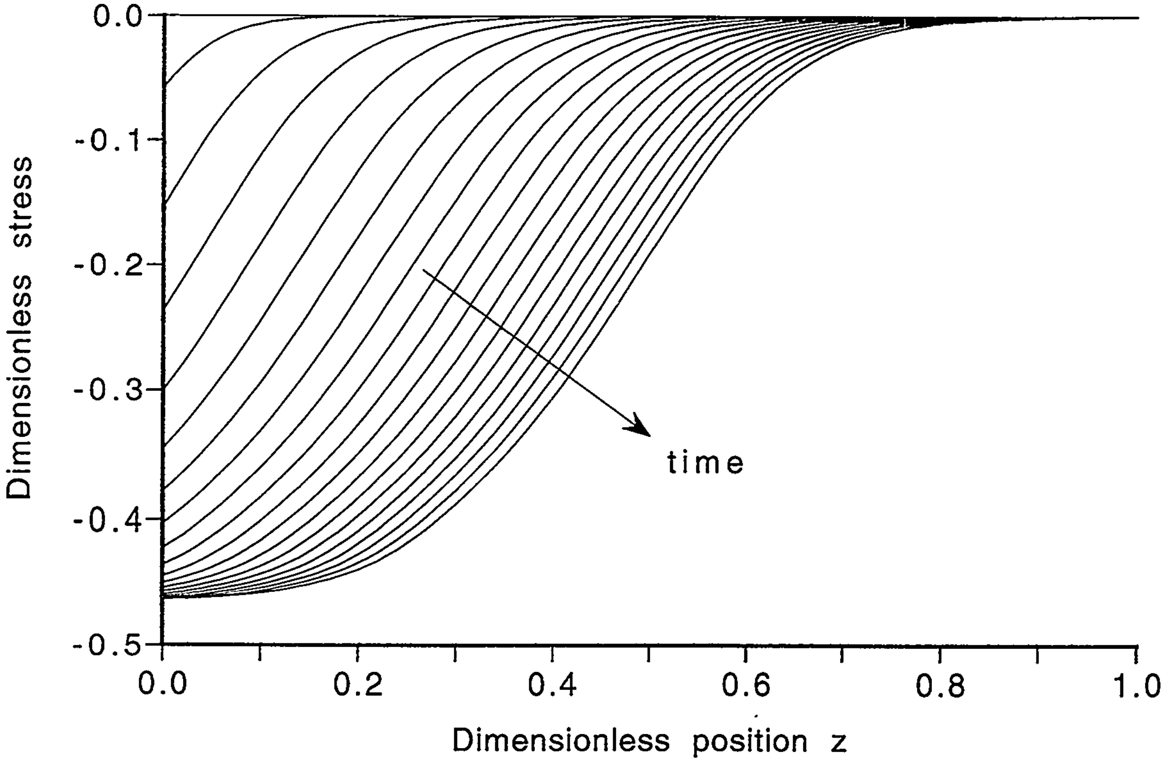

Figure 34: Stress profiles in one-dimensional model for $\theta = 0.01$, $\beta = 1$, $\tau_r = 1$, $\alpha = 2$, $\gamma = 1$, $\nu = 0.5$, and $\lambda = 1$.

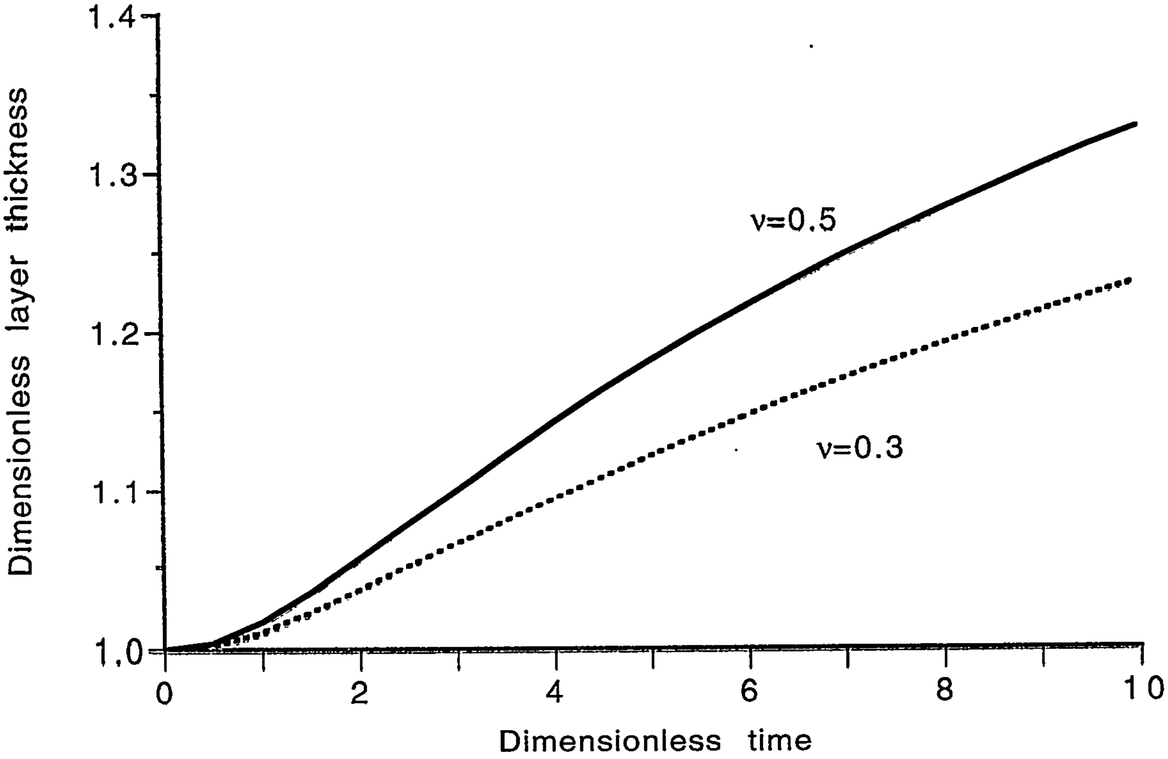

Figure 35: Progress of swelling in one-dimensional model for $\theta = 0.01$, $\beta = 1$, $\tau_r = 1$, $\alpha = 2$, $\gamma = 1$, and $\lambda = 1$.

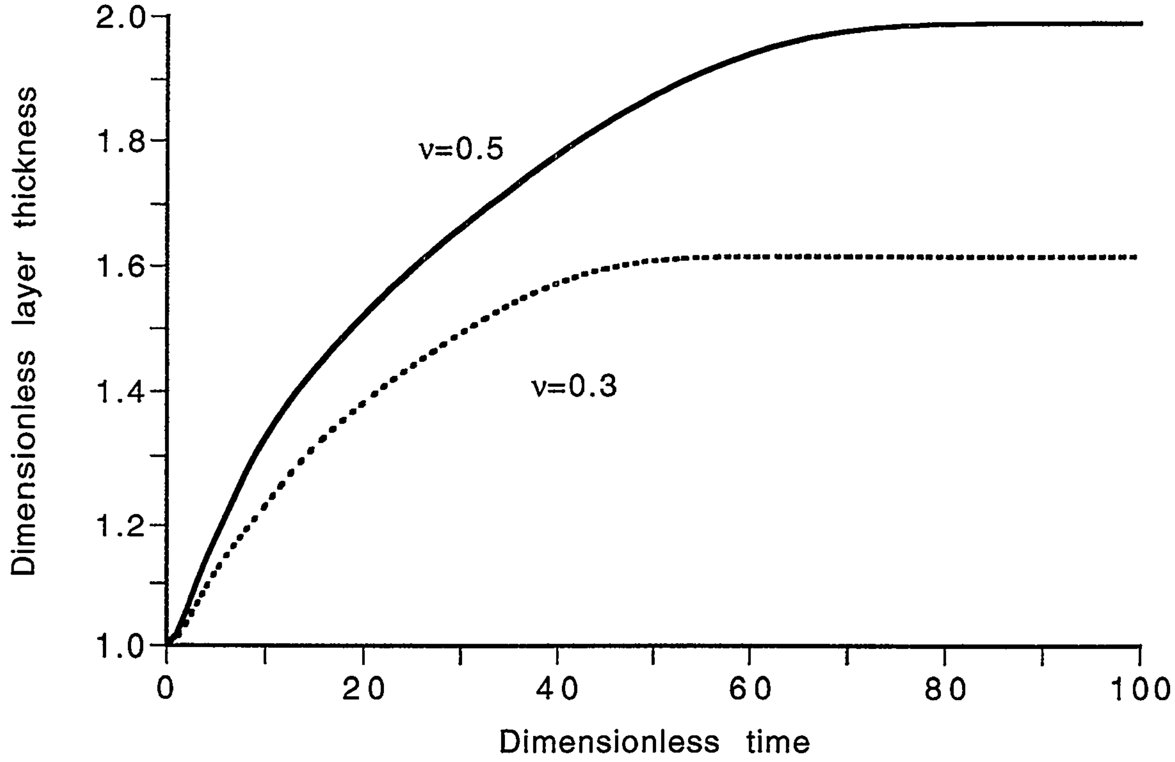

Figure 36: Overall progress of swelling in one-dimensional model for $\theta = 0.01$, $\beta = 1$, $\tau_r = 1$, $\alpha = 2$, $\gamma = 1$, and $\lambda = 1$.

References

[1] C. Henderson, D. Wheeler, T. Pollagi, G. Cardinale, D. O'Connell, A. Fisher, and J. Goldsmith. "Top Surface Imaging for Extreme Ultraviolet Lithography",. Y. Vladimirski, editor, *Emerging Lithographic Technologies II.* Proc. SPIE 3331, 1998.

[2] W.S. Han, J.H. Lee, H.Y. Kang, C.G. Park, Y.B. Koh, and M.Y. Lee. "Optimization of Deep UV Positive Tone Top Surface Imaging Process",. *Microelectronic Engineering*, **23**:255–258, 1994.

[3] D.C. La Tulipe, A.T.S. Pomerene, J.P. Simons, and D.E. Seeger. "Positive Mode Silylation Process Characterization",. *Microelectronic Engineering*, **17**:265–268, 1991.

[4] M.W. Horn, B.E. Maxwell, R.B. Goodman, R.R. Kunz, and L.M. Eriksen. "Plasma-deposited Silylation Resist for 193 nm Lithography",. *J. Vac. Sci. Technol. B*, **14**(6):4207–4211, 1996.

[5] T. Itani, H. Yoshino, S. Hashimoto, M. Yamana, N. Samoto, and K. Kasama. "A Study of Acid Diffusion in Chemically Amplified Deep Ultraviolet Resist",. *J. Vac. Sci. Technol. B*, 14(6):4226–4228, 1996.

[6] N. Glezos, G.P. Patsis, I. Raptis, and P. Argitis. "Application of a Reaction-Diffusion Model for Negative Chemically Amplified Resists to Determine Electron-Beam Proximity Correction Parameters",. *J. Vac. Sci. Technol. B*, **14**(6):4252–4256, 1996.

[7] C.S. Whelan, D.M. Tanenbaum, D.C. La Tulipe, M. Isaacson, and H.G. Craighead. "Low Energy Electron Beam Top Surface Image Processing Using Chemically Amplified AXT Resist",. *J. Vac. Sci. Technol. B*, **15**(6):2555–2560, 1997.

[8] M.A. Zuniga and A. R. Neureuther. "Diagnostics of Patterning Mechanisms in Chemically Amplified Resists from Bake Dependencies of Images",. *J. Vac. Sci. Technol. B*, **14**(6):4221–4225, 1996.

[9] L.E. Ocola and F. Cerrina. "Latent Image Characterization of Postexposure Bake Process in Chemically Amplified Resists",. *J. Vac. Sci. Technol. B*, **15**(6):2545–2549, 1997.

[10] M. Weiss and M. Goethals. "A Novel Approach to Simulation of the Silylation Bake in the DESIRE Process",. *Microelectronic Engineering*, **30**:313–316, 1996.

[11] B.E. Deal and A.S. Grove. "General Relationship for the Thermal Oxidation of Silicon",. *J. Appl. Phys.*, **36**(12):3770, 1965.

[12] L. Bauch, U. Jagdhold, J. Bauer, B. Dietrich, and W. Hoppner. "Positive Mode Silylation Process Characterization",. *Microelectronic Engineering*, **17**:265–268, 1991.

[13] M.A. Hartney, M. Rothschild, R.R. Kunz, D.J. Ehrlich, and D.C. Shaver. "Positive-Tone Silylation Processes at 193 nm",. *Microelectronic Engineering*, **13**:51–56, 1991.

[14] P.J. Paniez, O.P. Joubert, J.C. Oberlin M.J. Pons, T.G. Vachette, A.P. Weill, J.H. Pelletier, and C. Fiori. "The Role of Self Diffusion in the Dry Development and Plasma Durability of Polymers". *Microelectronic Engineering*, **13**:57–60, 1991.

[15] C. Pierrat. "New Model of Polymer Silylation: Application to Lithography",. *J. Vac. Sci. Technol. B*, **10**(6):2581–2588, 1992.

[16] W.S. Winters and W.E. Mason. "The Computer Code PASTA and Its Application to Coupled Thermal-

Mechanical Problems",. S.N. Atluri and G. Yagawa, editors, *The Proceedings of the International Conference on Computational Engineering Science*, pp. 59.vii.2–59.vii.4, Springer-Verlag, New York, NY. 1988.

[17] W.S. Winters and W.E. Mason. "PASTA2D-Applications",. Technical Report SAND89-8217, Sandia National Laboratories, Livermore, CA, 1989.

[18] Y.I. Dimitrienko. "Effect of Finite Deformations on Internal Heat-Mass Transfer in Elastomer Ablating Materials",. *Int. J. Heat Mass Transfer*, **40**(3):699–709, 1997.

[19] M.A. Zuniga and A. R. Neureuther. "Stress Dependent Silylation Model and Two-Dimensional Profile Simulation",. *J. Vac. Sci. Technol. B*, **15**(6):2565–2569, 1997.

[20] D. Wheeler, E. Scharrer, G. Kubiak, R. Hutton, S. Stein, R. Cirelli, F. Baiocchi, M. Cheng, C. Boyce, and G. Taylor. "Silylating Reagents with High Silicon Contents for Dry-Developed Positive-Tone Resists for Extreme-UV (13.5 nm) and Deep-UV (248 nm) Microlithography",. R. L. Clough and W. Shalaby, editors, *Irradiation of Polymers: Fundamentals and Technological Applications; ACS Symposium Series No. 620*, pp. 399–415. The American Chemical Society, 1996.

[21] A. Wong. PhD. Thesis. The University of California, Berkeley, CA, 1994.

[22] S. Whitaker. *Fundamental Principles of Heat Transfer*. R. E. Krieger Publishing Co., MaLabor, Florida, 1983.

[23] M. A. Hartney. "Modeling of Positive-tone Silylation Processes for 193-nm Lithography",. *J. Vac. Sci. Technol. B*, 11(3):681–687, 1993.

[24] N. L. Thomas and A. H. Windle. "A Theory of Case II Diffusion",. *Polymer*, **23**:529–542, April 1982.

[25] J. Crank and G. S. Park. *Diffusion in Polymers*. Academic Press, New York, 1968.

[26] C. Gostoli and G. C. Sarti. "Diffusion and Localized Swelling Resistances in Glassy Polymers",. *Polymer Engineering and Science*, **22**(16):529–542, 1982.

[27] J. Crank. *The Mathematics of Diffusion, 2nd Edition*. Clarendon Press, Oxford, 1975.

[28] S. Middleman. *Introduction to Mass and Heat Transfer*. Wiley, New York, 1998.

[29] R.N. Haward and G. Thackray. "The Use of a Mathematical Model to Describe Isothermal Stress-Strain Curves in Glassy Polymers",. *Proc. Roy. Soc. A.*, **302**:453–472, 1968.

[30] M.C. Boyce, D.M. Parks, and A.S. Argon. "Large Inelastic Deformation of Glassy polymers. Part I: Rate Dependent Constitutive Model",. *Mechanics of Materials*, **7**:15–33, 1988.

[31] A. Hoger. "The Material Time Derivative of Logarithmic Strain",. *Int. J. Solids Structures*, **22**(9):1019–1032, 1986.

[32] D.J. Bammann and G.C. Johnson. "On the Kinematics of Finite Deformation Plasticity",. *Acta Mechanica*, **70**:1–13, 1987.

[33] D.J. Bammann and E.C. Aifantis. "A Model for Finite Deformation Plasticity",. *Acta Mechanica*, **69**:91–117, 1987.

[34] K.H. Huebner and E.A. Thornton. *The Finite Element Method for Engineers*. John Wiley, New York,

1982.

[35] P. N. Brown, G. D. Byrne, and A. C. Hindmarsh. "VODE: A Variable Coefficient ODE Solver",. *SIAM J. Sci. Stat. Comput.*, **10**:1038–1051, 1989;. also Lawrence Livermore National Laboratory (LLNL) Report UCRL-98412, June 1988.

[36] G. E. Schneider and M. J. Raw. "Control Volume Finite-Element Method for Heat Transfer and Fluid Flow using Colocated Variables - 1. Computational Procedure",. *Numerical Heat Transfer*, **11**:363–390, 1987.

[37] B. F. Blackwell and R. E. Hogan. "Numerical Solution of Axisymmetric Heat Conduction Problems using Finite Control Volume Technique",. *Journal of Thermophysics and Heat Transfer*, **7**(3):462–471, 1993.

[38] R. E. Hogan, B. F. Blackwell, and R. J. Cochran. "Application of Moving Grid Control Volume Finite Element Method to Ablation Problems". *Journal of Thermophysics and Heat Transfer*, **10**(2):312–319, 1996.

[39] J.O. Hallquist. "User's Manual for DYNA2D - An Explicit Two-Dimensional Hydrodynamic Finite Element Code with Interactive Rezoning",. Technical Report UCID-18756, Lawrence Livermore National Laboratory, Livermore, CA, 1980.

[40] L.M. Taylor and D. Flanagan. "PRONTO2D, A Two-Dimensional Transient Solid Dynamics Program",. Technical Report SAND86-0594, Sandia National Laboratories, Albuquerque, NM, 1987.

[41] J.O. Hallquist. "NIKE2D: An Implicit, Finite-Element Code for Analyzing the Static and Dynamic Response of Two-Dimensional Solids",. Technical Report UCRL-52678, Lawrence Livermore National Laboratory, Livermore, CA, 1979.

[42] G. Maenchen and S. Sack. "The TENSOR Code",. *Methods in Comp. Physics*, **3**:181–210, 1964.

[43] D.P. Flanagan and T. Belytschko. "A Uniform Strain Hexahedron and Quadrilateral with Orthogonal Hourclass Control",. *Int. Journal for Numerical Methods in Engineering*, **17**:679–706, 1981.

[44] T. Belytschko and J.S. Ong. "Hourglass Control in Linear and Nonlinear Problems",. *Computer Methods in Applied Mechanics and Engineering*, **43**:251–276, 1984.

[45] K.J. Perano and V.N. Kaliakin. "INTERP- A Fortran Callable Free Format Data Interpretation Subroutine System",. Technical Report SAND87–8244, Sandia National Laboratories, Livermore, CA, 1989.

[46] K.J. Perano. "COMPRO - A Subroutine System for Syntactical Analysis",. Technical Report SAND89-8441, Sandia National Laboratories, Livermore, CA, 1989.

[47] P.E. Nielan, K.J. Perano, and W.E. Mason. "ANTIPASTO: An Interactive Mesh Generator and Preprocessor for Two-Dimensional Analysis Programs",. Technical Report SAND90–8203, Sandia National Laboratories, Livermore, CA, 1990.

[48] R.B. Bird, W.E. Stewart, and E.N. Lightfoot. *Transport Phenomena.* Wiley, New York, 1960.

[49] L.D. Landau and E.M. Lifshitz. *Theory of Elasticity.* Pergamon Press, Oxford, 1970.

[50] J.R. Welty, C.E. Wicks, and R.E. Wilson. *Fundamentals of Momentum, Heat and Mass Transfer.* Wiley, New York, 1969.

[51] L.R. Petzold. "A Description of DASSL: A Differential-Algebraic System Solver",. Technical Report SAND82–8637, Sandia National Laboratories, Livermore, CA, 1982.

Distribution

EXTERNAL DISTRIBUTION:

Prof. D. S. Dandy
Colorado State University
Dept. Agriculture and Chem Eng.
Fort Collins, CO 80523

Prof. M. C. Boyce
Massachusetts Institute of Technology
Dept. of Mechanical Engineering
Cambridge, MA 02139

L. Chuzhoy
Caterpillar Inc.
Technical Center, Bldg. E
Division 854
P.O. Box 1875
Peoria, IL 61656-1875

J. Cobb
EUVLLC/Motorola Assignee
Sandia National Laboratories
P.O. Box 969
MS 9911
Livermore, CA 94551-0969

E. Croffie
211-19 Cory Hall #1772
EECS Dept.
University of California
Berkeley, CA 94720

Prof. H. A. Dwyer
Dept of Aero. and Mech. Eng.
University of California
Davis, CA 95616

Prof. R.W. Dutton
CIS Extension, Room 333
Integrated Circuits Laboratory
Stanford University
Stanford, CA 94305-4075

G. Feit
SEMATECH
2706 Montopolis Drive
Austin, TX 78741-6299

Prof. D. L. Flamm
Dept. EECS
187M Cory Hall
University of California
Berkeley,CA 94596.

Prof. R. Greif
Dept. of Mech. Eng.
University of California
Berkeley, CA 94720

Prof. R. J. Kee
Engineering Division
Colorado School of Mines
Golden, CO 80401-1887

Ellen Meeks (RD)
Reaction Design
6500 Dublin Blvd., Suite 214
Dublin, CA 94568

Prof. A. R. Neureuther
Dept. EECS
University of California
Berkeley, CA 94720

Uzo Okoroanyanwu
AMD
One AMD Place
P.O. Box 3453
MS 78
Sunnyvale, CA 94088-3453

Prof. W. G. Oldham
Dept. EECS
University of California
Berkeley, CA 94720

Dr. S. C. Palmateer
Room MEL 204B
244 Wood St.
Lexington, MA 02173

Veena Rao
Intel
SCI-03
3065 Bowers Ave.
Santa Clara, CA 95052

G. Taylor
Shipley
455 Forest St.
Marlborough, MA 01752

C. Grant Willson
Chemical Engineering
Campus Mail Code: C0400
University of Texas
Austin, TX 78712

Marco Zuniga
C/O
Prof. A. R. Neureuther
Dept. EECS
University of California
Berkeley, CA 94720

INTERNAL DISTRIBUTION:

MS 0601	1126	M. E. Coltrin
MS 0601	1126	J. Y. Tsao
MS 0603	1711	P. Esherick
MS 1405	1812	D. R. Wheeler
MS 9001	8000	T. O. Hunter
		Attn: J. B. Wright, 2200
		M. E. John, 8100
		R. C. Wayne, 8400
		L. A. Hiles, 8800
		D. R. Henson, 8900
MS 9214	8980	W. E. Mason
MS 9420	8200	A. L. West
		Attn: L. N. Tallerico, 8204
		A. J. West, 8240
		C. T. Oien, 8260
MS 9405	8230	J. M. Hruby
MS9405	8230	C. C. Henderson
MS 9409	8250	G. D. Kubiak
MS 9409	8250	G. F. Cardinale
MS 9409	8270	R. H. Stulen
MS 9409	8270	A. Ray-Chaudhuri
MS 9054	8300	W. J. Mclean
		Attn: L. A. Rahn,8351
		F. P. Tully,8353
		W. Bauer, 8358
		D. R. Hardesty, 8361
		R. W. Carling, 8362
		R. J. Gallagher, 8366
MS 9041	8345	J. S. Binkley
MS 9042	8345	G. H. Evans (10)
MS 9051	8345	J. F. Grcar
MS 9042	8345	S. Griffiths
MS 9042	8345	W. G. Houf
MS 9051	8345	R. S. Larson
MS 9051	8345	A. E. Lutz
MS 9042	8345	C. D. Moen
MS 9042	8345	R. H. Nilson
MS 9402	8345	D. Rader
MS 9051	8345	F. M. Rupley
MS 9042	8345	P. A. Spence

MS 9051	8345	A. Ting
MS 9042	8345	W. S. Winters (10)
MS 9052	8361	M. Allendorf
MS 9405	8700	M. T. Dyer
		Attn: M. I. Baskes, 8712
		J. C. F. Wang, 8713
		G. J. Thomas, 8715
		K. L. Wilson,8716
		S. M. Foiles,8717
		W. A. Kawahara,8746
MS 9402	8701	C. M. Hartwig
MS 9042	8742	E. Chen
MS 9405	8743	P. E. Nielan
		Attn: D. J. Bammann,8743
		M. Horstemeyer, 8743
		M. L. Chiesa, 8743
		J. J. Dike, 8743
		A. R. Ortega, 8743
MS 9405	8743	L. A. Bertram
MS 9405	8743	J. F. Lathrop
MS 9405	8743	V. C. Prantil (10)
MS 9011	8980	K. Perano
MS 0841	9100	P. L. Hommert
		Attn: A. Ratzel, 9112
		R. Griffith, 9114
		W. Rutledge, 9115
		C. Peterson, 9116
		T. Baca, 9119
MS 0826	9111	W. L. Hermina
MS 0826	9111	D. K. Gartling
MS 0826	9111	R. Shunk
MS 0826	9113	S. Kempka
MS 0443	9117	H. S. Morgan
		Attn: J. B. Aidun, 9117
		S. W. Attaway,9117
		S. N. Burchett,9117
		A. F. Fossum,9117
MS 0443	9117	M. L. Blanford
MS 0443	9117	S. W. Key
MS 0443	9117	M. K. Neilsen
MS 0443	9117	V. L. Porter
MS 0443	9117	G. W. Wellman

3	MS 9018	Central Technical Files, 8940-2
1	MS 0899	Technical Library, 4916
1	MS 9021	Technical Communications Department, 8815/ Technical Library, MS 0899, 4916
1	MS 9021	Technical Communications Department, 8815 For DOE/OSTI
1	MS 1380	Technology Transfer, 4212